

NUCLEAR MAGNETIC RESONANCE OF ^{14}N IN SINGLE CRYSTAL GLYCINE
AND OF ^{15}N IN LIQUID AND SOLID N_2

By

LYLE MILTON ISHOL

A DISSERTATION PRESENTED TO THE GRADUATE COUNCIL OF
THE UNIVERSITY OF FLORIDA
IN PARTIAL FULFILLMENT OF THE REQUIREMENTS FOR THE
DEGREE OF DOCTOR OF PHILOSOPHY

UNIVERSITY OF FLORIDA

1976

To my wife, Jane

ACKNOWLEDGMENTS

It is not practical to list all those who assisted the author in the research leading to this dissertation; however a few must be mentioned for their especially important contributions.

Most important is Dr. Thomas A. Scott who suggested the problems and provided essential support, guidance, and assistance throughout all phases.

Mr. Paul Canepa was especially helpful with electronic and mechanical equipment and also assisted in taking data.

Dr. Atholl Gibson and Dr. James Brookeman must be thanked for their frequent and valuable consultations on both theoretical and experimental aspects.

Professor E.R. Andrew is to be thanked for the glycine crystals which were grown in his department at the University of Nottingham and also for the many helpful conversations during his visits to the University of Florida.

Mr. Ralph Warren and the rest of the men in the Physics Shop and Mr. Pat Coleman always managed to meet last minute requests for shop support and for liquid helium.

Other students and visiting scientists also shared their expertise and in some cases provided direct assistance, and finally, the typist, Adele Koehler, is to be congratulated on turning an illegible rough handwritten draft into such a fine job.

TABLE OF CONTENTS

	<u>Page</u>
ACKNOWLEDGMENTS	iii
LIST OF FIGURES	vii
ABSTRACT	x
CHAPTER	
I INTRODUCTION	1
1.1 High Field NQR of ^{14}N in Single Crystal Glycine . . .	1
1.2 NMR in Liquid and Solid Nitrogen	2
II THEORY	5
2.1 General	5
2.2 Intramolecular Dipolar Coupling	7
2.3 Nuclear Quadrupole Interaction	14
2.4 High Field Nuclear Quadrupole Interaction	21
2.5 Intramolecular Dipolar Splitting of the NMR Spectrum of ^{15}N in ^{15}N - ^{14}N Mixed Molecules	32
2.6 Nuclear Spin-Lattice Relaxation	41
2.6.1 General	41
2.6.2 The Hubbard Relation	46
III EXPERIMENTAL EQUIPMENT AND PROCEDURE	48
3.1 Superconductive Magnet System	48
3.1.1 Magnet	48
3.1.2 Dewars	57
3.1.3 Sample Probe	58
3.1.4 Operation of the Superconductive System	64

TABLE OF CONTENTS
(Continued)

	<u>Page</u>
3.2 Electromagnet System	67
3.2.1 Electromagnet	67
3.2.2 Cryostat and Sample System.	67
3.3 Spectrometers.	71
3.3.1 Pulse Spectrometer.	71
3.3.2 Continuous Wave Spectrometer.	74
IV RESULTS AND DISCUSSION - GLYCINE.	76
4.1 Glycine Structure.	76
4.2 Electric Field Gradient Tensors.	78
4.3 Data	89
4.4 Data Analysis.	98
4.5 Conclusions.	109
V RESULTS AND DISCUSSION -- NMR LINE SHAPE OF ^{15}N IN α NITROGEN WITH O_2 IMPURITY.	110
5.1 Structure of α Nitrogen.	110
5.2 Data	112
5.3 Data Analysis.	118
5.3.1 Paramagnetic O_2 Impurity.	118
5.3.2 Ortho-Para Conversion	127
5.3.3 ^{14}N Impurity.	128
5.3.4 Conclusions	133
VI RESULTS AND DISCUSSION - NMR SPECTRUM OF ^{15}N IN SOLID ^{15}N - ^{14}N	135
6.1 Sample	135
6.2 Data	135

TABLE OF CONTENTS
(Continued)

	<u>Page</u>
6.3 Computer Simulation.	140
6.4 Data Analysis.	140
6.4.1 Asymmetric Pake Doublet	141
6.4.2 Level Crossing.	141
6.5 Conclusions.	142
VII RESULTS AND DISCUSSION — NUCLEAR SPIN-LATTICE RELAXATION IN LIQUID AND SOLID $^{15}\text{N}_2$ AND $^{14}\text{N}_2$	143
7.1 Previous $^{15}\text{N}_2$ and $^{14}\text{N}_2$ Relaxation Time Studies	143
7.2 Data	148
7.3 Crystalline Structure of β -Solid Nitrogen.	150
7.4 Data Analysis.	153
7.5 Conclusions.	154
APPENDIX A.	156
LIST OF REFERENCES.	157
BIOGRAPHICAL SKETCH	159

LIST OF FIGURES

<u>Figure</u>	<u>Page</u>
1. Fake powder pattern doublet.	13
2. Comparison of z-axis projections of rotating vectors and tensor components.	24
3. Transformation between the lab axes and crystal axes during an X rotation	28
4. Temperature dependence of quadrupolar relaxation time.	44
5. Homogeneity of the superconductive magnet.	49
6. Differences between measured values of magnetic field and value calculated by exponential decay equation	51
7. Top access dewar system.	55
8. Re-entrant dewar system.	56
9. Sample probe, side view of sample holder	59
10. Sample probe, end view of sample holder.	60
11. Gas-flow temperature control system.	61
12. Cryostat used with electromagnet	68
13. Sample-gas system.	69
14. Glycine molecule	77
15. Typical α -glycine crystal.	79
16. Unit cell of α glycine	80
17. A vector \vec{r}_1 undergoing a 180° rotation about the Y axis would bring it to \vec{r}_2 , whereas a reflection in the X,Z plane would bring it to \vec{r}_3 , where $\vec{r}_2 = -\vec{r}_3$	81
18. Symmetry of rotation patterns for rotation axes in or normal to the X,Z plane.	82
19. C-axis rotation patterns from ^{14}N in α glycine at 5°C	91

LIST OF FIGURES
(continued)

<u>Figure</u>	<u>Page</u>
20. C-axis rotation patterns from ^{14}N in α glycine at 74°C . . .	92
21. C-axis rotation patterns from ^{14}N in α glycine at 148°C . . .	93
22. C-axis rotation patterns from ^{14}N in α glycine at 167°C . . .	94
23. Rotation patterns from ^{14}N in α glycine at 5°C using axis normal to (120) plane.	96
24. Relationship of U, V, W axes to X, Y, Z axes	99
25. Unit cell of αN_2	111
26. NMR spectrum of ^{15}N in αN_2 with 0.1% O_2 added at 625 and 950 G.	113
27. NMR spectrum of ^{15}N in αN_2 with 0.1% O_2 added at 2000, 3000, and 4000 G	114
28. NMR spectrum of ^{15}N in αN_2 with 0.1% O_2 added at 5000, 7000, and 9000 G	115
29. NMR spectrum of ^{15}N in αN_2 as a function of O_2 concentration.	116
30. Calculated NMR spectrum of protons which are nearest neighbors of O_2 impurity molecules in solid methane.	120
31. Possible superpositions of Pake doublet and paramagnetic spectrum which could explain data at 950 and 7000 G.	122
32. Calculated (---) and observed (—) NMR spectra of protons in $\text{NH}_4\text{Fe}(\text{SO}_4)_2$	123
33. Quadrupole transition frequencies of ^{14}N and Zeeman fre- quency of ^{15}N as a function of magnetic field H_0 and angle θ between H_0 and the molecular axis.	130
34. Qualitative effect on energy levels when the proton Zeeman transition energy matches a ^{14}N quadrupolar transition energy in $\text{SC}(\text{NH}_2)_2$	131
35. NMR spectra of ^{15}N in αN_2 enriched to 33% ^{15}N at 5000 and 6000 G	136
36. NMR spectra of ^{15}N in αN_2 enriched to 33% ^{15}N at 7000 and 9000 G	137

LIST OF FIGURES
(continued)

<u>Figure</u>	<u>Page</u>
37. Calculated NMR spectra of ^{15}N in α N_2 enriched to 33% ^{15}N at 5000 G.	138
38. Comparison of NMR spectra of ^{15}N in α N_2 enriched to 33% ^{15}N with computer simulation at 5000 and 7000 G.	139
39. Nitrogen spin-lattice relaxation times T_1 in $^{15}\text{N}_2$ (in seconds) and $^{14}\text{N}_2$ (in milliseconds).	145
40. Correlation times τ_Q and τ_{sr} in $^{14}\text{N}_2$ and $^{15}\text{N}_2$ respectively .	147
41. The reduced correlation time ($\tau^* = \tau(kT/I_0)^{1/2}$) τ_Q^* vs. τ_{sr}^* .	149
42. Crystal structure of β nitrogen.	152

Abstract of Dissertation Presented to the Graduate Council
of the University of Florida in Partial Fulfillment of the Requirements
for the Degree of Doctor of Philosophy

NUCLEAR MAGNETIC RESONANCE OF ^{14}N IN SINGLE CRYSTAL GLYCINE
AND OF ^{15}N IN LIQUID AND SOLID N_2

By

Lyle Milton Ishol

June, 1976

Chairman: Thomas A. Scott
Major Department: Physics

Quadrupole perturbed nuclear magnetic resonance (NMR) has been used to determine the quadrupole coupling constant e^2qQ/h , asymmetry parameter η , and electric field gradient (EFG) tensor in single crystal glycine. The results at room temperature are $e^2qQ/h = 1190$ kHz, $\eta = 0.505$, with the principal axis roughly parallel to the C-N bond direction. As the temperature increased, e^2qQ/h decreased. These results are consistent with earlier work, except there is no evidence of a significant change in the orientation of the EFG tensor at higher temperatures as reported earlier.

The NMR spectrum of ^{15}N in α -phase solid $^{15}\text{N}_2$ with paramagnetic O_2 impurity added has been determined as a function of magnetic field and O_2 concentration. A classical Pake doublet was obtained at 650 G as expected; however, the spectrum became increasingly asymmetric as the field was increased to a maximum of 9 kG. Increasing the O_2 concentration broadened the line but did not affect the asymmetry. Various

mechanisms may affect the line shape but none have been found to satisfactorily explain the asymmetry in all quantitative aspects.

The NMR spectrum of ^{15}N in an α -phase solid containing isotopic molecular species in the ratio $^{15}\text{N}_2 : ^{15}\text{N}-^{14}\text{N} : ^{14}\text{N}_2 = 1:4:4$ has been obtained as a function of magnetic field and compared with computer simulations. Besides the Pake doublet due to the $^{15}\text{N}_2$ molecules, an asymmetric triplet results from the $^{15}\text{N}-^{14}\text{N}$ mixed molecule. In the latter case the ^{14}N nucleus, which experiences a quadrupolar interaction comparable with the Zeeman Hamiltonian, produces a dipolar interaction at the ^{15}N nucleus which varies with the magnetic field in accordance with theoretical expectations. Additional effects occur due to level crossing and to the asymmetry of the Pake doublet mentioned above.

The nuclear spin-lattice relaxation time T_1 of ^{15}N has been measured in liquid $^{15}\text{N}_2$ for the temperature interval $63 < T < 77$ K and in the β -phase solid for $38 < T < 63$ K. The relaxation is attributed to the spin-rotational interaction in both the liquid and β solid. Any possible discontinuity in T_1 across the triple point is obscured by scatter in the data. When combined with previous T_1 data for $^{14}\text{N}_2$, it is concluded that a rotational diffusion model developed for liquids may hold in the β solid, and that the molecules reorient more slowly in the liquid than in the solid near the triple point.

CHAPTER I INTRODUCTION

1.1 High Field NQR of ^{14}N in Single Crystal Glycine

Nitrogen is an important atom in biological material, and nuclear quadrupole resonance of ^{14}N nuclei in biological molecules can provide information about the structure of the molecules. Problems arise due to the usually low atomic density and the low resonant frequencies which combine to give a poor signal-to-noise ratio. Glycine, for example, has a ^{14}N nuclear spin density of one nucleus per five C, O, and N atoms, not counting the five hydrogen atoms. Furthermore, there are two inequivalent sites, reducing the density of those participating in a resonance by a factor of two. The ^{14}N quadrupole coupling constant is about 1200 kHz at room temperature and increases only slightly at 77 K which, combined with the low density, results in a weak signal that is difficult to observe. To date, the pure quadrupole resonance has not been observed to the knowledge of the author.

Three research groups, Andersson, Gourdji, Guibe, and Proctor [1], Blinc, Mali, Osredkar, Prelesnik, Zupancic, and Ehrenberg [2], and Edmonds and Speight [3], have reported the quadrupole coupling constant e^2qQ/h and asymmetry parameter η of ^{14}N in glycine obtained from quadrupole perturbed NMR. References [1] and [2] also reported the quadrupole coupling tensor, or equivalently, the direction cosines of the principal axes of the tensor. Edmonds and Speight

[3] used a powder sample and therefore were unable to obtain the complete tensor.

Andersson et al. [1] used a wide-band Varian spectrometer and were able to obtain enough data to deduce the complete quadrupole coupling or electric field gradient (EFG) tensor at room temperature. They reported that the principal axis was roughly parallel to the axis of the NH_3 group. Blinc et al. [2] used pulsed double resonance methods at a temperature of 140°C , and reported the principal axis was about 60° away from the direction obtained by Andersson et al.; furthermore a much lower quadrupole coupling constant was deduced.

The purpose of the present experiment was two-fold. First, the laboratory had recently acquired a superconductive magnet capable of producing up to a 100-kG field and it was decided to employ it in an investigation of the use of a strong magnetic field to overcome the weak signal. Next, an attempt would be made to explain the differences between the data of Andersson et al. [1] and those of Blinc et al. [2].

1.2 NMR in Liquid and Solid Nitrogen

Nitrogen is an important and convenient substance for NMR studies for a number of reasons. Liquid nitrogen as a cryogenic fluid is readily available at low cost and requires no special handling other than that due to its low temperature. Aside from the attractive cost factor, it is advantageous to have the sample and the cryogenic fluid both the same, as it facilitates temperature and pressure control. A temperature region from about 50 K to 77 K in solid and liquid phases is easily attainable using liquid nitrogen.

More important than the practical aspects mentioned above are the physical properties. Two nonradioactive isotopes are available, the abundant ^{14}N with spin $I = 1$ and ^{15}N with $I = \frac{1}{2}$ which has only about 1/3% natural abundance. Three species of diatomic molecules are therefore available, $^{15}\text{N}_2$, $^{15}\text{N}-^{14}\text{N}$, and $^{14}\text{N}_2$.

Only three nonradioactive elements have spin $I = 1$, viz., ^{14}N , ^7Li , and ^2H . Lithium is a metal and deuterium is such a light atom that quantum effects are considerably more important than in the heavier ^{14}N . Therefore, ^{14}N occupies a rather unique position. As nuclei with spin $\frac{1}{2}$ have no quadrupole moment, nitrogen can be chosen with or without quadrupole interactions by selecting $^{14}\text{N}_2$ or $^{15}\text{N}_2$, respectively, and $^{15}\text{N}-^{14}\text{N}$ mixed molecules permit a study of unlike spin coupling. Three very different spin systems are therefore available with essentially the same lattice dynamics.

As implied by the name, nuclear spin-lattice relaxation depends on the coupling between nuclear spins and the lattice. The possibility of selecting either $I = 1$ or $I = \frac{1}{2}$ nuclei in essentially the same lattice turns out to be even more convenient in spin-lattice relaxation studies than the simple fact that the spins are different. It happens that the quadrupolar interaction is dominant in $^{14}\text{N}_2$ nuclear relaxation and spin-rotation interaction is dominant in $^{15}\text{N}_2$ relaxation as $^{15}\text{N}_2$ experiences no quadrupolar interaction. Hence, two fundamental relaxation processes can be isolated in the same environment. Furthermore, we will find the particular two processes are uniquely related in that a change in molecular dynamics due to a temperature change has opposite effects on the two processes.

It is also interesting to note that β nitrogen, stable from 35 K

to the triple point, 63 K, is a plastic crystal with low molecular orientational order. Thus rotational and orientational dependent properties in β -solid nitrogen have some similarities to the same properties in liquid nitrogen.

Finally, there are two crystalline forms readily obtained at low pressures, β nitrogen mentioned earlier, and α nitrogen, a much more rigid form, stable below 35 K. In α nitrogen, molecules undergo librational motion about fixed directions in the lattice. The effect of the librational motion for some purposes is to reduce the magnitude of the interaction by motional averaging. The resulting line shape is therefore unchanged except for an overall reduction in width due to the motional averaging. We therefore can conduct line shape studies of nuclei in molecules with like spin ($I = \frac{1}{2}$) or with unlike spin ($I = 1, \frac{1}{2}$) in the same crystalline structure.

The purpose of the present work is to study the line shape of ^{15}N in $^{15}\text{N}_2$ and in a mixture of $^{15}\text{N}_2$ and $^{15}\text{N}-^{14}\text{N}$ samples, and to study the spin-lattice relaxation times in liquid and β -solid $^{15}\text{N}_2$ and thereby fill a gap in existing nitrogen data. In so doing, contributions will also be made to the understanding of fundamental processes, such as spin-rotation interaction in solids, which will have applications to other systems.

CHAPTER II
THEORY

2.1 General

A nucleus with a magnetic moment $\vec{\mu}$ in a uniform external magnetic field \vec{H}_0 has an energy given by

$$E = -\vec{\mu} \cdot \vec{H}_0 \quad . \quad (2.1.1)$$

The quantum mechanical Hamiltonian is the well-known Zeeman term

$$\mathcal{H}_Z = -\vec{\mu} \cdot \vec{H}_0 = -\gamma \hbar \vec{I} \cdot \vec{H}_0 = -\gamma \hbar H_0 I_Z \quad (2.1.2)$$

where \vec{I} is the nuclear spin, γ is the gyromagnetic ratio, and $\vec{H}_0 = \hat{z} H_0$.

The Zeeman energy levels are

$$E_m = \langle m | \mathcal{H}_Z | m \rangle = -\gamma \hbar H_0 m \quad ,$$

or

$$E_m = \hbar \omega_0 m \quad , \quad (2.1.3)$$

where $\omega_0 = -\gamma H_0$.

Transitions between levels may be induced by application of a small rotating magnetic field, perpendicular to \vec{H}_0 ,

$$H_x = H_1 \cos \omega t, \quad H_y = H_1 \sin \omega t \quad , \quad (2.1.4)$$

as a perturbation of \vec{H}_0 . In practice, an alternating magnetic field is applied which can be thought of as the sum of two counter-rotating components. It will be seen later that only one component is effective in inducing transitions.

The perturbing Hamiltonian is

$$H_1 = -\gamma \hbar (H_x I_x + H_y I_y) = -\frac{1}{2} \gamma \hbar H_1 (I_+ e^{-i\omega t} + I_- e^{i\omega t}) \quad (2.1.5)$$

where the raising and lowering operators $I_{\pm} = I_x \pm iI_y$ have been introduced. These operators have nonvanishing matrix elements only between states for which m differs by one, so the only transitions allowed will differ in energy by $\Delta E = \hbar \omega_0$. Thus, the frequency of the perturbing alternating magnetic field must be ω_0 in order to induce transitions. The counter-rotating component $-\omega_0$ is $2\omega_0$ off resonance and can be ignored for most purposes. The resonant condition, $\omega = \omega_0$, allows an exchange of energy between the spin system and the alternating field, and this exchange can be observed electronically if the net exchange is not zero.

The nucleus experiences not only the external field \vec{H}_0 , but also fields, both electric and magnetic, due to its surroundings. Neighboring nuclei with magnetic moments influence the nucleus of interest through dipole-dipole coupling. Net electrostatic forces may be

exerted on a nucleus with a nonspherical charge distribution. While a molecule is rotating, its charges cause a magnetic field at the sites of its own nuclei, giving rise to spin-rotation interaction. There are other interactions which are less important in the present work, and will be disregarded.

An isolated nucleus would resonate at ω_0 , providing no information other than the Zeeman frequency. In practice, effects such as those mentioned above modify the behavior of the nucleus by adding to the applied field or by causing other forces on the nucleus. The nuclei therefore resonate at different frequencies, depending on their surroundings. The frequency spectrum therefore provides information about the surroundings and about the interactions taking place.

In order for there to be a net exchange of energy between the alternating field and the spin system, the spins must have a net exchange of energy with a third system, the lattice. This takes place through the interactions mentioned above as well as through some other interactions less important here, and the rate of the interaction is characterized by a spin-lattice relaxation time T_1 .

Much of the discussion below will follow Abragam [4], Andrew [5], Cohen and Reif [6], or possibly other standard references, and will not be specifically referenced at each step.

2.2 Intramolecular Dipolar Coupling

Consider one nucleus i at the origin P , and a second nucleus j at \vec{r} , with magnetic moments $\vec{\mu}_i$ and $\vec{\mu}_j$, respectively. The magnetic potential at P due to $\vec{\mu}_j$ is

$$\phi_{ij} = -\vec{\mu}_j \cdot \nabla(1/r_{ij}) \quad (2.2.1)$$

and the magnetic field is

$$\vec{H}_{ij} = -\nabla\phi_{ij} \quad (2.2.2)$$

Performing the indicated operations results in

$$\vec{H}_{ij} = -[\vec{\mu}_j - 3\vec{r}_{ij}(\vec{\mu}_j \cdot \vec{r}_{ij})/r_{ij}^2] r_{ij}^{-3} \quad (2.2.3)$$

The dipolar Hamiltonian, obtained by letting $\vec{H}_0 = \vec{H}_{ij}$ in Eq. (2.1.2), is

$$\mathcal{H}_D = -\vec{\mu}_i \cdot \vec{H}_{ij} = [\vec{\mu}_i \cdot \vec{\mu}_j - 3(\vec{\mu}_i \cdot \vec{r}_{ij})(\vec{\mu}_j \cdot \vec{r}_{ij})/r_{ij}^2] r_{ij}^{-3}, \quad (2.2.4)$$

as \vec{H}_{ij} interacts with the nucleus i the same way as \vec{H}_0 . If an external field $\vec{H}_0 = \hat{z}H_0$ is now applied, where $H_0 \gg H_{ij}$, the total Hamiltonian of the two nuclei is

$$\mathcal{H} = -\gamma_i \hbar H_0 I_{iz} - \gamma_j \hbar H_0 I_{jz} + \frac{\hbar^2 \gamma_i \gamma_j}{r_{ij}} \left[\vec{I}_i \cdot \vec{I}_j - \frac{3(\vec{I}_i \cdot \vec{r}_{ij})(\vec{I}_j \cdot \vec{r}_{ij})}{r_{ij}^2} \right] \quad (2.2.5)$$

Letting

$$W_{ij} = \vec{I}_i \cdot \vec{I}_j - \frac{3(\vec{I}_i \cdot \vec{r}_{ij})(\vec{I}_j \cdot \vec{r}_{ij})}{r_{ij}^2}, \quad (2.2.6)$$

it is customary to write

$$W_{ij} = A + B + C + D + E + F \quad (2.2.7)$$

where

$$A = I_{iz} I_{jz} (1 - 3\cos^2\theta)$$

$$B = -(\frac{1}{4})(I_{i+} I_{j-} + I_{i-} I_{j+}) (1 - 3\cos^2\theta)$$

$$C = -(3/2)(I_{iz} I_{j+} + I_{jz} I_{i+}) \sin\theta \cos\theta e^{-i\phi}$$

$$D = -(3/2)(I_{iz} I_{j-} + I_{jz} I_{i-}) \sin\theta \cos\theta e^{i\phi} = C^*$$

$$E = -(3/4)(I_{i+} I_{j+}) \sin^2\theta e^{-2i\phi}$$

$$F = -(3/4)(I_{i-} I_{j-}) \sin^2\theta e^{2i\phi} = E^* \quad (2.2.8)$$

The field (2.2.3) \vec{H}_{ij} is on the order of 1 G, whereas \vec{H}_0 is 10^3 or 10^4 G, so \mathcal{H}_D may be treated as a perturbation of \mathcal{H}_Z . Restricting the problem to like spin $\frac{1}{2}$ nuclei, the zero-order energy level is $E_Z = -\gamma\hbar H_0 (m_i + m_j)$, and according to first-order perturbation theory, only those parts of the perturbing Hamiltonian which induce no net change in $M = m_i + m_j$ contribute to the energy. Inspection of Eq. (2.2.8) shows only terms A and B fit this condition, and terms C through F may be disregarded here. These terms actually permit weak

resonances at 0 and $2\omega_0$ frequencies, which are of no interest in the present work. The truncated Hamiltonian, good to an excellent approximation, is therefore

$$\mathcal{H} = -\gamma\hbar H_0 (I_{iz} + I_{jz}) + \frac{\gamma^2 \hbar^2}{3 r_{ij}^2} (1 - 3\cos^2\theta) [I_{iz} I_{jz} - (\frac{1}{2})(I_{i+} I_{j-} + I_{i-} I_{j+})] . \quad (2.2.9)$$

It is noted that term A can be interpreted as nucleus i experiencing the average field due to nucleus j, whereas term B is the simultaneous 'flipping' of both spins, which can occur when i and j are like nuclei and therefore in resonance.

There are four states for the case of two spin $\frac{1}{2}$ nuclei, represented by $|++\rangle$, $|+-\rangle$, $| -+\rangle$, $|--\rangle$. Term B has no diagonal matrix elements in this representation; however, linear combinations may be used to define a triplet state,

$$\begin{aligned} |+\rangle &= |++\rangle \\ |0\rangle &= (1/\sqrt{2})(|+-\rangle + | -+\rangle) \\ |-\rangle &= |--\rangle \end{aligned} \quad (2.2.10)$$

and a singlet state, $|0\rangle_s = (1/\sqrt{2})(|+-\rangle - | -+\rangle)$. The singlet state has no Zeeman energy and isn't coupled to the triplet state by either \mathcal{H}_D or \mathcal{H}_Z , and may be ignored.

Energy levels are readily calculated and are

$$E_1 = -\gamma\hbar H_0 + (\gamma^2 \hbar^2 / 4r^3) (1 - 3\cos^2\theta)$$

$$E_0 = - (\gamma^2 \hbar^2 / 2r^3) (1 - 3\cos^2 \theta)$$

$$E_{-1} = \gamma \hbar H_0 + (\gamma^2 \hbar^2 / 4r^3) (1 - 3\cos^2 \theta) \quad (2.2.11)$$

In the remainder of this section only identical spin $\frac{1}{2}$ nuclei in diatomic molecules will be considered, whose intramolecular separation is significantly less than the intermolecular nuclear separation. Thus, the i, j subscripts may be dropped, as the $1/r^3$ factor insures intramolecular effects dominate.

Two resonant frequencies may be observed at constant H_0 ,

$$\hbar \omega' = E_{-1} - E_0 = \gamma \hbar [H_0 + \alpha(1 - 3\cos^2 \theta)]$$

$$\hbar \omega'' = E_0 - E_1 = \gamma \hbar [H_0 - \alpha(1 - 3\cos^2 \theta)] \quad (2.2.12)$$

where $\alpha = 3\gamma \hbar / 4r^3$. Or H_0 could be varied and $\omega = \omega' = \omega''$ held fixed, the resonant condition being found at two values of H_0 ,

$$H_0 = H^* \pm \alpha(3u^2 - 1) \quad , \quad (2.2.13)$$

where $H^* = \omega/\gamma$ and $u = \cos \theta$. H^* is the constant central, or Zeeman, field, and u is the cosine of the angle θ between \vec{H}_0 and \vec{r} .

In a polycrystalline sample, any orientation is equally likely, and for each orientation, there will be two resonant lines, above or below H^* by an amount

$$h = H_0 - H^* = \pm(3u^2 - 1) \quad . \quad (2.2.14)$$

The spectral distribution is just a plot of the density of lines (or density of orientations) versus h , so the density of orientations must be known as a function of u .

A sphere can be defined by all possible positions of the second nucleus if the first is held fixed, and the density of positions is constant over the surface of the sphere. Remembering $r \cos \theta = ru$ is the projection of r along $\vec{H}_0 = \hat{z}H_0$, it is noted that any value of u defines a circle on the sphere, and a plane containing the circle is normal to \hat{z} at a distance ru above the center of the sphere. Another plane and circle are defined by $u + \Delta u$, the planes being separated by $r\Delta u$. The surface of a sphere between two planes separated by d is $2\pi r d$, so the surface area between the planes defined by u and $u + \Delta u$ is $2\pi r^2 \Delta u$, independent of u itself. Therefore any value of u is equally probable, and the spectrum can be considered a plot of the density of u 's versus h , or du/dh .

From (2.2.14)

$$u \propto \left(\frac{h}{\pm\alpha} + 1 \right)^{1/2} \quad (2.2.15)$$

and the spectral distribution, $f(h)$, is

$$f(h) = \frac{du}{dh} \propto \left(\frac{h}{\pm\alpha} + 1 \right)^{-1/2} \quad . \quad (2.2.16)$$

In the case of ^{15}N , $\gamma = -|\gamma|$, so (2.2.16) becomes

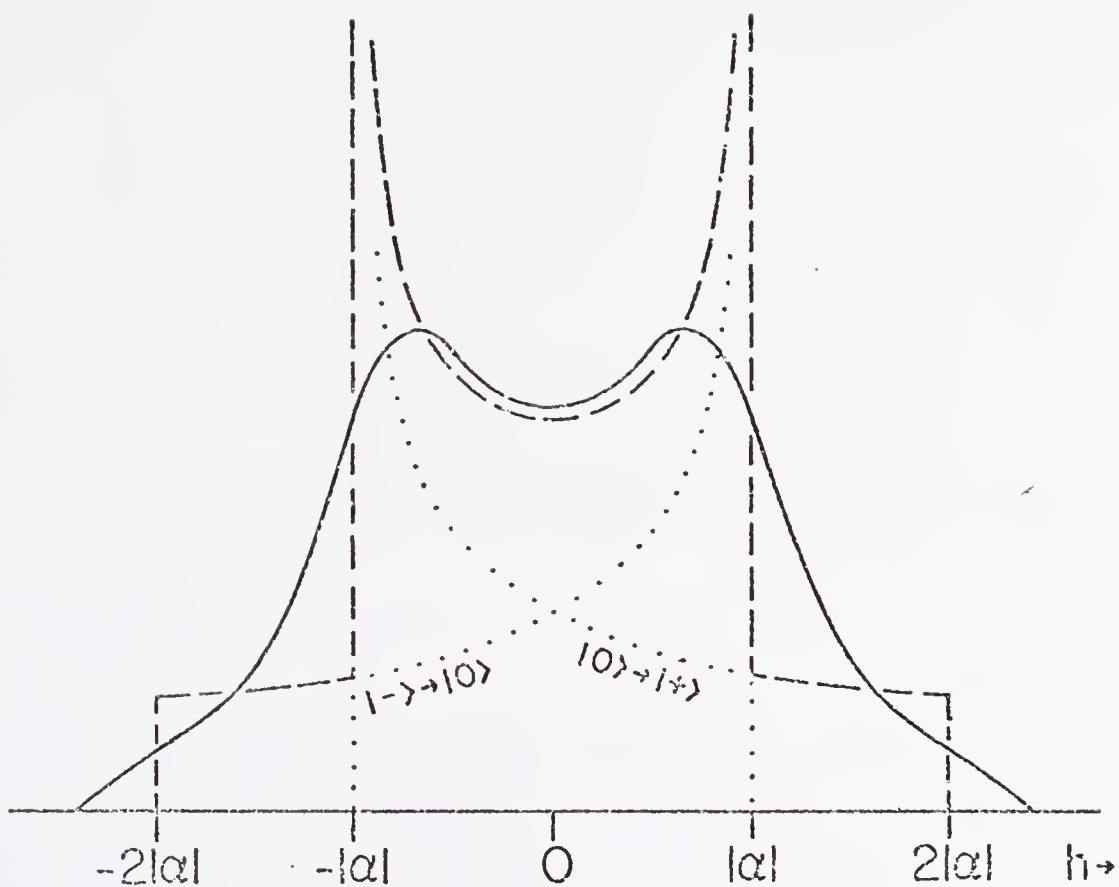


Figure 1. Pake powder pattern doublet. The theoretical unbroadened spectrum (dashed line) is the sum of the two components (dotted lines) resulting from the transitions shown which are for the case of a negative gyromagnetic ratio. A typical spectrum including intermolecular broadening is shown by the solid line.

$$f(h) \propto \left(\frac{h}{\pm|\alpha|} + 1 \right)^{-\frac{1}{2}} \quad (2.2.17)$$

the upper (lower) sign corresponding to the $|-\rangle \rightarrow |0\rangle$ ($|0\rangle \rightarrow |+\rangle$) transition. From (2.2.14), we note

$$\begin{aligned} -2|\alpha| \leq h \leq |\alpha| & \quad |-\rangle \rightarrow |0\rangle \\ -|\alpha| \leq h \leq 2|\alpha| & \quad |0\rangle \rightarrow |+\rangle \end{aligned} \quad (2.2.18)$$

The two curves overlap in the region $-|\alpha| \leq h \leq |\alpha|$, and result in a spectrum indicated by the dashed line in Fig. 1. Intermolecular dipolar coupling causes each line to be broadened, resulting in a curve such as that shown in Fig. 1 by the solid line. The spectrum shown in Fig. 1 is known as the Pake doublet after G.E. Pake [7]. It should be noted that the curve will be reversed if frequency units vice magnetic field units are used, in addition to a scale factor set by the gyromagnetic ratio.

2.3 Nuclear Quadrupole Interaction

The charge distribution in a nonspherical nucleus exhibits an orientational-dependent interaction with the surrounding electric field due to the external charge distribution. Classically, this may be written as

$$E = \int \rho(\vec{r}) \phi(\vec{r}) d^3r \quad (2.3.1)$$

where $\rho(\vec{r})$ is the nuclear charge density and $\phi(\vec{r})$ is the potential due

to external charges.

One convenient method of treating the problem is a Taylor series expansion of $\phi(\vec{r})$ about the origin:

$$E = \phi(0) \int \rho d^3r + \sum_{\alpha} \phi_{\alpha} \int x_{\alpha} \rho d^3r + \frac{1}{2!} \sum_{\alpha, \beta} \phi_{\alpha\beta} \int x_{\alpha} x_{\beta} \rho d^3r + \dots \quad (2.3.2)$$

where x_{α} ($\alpha = 1, 2, 3$) stands for x, y, z respectively, and where

$$\phi_{\alpha} \equiv \left. \frac{\partial \phi}{\partial x_{\alpha}} \right|_{r=0}, \quad \phi_{\alpha\beta} \equiv \left. \frac{\partial^2 \phi}{\partial x_{\alpha} \partial x_{\beta}} \right|_{r=0}, \quad \text{etc.} \quad (2.3.3)$$

The first term in the expansion is the electrostatic energy of the nucleus taken as a point charge, and is of no interest as it is just a constant with no orientational dependence. The second, or dipole, term vanishes as nuclear theory tells us the wave function has definite parity so $\rho(\vec{r}) = \rho(-\vec{r})$, and since x_{α} changes sign in opposite quadrants, the dipole integral vanishes. For the same reason, all the even terms vanish.

The terms in the expansion are referred to as monopole, dipole, quadrupole, octopole, hexadecapole, etc., as they are identified with the type of charge distribution which would cause the corresponding potential. We have shown the dipole, octopole, and every other higher term vanishes and the monopole term exists but is of no interest. This leaves the quadrupole, hexadecapole, and higher terms:

$$E = \frac{1}{2} \sum_{\alpha, \beta} \phi_{\alpha\beta} \int x_{\alpha} x_{\beta} \rho d^3r + \text{hexadecapole and higher} \quad (2.3.4)$$

Now $\phi(0)$ is roughly e/r_e , where r_e is of the order of the radius of an electron orbit, so the monopole term $\phi(0) \int \rho d^3r$ is on the order of Ze^2/r_e . The next nonzero term, $\partial^2 \phi / \partial x_\alpha \partial x_\beta \int x_\alpha x_\beta \rho d^3r$, is on the order of $(e/r_e^3)(r_n^2 Ze) = (r_n^2/r_e^2)(Ze^2/r_e)$ where r_n is on the order of a nuclear radius. As $r_n^2/r_e^2 \approx 10^{-8}$, the quadrupole term is on the order of 10^{-8} times the monopole term. Likewise, the hexadecapole term is on the order of 10^{-8} times the quadrupole term and so on for succeeding terms. Thus, the quadrupole term is the only one of interest within the resolution of most spectrometers.

If we replace ρ with its quantum mechanical equivalent ρ_{op} and define the symmetric tensor $Q'_{\alpha\beta} = \int x_\alpha x_\beta \rho_{op} d^3r$, we have the quadrupolar Hamiltonian to an excellent approximation,

$$\mathcal{H}_Q = \frac{1}{2} \sum_{\alpha, \beta} \phi_{\alpha\beta} Q'_{\alpha\beta} \quad . \quad (2.3.5)$$

It is convenient to substitute the symmetric, traceless tensor

$$Q_{\alpha\beta} = 3Q'_{\alpha\beta} - \delta_{\alpha\beta} \sum_{\sigma} Q'_{\sigma\sigma} \quad (2.3.6)$$

in Eq. (2.3.5) which then becomes

$$\mathcal{H}_Q = \frac{1}{6} \sum_{\alpha, \beta} \phi_{\alpha\beta} Q_{\alpha\beta} + \frac{1}{6} \left(\sum_{\alpha} \phi_{\alpha\alpha} \right) \left(\sum_{\sigma} Q'_{\sigma\sigma} \right) \quad . \quad (2.3.7)$$

The potential is due to charges outside the nucleus, and therefore satisfies Laplace's equation, so $\phi_{\alpha\alpha}$ is traceless and hence the second term in Eq. (2.3.7) vanishes. Here we are neglecting any electronic

charge distribution which is overlapping the nucleus as it is very small, especially after subtracting the spherically symmetric part which is of no interest in orientational studies. We are therefore left with

$$\mathcal{H}_Q = \frac{1}{6} \sum_{\alpha, \beta} \phi_{\alpha\beta} Q_{\alpha\beta} \quad . \quad (2.3.8)$$

From Eq. (2.3.6) and the definition of $Q'_{\alpha\beta}$, we have

$$Q_{\alpha\beta} = \int (3x_{\alpha}x_{\beta} - \delta_{\alpha\beta}r^2)\rho_{op}d^3r \quad . \quad (2.3.9)$$

Putting in $\rho_{op}(\vec{r}) = \sum_{\mathbf{k}} q_{\mathbf{k}}\delta(\vec{r} - \vec{r}_{\mathbf{k}})$, and performing the integration results in

$$Q_{\alpha\beta} = e \sum_{\mathbf{k}} (3x_{\alpha\mathbf{k}}x_{\beta\mathbf{k}} - \delta_{\alpha\beta}r_{\mathbf{k}}^2) \quad (2.3.10)$$

where e is the charge of a proton and the sum is over the protons in the nucleus. The expression in the parentheses could be written

$$Q_{\alpha\beta\mathbf{k}} = \frac{3(x_{\alpha\mathbf{k}}x_{\beta\mathbf{k}} + x_{\beta\mathbf{k}}x_{\alpha\mathbf{k}})}{2} - \delta_{\alpha\beta}r_{\mathbf{k}}^2 \quad . \quad (2.3.11)$$

We now look at another operator

$$I_{\alpha\beta}(op) = \frac{3(I_{\alpha}I_{\beta} + I_{\beta}I_{\alpha})}{2} - \delta_{\alpha\beta}I^2 \quad , \quad (2.3.12)$$

and assert

$$\langle \text{Im} | Q_{\alpha\beta} | \text{Im}' \rangle = C \langle \text{Im} | (3/2)(I_{\alpha} I_{\beta} + I_{\beta} I_{\alpha}) - \delta_{\alpha\beta} \vec{I}^2 | \text{Im}' \rangle \quad (2.3.13)$$

We notice the two operators are constructed in the same way and that $Q_{\alpha\beta}$ is a linear combination of the $Q_{\alpha\beta k}$'s. The two operators obey three conditions: 1) they are symmetric, 2) they are traceless, and 3) they transform under rotation of coordinate axes in the same way as second order spherical harmonics. This last condition is equivalent to saying they are second rank tensor operators, or that they satisfy the same commutation rules with respect to \vec{I} . These three conditions are sufficient, using group theory, to prove Eq. (2.3.13) [8]. A more sophisticated proof calls on the Wigner-Eckart theorem which shifts the complexity to the proof of the theorem. A simpler, more direct proof, but also more tedious, comes from direct matrix multiplication [8].

Remembering $Q_{\alpha\beta}$ was related to the quadrupole portion of the nuclear charge distribution, we define the quadrupole moment Q by

$$eQ = \langle \text{II} | Q_{zz} | \text{II} \rangle \quad (2.3.14)$$

which is used in Eq. (2.3.13) to obtain

$$eQ = C \langle \text{II} | 3I_z^2 - \vec{I}^2 | \text{II} \rangle = C I(2I - 1) \quad (2.3.15)$$

from which we obtain $C = eQ/I(2I - 1)$.

Equation (2.3.8) can be rewritten

$$\mathcal{H}_Q = \frac{1}{6} \frac{eQ}{I(2I - 1)} \sum_{\alpha, \beta} \phi_{\alpha\beta} \left[\frac{3}{2} (I_\alpha I_\beta + I_\beta I_\alpha) - \delta_{\alpha\beta} \vec{I}^2 \right] . \quad (2.3.16)$$

We can diagonalize $\phi_{\alpha\beta}$ and hereafter assume we have done so and use α, β without primes to indicate the coordinate system in which $\phi_{\alpha\beta}$ is diagonal. Thus,

$$\mathcal{H}_Q = \frac{1}{6} \frac{eQ}{I(2I - 1)} \sum_{\alpha} Q_{\alpha\alpha} (3I_\alpha^2 - \vec{I}^2) . \quad (2.3.17)$$

Labeling the axes is arbitrary, so we define a principal axes frame by

$$|\phi_{zz}| \geq |\phi_{yy}| \geq |\phi_{xx}| , \quad (2.3.18)$$

and in this frame

$$\mathcal{H}_Q = \frac{1}{6} \frac{eQ}{I(2I - 1)} \left[\phi_{xx} (3I_x^2 - \vec{I}^2) + \phi_{yy} (3I_y^2 - \vec{I}^2) + \phi_{zz} (3I_z^2 - \vec{I}^2) \right] . \quad (2.3.19)$$

With the help of Laplace's equation, $\phi_{xx} + \phi_{yy} + \phi_{zz} = 0$,

$$\mathcal{H}_Q = \frac{1}{4} \frac{eQ}{I(2I - 1)} \left[\phi_{zz} (3I_z^2 - \vec{I}^2) + (\phi_{xx} - \phi_{yy}) (I_x^2 - I_y^2) \right] . \quad (2.3.20)$$

Introducing $A = e^2 q Q / 4I(2I - 1)$, $\eta = (\phi_{xx} - \phi_{yy}) / \phi_{zz}$, $e q = \phi_{zz}$, and the raising and lowering operators $I_{\pm} = (I_x \pm iI_y)$, we obtain

$$\mathcal{H}_Q = A \left[3I_z^2 - \vec{I}^2 + (\eta/2) (I_+^2 + I_-^2) \right] . \quad (2.3.21)$$

If we were to calculate matrix elements for $I = 0$ or $I = \frac{1}{2}$ using Eq. (2.3.17), we would find all terms vanish, which means the electric quadrupole interaction exists only for $I \geq 1$. Semiclassically, we would expect no orientational dependence for $I = 0$ which has no z component, and $I = \frac{1}{2}$ has two states, $+\frac{1}{2}$ and $-\frac{1}{2}$, which correspond to a reversal of spin direction but no change in charge distribution and again no orientational dependence.

We have introduced the electric quadrupole moment Q , the electric field gradient (in the direction of maximum gradient) q , the asymmetry parameter η , and a quantity $A = e^2 q Q / 4I(2I - 1)$. We notice $\eta = 0$ when $\phi_{xx} = \phi_{yy}$, which occurs in spherical, cylindrical, or cubic symmetry, hence the name asymmetry parameter. The maximum value η can have is unity when $\phi_{xx} = 0$ and $|\phi_{yy}| = |\phi_{zz}|$. We also note that q and Q can not be determined individually in a nuclear quadrupole resonance experiment as they appear only as a product. The quantity $e^2 q Q / h$ is called the quadrupole coupling constant, and it is convenient to include it in the constant A .

The quantization direction of the nuclear quadrupole interaction is set by the z principal axis which is the direction of the maximum electric field gradient. If other interactions are present, they in general will have different quantization directions. In the presence of an external magnetic field, for instance, the Zeeman Hamiltonian \mathcal{H}_Z (discussed in Sec. 2.2) is diagonal in a coordinate system with the z axis parallel to the external field which in general does not coincide with the z principal axis. Low magnetic field and high magnetic field cases can be treated by first-order perturbation theory. The intermediate case with the two interactions of comparable

magnitude must be solved exactly and results in a much more complex orientational dependence. The low magnetic field case is of little interest in the present experiments and will not be discussed. The high field case will be treated in Sec. 2.4 and the intermediate region in Sec. 2.5.

2.4 High Field Nuclear Quadrupole Interaction

If a system of identical spins is placed in a magnetic field, the well-known Zeeman Hamiltonian is

$$\mathcal{H}'_Z = -\gamma\hbar H_0 I_z', \quad (2.4.1)$$

from Eq. (2.1.2), the prime being used to distinguish the coordinate system in which \mathcal{H}'_Z is diagonal.

If nuclear quadrupole interactions are also present, we must add the quadrupolar Hamiltonian, Eq. (2.3.21):

$$\mathcal{H} = \mathcal{H}'_Z + \mathcal{H}'_Q = -\gamma\hbar H_0 I_z' + A \left[3I_z'^2 - I^2 + \frac{\eta}{2} (I_+^2 + I_-^2) \right]. \quad (2.4.2)$$

The unprimed coordinate system refers to the principal axes frame.

Restricting the discussion to the high field approximation where first-order perturbation theory is valid for \mathcal{H}'_Q , we are only interested in the diagonal matrix elements, $\langle m | \mathcal{H} | m \rangle$. It is convenient at this point to return to Eq. (2.3.15) which, using $\phi_{xx} + \phi_{yy} + \phi_{zz} = 0$, becomes

$$\mathcal{H}_Q = \frac{eQ}{2I(2I - 1)} (\phi_{xx} I_x^2 + \phi_{yy} I_y^2 + \phi_{zz} I_z^2) \quad . \quad (2.4.3)$$

Writing the direction cosine of x_α with respect to x'_β as $a_{\alpha\beta}$, where x_α , $\alpha = 1,2,3$ stands for x, y, z , and x'_β , $\beta = 1,2,3$ stands for x', y', z' , we have

$$I_\alpha = \sum_{\beta} a_{\alpha\beta} I_\beta \quad . \quad (2.4.4)$$

Thus,

$$I_x^2 = a_{11}^2 I_{x'}^2 + a_{12}^2 I_{y'}^2 + a_{13}^2 I_{z'}^2 + \text{cross terms} \quad (2.4.5)$$

and likewise for I_y^2 and I_z^2 . We are considering only diagonal matrix elements and cross product terms like $\langle m | a_{11} a_{12} (I_{x'} I_{y'} + I_{y'} I_{x'}) | m \rangle$ vanish and may be dropped for our purposes.

Putting Eq. (2.4.4) in Eq. (2.4.3) results in

$$\begin{aligned} \mathcal{H}_Q = \frac{eQ}{2I(2I - 1)} & \left[\phi_{xx} (a_{11}^2 I_{x'}^2 + a_{12}^2 I_{y'}^2 + a_{13}^2 I_{z'}^2) \right. \\ & \left. + \phi_{yy} (a_{21}^2 I_{x'}^2 + a_{22}^2 I_{y'}^2 + a_{23}^2 I_{z'}^2) + \phi_{zz} (a_{31}^2 I_{x'}^2 + a_{32}^2 I_{y'}^2 + a_{33}^2 I_{z'}^2) \right] \quad . \end{aligned} \quad (2.4.6)$$

It is easy to show that

$$\langle m | I_x^2 | m \rangle = \langle m | I_y^2 | m \rangle = \frac{1}{2} \langle m | \vec{I}^2 - I_z^2 | m \rangle = \frac{1}{2} [I(I + 1) - m^2] \quad . \quad (2.4.7)$$

As the only allowed transitions are those for which $\Delta m = \pm 1$, we calculate

$$\langle m | I_x^2 | m \rangle - \langle m - 1 | I_x^2 | m - 1 \rangle = -\frac{1}{2}(2m - 1)$$

$$\langle m | I_z^2 | m \rangle - \langle m - 1 | I_z^2 | m - 1 \rangle = (2m - 1) \quad (2.4.8)$$

The transitions $\Delta E_{Q(m \rightarrow m - 1)} = \langle m | \mathcal{H}'_Q | m \rangle - \langle m - 1 | \mathcal{H}'_Q | m - 1 \rangle$ are then evaluated, yielding

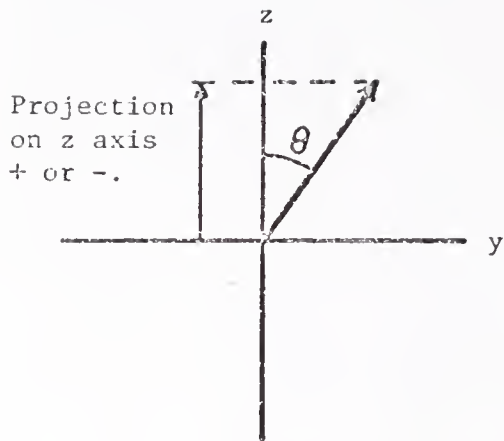
$$\begin{aligned} \Delta E_{Q(m \rightarrow m - 1)} &= \frac{eQ(2m - 1)}{2I(2I - 1)} \left[\phi_{xx} \left(-\frac{a_{11}^2}{2} - \frac{a_{12}^2}{2} + a_{13}^2 \right) + \phi_{yy} \left(-\frac{a_{21}^2}{2} - \frac{a_{22}^2}{2} + a_{23}^2 \right) \right. \\ &\quad \left. + \phi_{zz} \left(-\frac{a_{31}^2}{2} - \frac{a_{32}^2}{2} + a_{33}^2 \right) \right] \\ &= \frac{eQ(2m - 1)}{2I(2I - 1)} \left(\frac{3}{2} \phi_{xx} a_{13}^2 + \frac{3}{2} \phi_{yy} a_{23}^2 + \frac{3}{2} \phi_{zz} a_{33}^2 \right) \quad (2.4.9) \end{aligned}$$

From Eq. (2.4.8) we see that $E_{Q(-m + 1 \rightarrow -m)} = -E_{Q(m \rightarrow m - 1)}$ and from Sec. 2.1, $\Delta E_{Z(m \rightarrow m - 1)} = \Delta E_{Z(-m + 1 \rightarrow -m)} = -\gamma \hbar H_0$. Hence the observed transitions are in pairs,

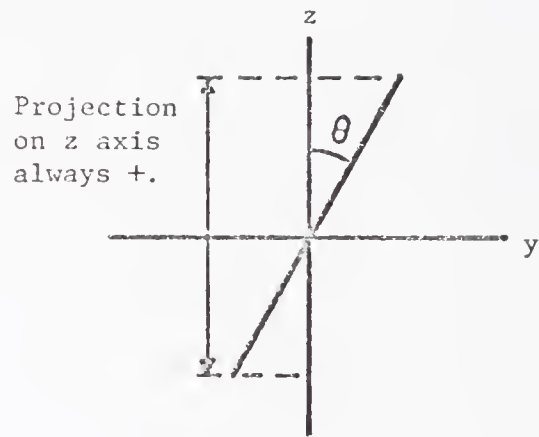
$$\Delta E_{\pm} = \Delta E_Z \pm \Delta E_Q \quad (2.4.10)$$

where the upper sign signifies the $(m \rightarrow m - 1)$ transition and the lower sign the $(-m + 1 \rightarrow -m)$ transition.

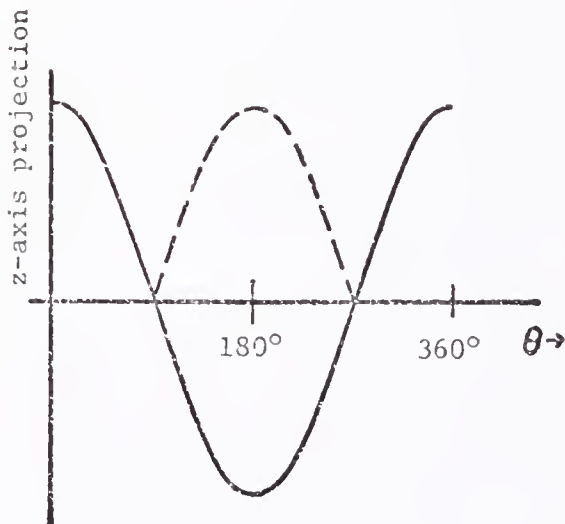
We are not concerned with the Zeeman term which depends only on



a. Vector



b. Tensor



c. Projections of vector (—) and tensor component (---) on z axis.

Figure 2. Comparison of z-axis projections of rotating vectors and tensor components. The period of the tensor component is $\frac{1}{2}$ that of the vector.

H_0 and the nuclear species. It is sufficient to measure the difference in energies between the two transitions, which is $2\Delta E_Q$. In frequency units,

$$2\Delta\nu = \frac{3eQ(2m - 1)}{2I(2I - 1)\hbar} (\phi_{xx} a_{13}^2 + \phi_{yy} a_{23}^2 + \phi_{zz} a_{33}^2) \quad (2.4.11)$$

This is a convenient point at which to note the physical interpretation of the frequency separation $2\Delta\nu$ in terms of the orientation of the external field \vec{H}_0 with respect to the principal axes x, y, z . We recall a_{13} is the direction cosine of the x principal axis with respect to the direction of \vec{H}_0 (which is parallel to z') and likewise for a_{23} and a_{33} . Thus, $\phi_{xx} a_{13}^2$ is the magnitude of the x component of the electric field gradient tensor times the square of the cosine of the angle between the x component and \vec{H}_0 , and so on for the other terms. We note ϕ_{xx} and ϕ_{yy} have the same sign, which is opposite to the sign of ϕ_{zz} .

The observed frequency shift $\Delta\nu$ is proportional to the sum of the three 'projections', remembering the z component is opposite in sign to the others.

We also note here the significance of the square of the cosine. If the EFG components were simple vectors which have a direction and sense (or sign), we would expect any effects to reverse signs every 180° as shown in Fig. 2. Noting in Fig. 2(c) that the tensor 'projection' goes through two complete cycles in a 360° rotation, we expect a 2θ to appear which will come from the cosine squared factors.

In general, the orientations of the principal axes are unknown as are the magnitudes of the $\phi_{\alpha\alpha}$'s. We therefore express the EFG

tensor in the lab frame. Using $a_{\alpha\beta}$, as before and the fact that $\phi_{\alpha\beta}$ is diagonal ($\phi_{\alpha\beta} = \delta_{\alpha\beta} \phi_{\alpha\beta}$) we have

$$\begin{aligned} \phi_{x'_\alpha x'_\beta} &= \sum_{\gamma, \delta} (a^{-1})_{\alpha\gamma} \phi_{\gamma\delta} a_{\delta\beta} = \sum_{\gamma, \delta} a_{\gamma\alpha} \delta_{\gamma\delta} \phi_{\gamma\delta} a_{\delta\beta} \\ &= \sum_{\delta} a_{\delta\alpha} \phi_{\delta\delta} a_{\delta\beta} \end{aligned} \quad (2.4.12)$$

and therefore

$$\phi_{z'z'} = \sum_{\delta} a_{\delta 3} \phi_{\delta\delta} a_{\delta 3} = a_{13}^2 \phi_{xx} + a_{23}^2 \phi_{yy} + a_{33}^2 \phi_{zz} \quad (2.4.13)$$

Finally, Eq. (2.4.11) becomes

$$2\Delta v = \frac{3eQ(2m-1)}{2I(2I-1)\hbar} \phi_{z'z'} = K \phi_{z'z'} \quad (2.4.14)$$

with the definition of K obvious.

We are interested in finding $e^2 qQ/h$ (or $A = e^2 qQ/4I(2I-1)$), η , and the orientation of the principal axes. By measuring $2\Delta v$ at enough different orientations and using the transformation Eq. (2.4.13), the desired quantities can be worked out. Equation (2.4.13) is not very convenient, however, as the a_{13} , a_{23} , a_{33} terms are different for each orientation. We therefore pick a crystal frame X, Y, Z which is known and may contain some of the crystal axes. The transformation from the lab x' , y' , z' frame to the X, Y, Z frame is known, and the transformation from the X, Y, Z frame to the x , y , z principal axis frame will be constant as both frames are fixed in the crystal.

The procedure is to find the EFG tensor in the crystal frame by experimental methods, then diagonalize the tensor. Diagonalization will yield the EFG tensor in the principal axis frame as well as its orientation with respect to the crystal axes. Volkoff, Petch and Smellie [9] outlined the procedure in 1952 and it has become a rather standard method since then. The Volkoff method more recently was shown to have possible ambiguities [10]. Furthermore it requires more data than is necessary in many cases as discovered in the present work (discussed in Chap. 4) and as recently reported by El Saffar [11]. Nevertheless, the Volkoff method provides a very convenient starting point and it is easy to modify it to reduce the quantity of data required.

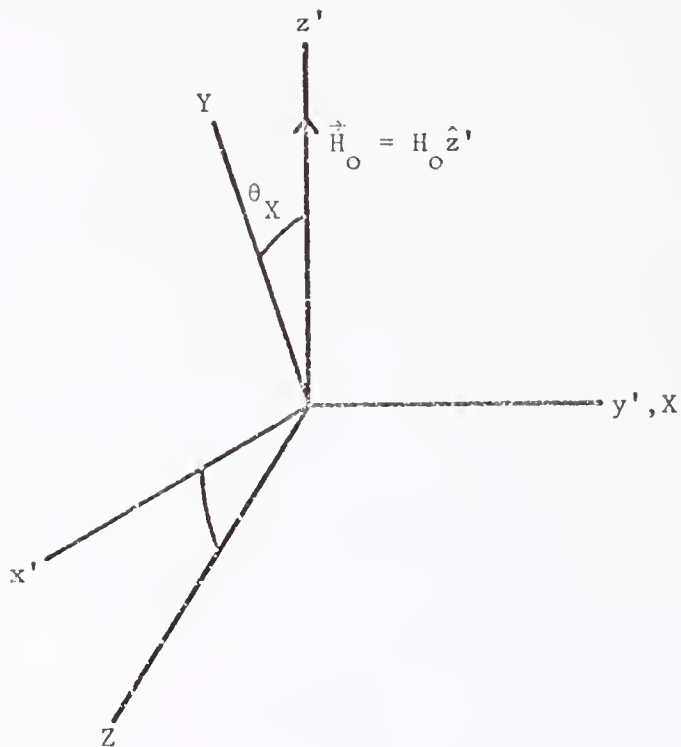
The tensor

$$\begin{pmatrix} \phi_{XX} & \phi_{XY} & \phi_{XZ} \\ \phi_{XY} & \phi_{YY} & \phi_{YZ} \\ \phi_{XZ} & \phi_{YZ} & \phi_{ZZ} \end{pmatrix} \quad (2.4.15)$$

is symmetric as displayed and has only 5 independent elements using the vanishing trace property. Diagonalization gives

$$\begin{pmatrix} \phi_{xx} & 0 & 0 \\ 0 & \phi_{yy} & 0 \\ 0 & 0 & \phi_{zz} \end{pmatrix} = \begin{pmatrix} -eq(1-\eta)/2 & 0 & 0 \\ 0 & -eq(1+\eta)/2 & 0 \\ 0 & 0 & eq \end{pmatrix} \quad (2.4.16)$$

and the direction cosines of the principal axes. We recall the



$$\begin{aligned} X &= y' \\ Y &= z' \cos \theta_X + x' \sin \theta_X \\ Z &= -z' \sin \theta_X + x' \cos \theta_X \end{aligned}$$

Figure 3. Transformation between the lab axes and crystal axes during an X rotation. Cyclic permutations of X, Y, Z result in the transformations for Z and Y rotations.

elements all contain the factor $K = 3eQ(2m - 1)/2I(2I - 1)h$ so only e^2qQ is actually determined, rather than eq and eQ .

We start experimentally by selecting crystal axes X, Y, Z and aligning the crystal in a magnetic field $\vec{H}_c = \hat{z}'H_0$ with X, Y, Z parallel to y' , z' , x' initially. The crystal is then rotated about the X = y' axis through an angle θ_X and the frequency separation $2\Delta\nu_X$ observed and plotted versus θ_X , the plot being termed the X rotation pattern. Figure 3 shows the relation between the crystal and lab frames for an X rotation.

Using the transformation equations in Fig. 3, we obtain

$$\begin{aligned} \phi_{z'z'} &= \frac{\partial^2}{\partial z' \partial z'} \phi = \left(\cos\theta_X \frac{\partial}{\partial Y} - \sin\theta_X \frac{\partial}{\partial Z} \right)^2 \phi \\ &= \frac{1}{2}(\phi_{YY} + \phi_{ZZ}) + \frac{1}{2}(\phi_{YY} - \phi_{ZZ})\cos 2\theta_X - \phi_{YZ}\sin 2\theta_X \end{aligned} \quad (2.4.17)$$

which is put in Eq. (2.4.14), yielding

$$\begin{aligned} 2\Delta\nu_X &= A_X + B_X\cos 2\theta_X + C_X\sin 2\theta_X \\ &= A_X + (B_X^2 + C_X^2)^{\frac{1}{2}}\cos 2(\theta_X - \delta_X) \end{aligned} \quad (2.4.18)$$

where

$$A_X = \frac{1}{2}K(\phi_{YY} + \phi_{ZZ}) = -\frac{1}{2}K\phi_{XX}$$

$$B_X = \frac{1}{2}K(\phi_{YY} - \phi_{ZZ})$$

$$C_X = -K\phi_{YZ}$$

$$\tan 2\delta_X = \frac{C_X}{B_X} \quad . \quad (2.4.19)$$

Thus the X rotation yields the diagonal elements and ϕ_{YZ} . Similar equations may be obtained by cyclic permutation, so ϕ_{XZ} and ϕ_{XY} may be obtained from Y and Z rotations, respectively.

Diagonalization of the EFG tensor requires solving the cubic equation

$$\gamma^3 - a\gamma - b = 0 \quad , \quad (2.4.20)$$

where

$$a = K^2(\phi_{XY}^2 + \phi_{YZ}^2 + \phi_{XZ}^2 - \phi_{XX}\phi_{YY} - \phi_{YY}\phi_{ZZ} - \phi_{ZZ}\phi_{XX})$$

$$b = K^3(\phi_{XX}\phi_{YY}\phi_{ZZ} + 2\phi_{XY}\phi_{YZ}\phi_{XZ} - \phi_{XY}^2\phi_{YZ} - \phi_{YY}^2\phi_{XZ} - \phi_{ZZ}^2\phi_{XY}) \quad . \quad (2.4.21)$$

We find

$$\gamma_n = 2(a/3)^{1/2} \cos(\alpha - 2\pi n/3), \quad n = 1, 2, 3 \quad (2.4.22)$$

$$\cos 3\alpha = (|b|/2)(3/a)^{3/2} \quad 0 \leq \alpha \leq \pi/6$$

$$\gamma_1 = K\phi_{xx}, \quad \gamma_2 = K\phi_{yy}, \quad \gamma_3 = K\phi_{zz} \quad .$$

These choices insure

$$\gamma_3 = |\gamma_3|, \quad |\gamma_3| \geq |\gamma_2| \geq |\gamma_1|, \quad (2.4.23)$$

and finally we obtain

$$\eta = (\gamma_1 - \gamma_2)/\gamma_3 = 3^{1/2} \tan \alpha \quad (2.4.24)$$

and

$$|e^2 q Q / h| = |e Q \phi_{zz} / h| = [2I(2I - 1) / 3(2n - 1)] \cdot |K \phi_{zz}| \quad (2.4.25)$$

The diagonalization process yields the direction cosines of the x, y, z principal axes with respect to the X, Y, Z crystal axes:

$$\frac{\lambda_n}{D_{1n}} = \frac{\mu_n}{D_{2n}} = \frac{\nu_n}{D_{3n}} = \frac{\pm 1}{(D_{1n}^2 + D_{2n}^2 + D_{3n}^2)^{1/2}} \quad (2.4.26)$$

where λ_1, μ_1, ν_1 are the direction cosines of x with respect to X, Y, Z and likewise for $n = 2$ and 3 .

The relative signs of λ_n, μ_n, ν_n for any n are fixed, but all three signs may be reversed without reversing the signs for the other values of n . Thus, a right- or left-handed coordinate system may be chosen.

Volkoff notes that only five readings are required in the most general case, such as $\theta_X = \theta_Y = \theta_Z = 45^\circ$ and any two of $\theta_X = \theta_Y = \theta_Z = 0^\circ$. This would require a very accurate knowledge of the

orientations and in the case of inequivalent sites, identification of the transitions might be difficult.

Additional data increase accuracy and may be helpful in detecting orientation errors and in identifying the transitions. Some of these effects as well as the single rotation method will be discussed in Chap. 4.

2.5 Intramolecular Dipolar Splitting of the NMR Spectrum of ^{15}N in ^{15}N - ^{14}N Mixed Molecules

We next consider the case of ^{15}N - ^{14}N mixed molecules with nuclear spins $I = \frac{1}{2}$ and $I = 1$ for the two isotopes, respectively. The total Hamiltonian is taken as

$$\mathcal{H} = \mathcal{H}_Z(15) + \mathcal{H}_Z(14) + \mathcal{H}_Q(14) + \mathcal{H}_D(15-14) \quad . \quad (2.5.1)$$

The region where the ^{15}N Zeeman and ^{14}N quadrupolar energies are of the same order will be considered. The ^{15}N - ^{14}N intramolecular dipolar energy is much less and may be treated by first-order perturbation theory. We note at this point that the asymmetry parameter η is zero for N_2 .

We proceed in the following manner. The $\mathcal{H}_Q(14)$ term in zero field gives rise to two energy levels corresponding to $m = 0$ and $m = \pm 1$ with state functions $|1\rangle$, $|0\rangle$, $|-1\rangle$. Adding an external magnetic field \vec{H}_0 removes the degeneracy and the state functions become linear combinations of $|1\rangle$, $|0\rangle$, $|-1\rangle$:

$$|\psi_n\rangle = \alpha_{1n}|1\rangle + \alpha_{2n}|0\rangle + \alpha_{3n}|-1\rangle \quad . \quad (2.5.2)$$

Working in the principal axes (PA) frame, we calculate the α_{mn} 's using $\mathcal{H}_Q(14)$ and $\mathcal{H}_Z(14)$. Next, $\mathcal{H}_Z(15)$ (with state functions $|+\frac{1}{2}\rangle$, $|-\frac{1}{2}\rangle$ in a frame where $\vec{H}_0 = \hat{z}H_0$) is expressed in the PA frame, and the state functions are linear combinations of $|+\frac{1}{2}\rangle$, $|-\frac{1}{2}\rangle$:

$$|\zeta_{\pm}\rangle = \beta_{1\pm}|+\frac{1}{2}\rangle + \beta_{2\pm}|-\frac{1}{2}\rangle \quad . \quad (2.5.3)$$

To first order, the total state functions are taken as products of the exact uncoupled state functions,

$$|\xi_{n\pm}\rangle = |\psi_n\rangle |\zeta_{\pm}\rangle \quad . \quad (2.5.4)$$

$\mathcal{H}_D(15-14)$ is treated as a perturbation causing a first-order shift which is dependent on the state of the $^{14}_N$ nuclei.

From Eqs. (2.3.21) and (2.1.2) we have

$$\begin{aligned} \mathcal{H}_{Q,Z}(14) &= \mathcal{H}_Q(14) + \mathcal{H}_Z(14) \\ &= A(3I_z^2 - I^2) - \gamma\hbar\vec{I}\cdot\vec{H}_0 \end{aligned} \quad (2.5.5)$$

where x, y, z is the PA frame.

As the molecule is axially symmetric (and therefore $\eta = 0$), we may arbitrarily select the orientation of x and y and therefore choose x in the plane of H_0 and z. Thus, $\vec{H}_0 = \hat{z}H_0 \cos\theta + \hat{x}H_0 \sin\theta$ where θ is the angle between \vec{H}_0 and \hat{z} , and

$$\begin{aligned} \mathcal{H}_{Q,Z}^{(14)} &= A(3I_Z^2 - \vec{I}^2) - \gamma\hbar(I_Z H_0 \cos\theta + I_X H_0 \sin\theta) \\ &= A(3I_Z^2 - \vec{I}^2) - \gamma\hbar I_Z H_0 \cos\theta - \frac{\gamma\hbar H_0 \sin\theta}{2} (I_+ + I_-). \end{aligned} \quad (2.5.6)$$

Introducing

$$L = \frac{2\gamma\hbar H_0}{e^2 q Q}, \quad T = \frac{E}{2A}, \quad u = \cos\theta, \quad v = \frac{\sin\theta}{\sqrt{2}} \quad (2.5.7)$$

we obtain

$$\mathcal{H}_{Q,Z}^{(14)} = 2A \left[(3I_Z^2 - \vec{I}^2)/2 - LuI_Z - Lv(I_+ + I_-)/\sqrt{2} \right]. \quad (2.5.8)$$

Matrix elements are calculated and displayed in matrix form

$$= 2A \begin{pmatrix} \frac{1}{2} - Lu & -Lv & 0 \\ -Lv & -1 & -Lv \\ 0 & -Lv & \frac{1}{2} + Lu \end{pmatrix}. \quad (2.5.9)$$

The secular determinant

$$|\mathcal{H} - E\mathbb{1}| = 0 \quad (2.5.10)$$

results in the cubic equation

$$T^3 - T(3/4 + L^2) + 1/4 - (1/2)L^2(3u^2 - 1) = 0, \quad (2.5.11)$$

where we have used $T = E/2A$ from (2.5.7). The solutions of a cubic equation

$$T^3 - a_1 T - a_0 = 0 \quad (2.5.12)$$

are

$$T_{-1} = 2(a_1/3)^{1/2} \cos(\phi/3)$$

$$T_0 = 2(a_1/3)^{1/2} \cos(\phi/3 + 120^\circ)$$

$$T_1 = 2(a_1/3)^{1/2} \cos(\phi/3 + 240^\circ) \quad (2.5.13)$$

where $\cos\phi = (a_0/2)(a_1/3)^{-3/2}$. Parker [12] has tabulated T_n 's for various angles, external fields, and spins.

The assignment of subscripts to the reduced energies T_n is made by examining the behavior of T_n in the limit of small H_0 where $-1, 0, 1$ are good quantum numbers. In the region of interest, linear combinations must be used as expressed in Eq. (2.5.2) which can be written as a column vector,

$$|\psi_n\rangle = \begin{pmatrix} \alpha_{1n} \\ \alpha_{0n} \\ \alpha_{-1n} \end{pmatrix} \quad (2.5.14)$$

In our notation, $\mathcal{H}|\psi_n\rangle = E_n|\psi_n\rangle$ becomes

$$\begin{pmatrix} \frac{1}{2} - Lu & -Lv & 0 \\ -Lv & -1 & -Lv \\ 0 & -Lv & \frac{1}{2} + Lu \end{pmatrix} \begin{pmatrix} \alpha_{1n} \\ \alpha_{0n} \\ \alpha_{-1n} \end{pmatrix} = Tn \begin{pmatrix} \alpha_{1n} \\ \alpha_{0n} \\ \alpha_{-1n} \end{pmatrix}, \quad (2.5.15)$$

which can be solved for α_{mn} 's using $\alpha_{1n}^2 + \alpha_{0n}^2 + \alpha_{-1n}^2 = 1$.

Introducing

$$C_{1n} = (\frac{1}{2} - Tn - Lu), \quad C_{0n} = Lv, \quad C_{-1n} = (\frac{1}{2} - Tn + Lu),$$

$$C_n = (C_{1n}^2 C_{0n}^2 + C_{1n}^2 C_{-1n}^2 + C_{-1n}^2 C_{0n}^2)^{\frac{1}{2}} \quad (2.5.16)$$

the solutions are

$$\alpha_{1n} = C_{0n} C_{-1n} / C_n, \quad \alpha_{0n} = C_{-1n} C_{1n} / C_n, \quad \alpha_{-1n} = C_{0n} C_{1n} / C_n. \quad (2.5.17)$$

The complexity of these rather simple appearing equations can only be appreciated by expressing them in terms of H_0 , $e^2 q Q$, and θ ; however, the substitutions in (2.5.7) and (2.5.16) greatly simplify the calculations.

Up to this point only ^{14}N has been considered. From here on we must add a 14 or 15 label to avoid confusion. The Zeeman Hamiltonian $\mathcal{H}_Z(15)$ expressed in the PA frame has a form similar to $\mathcal{H}_Z(14)$ in Eq. (2.5.6):

$$\mathcal{H}_Z(15) = -\gamma(15)\hbar H_0 \cos\theta I_Z(15) - \frac{\gamma(15)\hbar H_0 \sin\theta}{2} (I_+(15) + I_-(15)). \quad (2.5.18)$$

In the frame with H_0 parallel to the z axis, the exact states are $|+\frac{1}{2}\rangle$, $|-\frac{1}{2}\rangle$, but here H_0 forms an angle θ with the z axis and linear combinations of the exact state functions must be used:

$$\begin{aligned} |\zeta_{\pm}\rangle &= \beta_{1\pm} |+\frac{1}{2}\rangle + \beta_{2\pm} |-\frac{1}{2}\rangle \\ &= \begin{pmatrix} \beta_{1\pm} \\ \beta_{2\pm} \end{pmatrix} \end{aligned} \quad (2.5.19)$$

in column vector form.

Letting $B = (\frac{1}{2})\gamma(15)\hbar H_0 \cos\theta$, $C = (\frac{1}{2})\gamma(15)\hbar H_0 \sin\theta$, Eq. (2.5.18) becomes

$$\begin{aligned} \mathcal{H}'_Z(15) &= -2BI_Z(15) - C[I_+(15) + I_-(15)] \\ &= \begin{pmatrix} -B & -C \\ -C & C \end{pmatrix} \end{aligned} \quad (2.5.20)$$

in matrix form, and

$$\begin{pmatrix} -B & -C \\ -C & C \end{pmatrix} \begin{pmatrix} \beta_{1\pm} \\ \beta_{2\pm} \end{pmatrix} = \mp\gamma(15)\hbar H_0 \begin{pmatrix} \beta_{1\pm} \\ \beta_{2\pm} \end{pmatrix} \quad (2.5.21)$$

This equation together with the normalization condition, $\beta_{1\pm}^2 + \beta_{2\pm}^2 = 1$, can be used to obtain

$$\begin{aligned} \beta_{1+} &= \cos\frac{\theta}{2}, & \beta_{2+} &= \sin\frac{\theta}{2} \\ \beta_{1-} &= -\sin\frac{\theta}{2}, & \beta_{2-} &= \cos\frac{\theta}{2} \end{aligned} \quad (2.5.22)$$

or

$$|\zeta_+\rangle = \begin{pmatrix} \cos\frac{\theta}{2} \\ \sin\frac{\theta}{2} \end{pmatrix}, \quad |\zeta_-\rangle = \begin{pmatrix} -\sin\frac{\theta}{2} \\ \cos\frac{\theta}{2} \end{pmatrix}. \quad (2.5.23)$$

We can now form the product functions $|\xi_{n\pm}\rangle$ Eq. (2.5.4).

We next consider the perturbation term,

$$\mathcal{H}_D(15-14) = \frac{\gamma(15)\gamma(14)\hbar^2}{r^3} \left[\vec{I}(15) \cdot \vec{I}(14) - 3 \frac{(\vec{I}(15) \cdot \vec{r})(\vec{I}(14) \cdot \vec{r})}{r^2} \right] \quad (2.5.24)$$

which comes from Eq. (2.2.5). In the PA frame, $\vec{r}/r = \hat{z}$, so

$$\mathcal{H}_D(15-14) = D \left\{ (1/2) [I_+(15)I_-(14) + I_-(15)I_+(14)] - 2I_z(15)I_z(14) \right\} \quad (2.5.25)$$

where $D = \gamma(15)\gamma(14)\hbar^2/r^3$. We recognize the B and A terms, respectively, of Eqs. (2.2.8) with $\theta = 0$, and note all the other terms vanish due to a $\sin\theta$ factor. We recall the angle θ in Sec. 2.3 was between \vec{r} and the z axis which is taken to be zero here.

We are interested only in the first-order energy shifts due to $\mathcal{H}_D(15-14)$, given by the diagonal matrix elements $\langle \xi_{n\pm} | \mathcal{H}_D(15-14) | \xi_{n\pm} \rangle$.

Expressing Eq. (2.5.20) in matrix form,

$$\mathcal{H}_D(15-14) = D \left[\frac{1}{\sqrt{2}} \begin{pmatrix} 0 & 1 & 0 \\ 0 & 0 & 1 \\ 0 & 0 & 0 \end{pmatrix} \begin{pmatrix} 0 & 0 \\ 1 & 0 \end{pmatrix} + \frac{1}{\sqrt{2}} \begin{pmatrix} 0 & 0 & 0 \\ 1 & 0 & 0 \\ 0 & 1 & 0 \end{pmatrix} \begin{pmatrix} 0 & 1 \\ 0 & 0 \end{pmatrix} - \begin{pmatrix} 1 & 0 & 0 \\ 0 & 0 & 0 \\ 0 & 0 & -1 \end{pmatrix} \begin{pmatrix} 1 & 0 \\ 0 & -1 \end{pmatrix} \right]. \quad (2.5.26)$$

Diagonal elements can be calculated

$$\begin{pmatrix} \alpha_{1n}, \alpha_{0n}, \alpha_{-1n} \end{pmatrix} \begin{pmatrix} 0 & 1 & 0 \\ 0 & 0 & 1 \\ 0 & 0 & 0 \end{pmatrix} \begin{pmatrix} \alpha_{1n} \\ \alpha_{0n} \\ \alpha_{-1n} \end{pmatrix} (\beta_{1\pm} \beta_{2\pm}) \begin{pmatrix} 0 & 0 \\ 1 & 0 \end{pmatrix} \begin{pmatrix} \beta_{1\pm} \\ \beta_{2\pm} \end{pmatrix} \\ = (\alpha_{1n} \alpha_{0n} + \alpha_{0n} \alpha_{-1n}) (\beta_{1\pm} \beta_{2\pm}) \quad (2.5.27)$$

and so on for the other terms. The result is

$$\Delta E_{n\pm} = D \left[\sqrt{2} (\alpha_{0n} \alpha_{1n} + \alpha_{0n} \alpha_{-1n}) (\beta_{1\pm} \beta_{2\pm}) - (\alpha_{1n}^2 - \alpha_{-1n}^2) (\beta_{1\pm}^2 - \beta_{2\pm}^2) \right] \\ = \pm D \left[(\alpha_{0n} \alpha_{1n} + \alpha_{0n} \alpha_{-1n}) \frac{\sin \theta}{\sqrt{2}} - (\alpha_{1n}^2 - \alpha_{-1n}^2) \cos \theta \right] \\ = -\Delta E_{n\mp} \quad (2.5.28)$$

The $^{15}\text{N} \ +\frac{1}{2} \rightarrow -\frac{1}{2}$ transition will occur, to zero order, at $\hbar\omega_c = \gamma \hbar H_0$ which is of no interest and will be shifted by $\Delta E_{n+} - \Delta E_{n-} = 2\Delta E_{n+}$. We therefore calculate only

$$2\Delta E_{n+} = D \left[\sqrt{2} (\alpha_{0n} \alpha_{1n} + \alpha_{0n} \alpha_{-1n}) \sin \theta - 2(\alpha_{1n}^2 - \alpha_{-1n}^2) \cos \theta \right]. \quad (2.5.29)$$

It is useful to examine the θ dependence of $2\Delta E_{n+}$. We note from Eqs. (2.5.11) and (2.5.12) that a_0 and a_1 have the same value at θ and $180 - \theta$, and thus ϕ and subsequently T_{-1} , T_0 , T_1 also have the same value. Therefore, from Eqs. (2.5.16), $C_{1n}(\theta) = C_{-1n}(180 - \theta)$, $C_{0n}(\theta) = C_{0n}(180 - \theta)$ and $C_n(\theta) = C_n(180 - \theta)$. Using these equations, we find from Eqs. (2.5.17) that $\alpha_{1n}(\theta) = \alpha_{-1n}(180 - \theta)$ and $\alpha_{0n}(\theta) = \alpha_{0n}(180 - \theta)$. We now inspect Eq. (2.5.29) and note $(\alpha_{0n}\alpha_{1n} + \alpha_{0n}\alpha_{-1n})$ and $\sin\theta$ have the same value at θ as at $180 - \theta$, while both $(\alpha_{1n}^2 - \alpha_{-1n}^2)$ and $\cos\theta$ reverse signs, so the product does not change value or sign. Thus $2\Delta E_{n+}$ needs to be calculated for the first quadrant only, as it merely repeats the same values in the second quadrant.

As the sample was polycrystalline, we again must work out the powder pattern spectrum. In Sec. 2.2 it was shown that any value of $\cos\theta$ was equally probable so the unbroadened spectrum was the 'density' of $u(= \cos\theta)$ versus h , the dipole contribution to the field, or du/dh . It was easy to express u in terms of h , and thereby obtain an analytic expression.

In principle the same procedure would work here, but it is not possible to express u in terms of v (equivalent to h in Sec. 2.2). It is possible in both cases, however, to numerically calculate v (or h) for various θ 's and weigh the results by a factor depending on the probability of each θ occurring.

We center a sphere on the origin and note that a given θ_i and $\Delta\theta$ define an annular area on the surface of the sphere given by

$$\begin{aligned} \Delta A_i &= (\text{length})(\text{width}) = (2\pi r \sin\theta_i)(r\Delta\theta) \\ &= (\text{constant}) \sin\theta_i \end{aligned} \tag{2.5.30}$$

in the limit of small $\Delta\theta$. The intensity of the signal at frequency ν_i due to molecules with orientation θ_i is proportional to the number of molecules with that orientation, or $\sin\theta_i$. We therefore plot $\sin\theta_i$ versus ν_{θ_i} to obtain the unbroadened spectrum, or convolute with a Gaussian function to obtain the intermolecular broadened function.

A computer is used to perform the calculations, taking values of θ_i between 0° and 90° with a sufficiently small $\Delta\theta$ to adequately represent the smooth curve.

2.6 Nuclear Spin-Lattice Relaxation

2.6.1 General

The resonant condition is detected by noting the energy absorbed in driving nuclear spins to a higher energy state or by noting the energy given off when they return to a lower energy state. The radio frequency field H_1 , discussed in Sec. 2.1, is equally likely to induce transitions either way which would result in zero net energy exchange if there were the same number of spins in the two states involved.

In practice, the population of the lower energy state is slightly favored according to the Boltzmann distribution if the system is in thermal equilibrium. Therefore, a resonant rf signal will give up a net amount of energy to the system as long as there are more spins in the lower energy state.

It can be seen that the rf signal will tend to destroy the population difference by inducing transitions from the more highly populated state at a faster rate. The experimental fact that the system returns to the equilibrium distribution, perhaps at a rate fast enough to overcome the tendency of the rf signal to destroy the equilibrium condition,

is evidence that there must be some other mechanism which couples with the spins.

We find there are several mechanisms by which the spin system can give up energy to the lattice and thereby return to equilibrium. The rate at which this occurs is termed the relaxation rate and its reciprocal is the spin-lattice relaxation time T_1 .

Taking the simple condition of a spin system in a magnetic field \vec{H}_0 where \vec{H}_0 is parallel to the z axis, we see the population difference results in a net magnetization M_z parallel to \vec{H}_0 which has some equilibrium value M_0 . The magnetization M_z approaches M_0 at a rate proportional to the difference $M_0 - M_z$, resulting in the exponential equation

$$M_z(t) = M_0(1 - e^{-t/T_1}) \quad , \quad (2.6.1)$$

where t is measured from the time at which the spin order was completely destroyed ($M_z(0) = 0$).

The spin system exchanges energy with the lattice in several ways. For instance, in Sec. 2.2 it was noted that the magnetic moment of one nucleus produces a magnetic field at the sites of neighboring nuclei. If the nucleus is undergoing some type of motion within the lattice, it will produce a changing magnetic field at other sites. We might imagine this varying field as a sum of its Fourier components. If some of the components are of the appropriate frequency, they can induce transitions in neighboring spins, allowing the nonequilibrium spin system to return to equilibrium. This relaxation towards equilibrium through a coupling of the spins with the lattice through the field produced by nearby nuclear dipoles is appropriately called dipolar relaxation.

A nucleus having a nuclear quadrupole moment in an electric field

gradient which is time dependent due to motion within the lattice experiences nuclear quadrupole relaxation. Considering the magnetic moment of a molecule as a whole, a time-dependent field is produced at the nuclear sites within the molecule itself due to the rotational motion of the molecule which produces spin-rotational relaxation.

There are many other relaxation processes which are of no interest to the present experiment. It might be that several processes simultaneously contribute to the relaxation and the observed relaxation rate is the sum of the rates due to individual processes,

$$1/T_1 = 1/T_{1D} + 1/T_{1Q} + 1/T_{1sr} + \dots \quad , \quad (2.6.2)$$

where T_{1D} , T_{1Q} , T_{1sr} are the dipolar, quadrupolar, and spin-rotation relaxation times, respectively. It may be relatively difficult in such a case to determine the relaxation times individually.

The molecular motion responsible for producing the fluctuating electric or magnetic fields at the site of a nucleus must have frequency components in the spectral density at resonance and must be significant enough to induce transitions. In the case of dipolar and quadrupolar relaxation, a reorientation on the order of one radian at the appropriate rate is required, whereas spin-rotation relaxation involves only a change in angular momentum. In order to relate this molecular motion to the temperature of the sample, we use a quantity called the correlation time which is something like the time required by the molecule to undergo the appropriate change in orientation or angular momentum. The quadrupolar correlation time τ_Q is given [13] by the integral of the autocorrelation function of $P_2(\cos\theta)$ where θ specifies the orientation of the molecule, and the spin-rotational correlation time τ_{sr} is given [13] by the integral of the time autocorrelation function of molecular

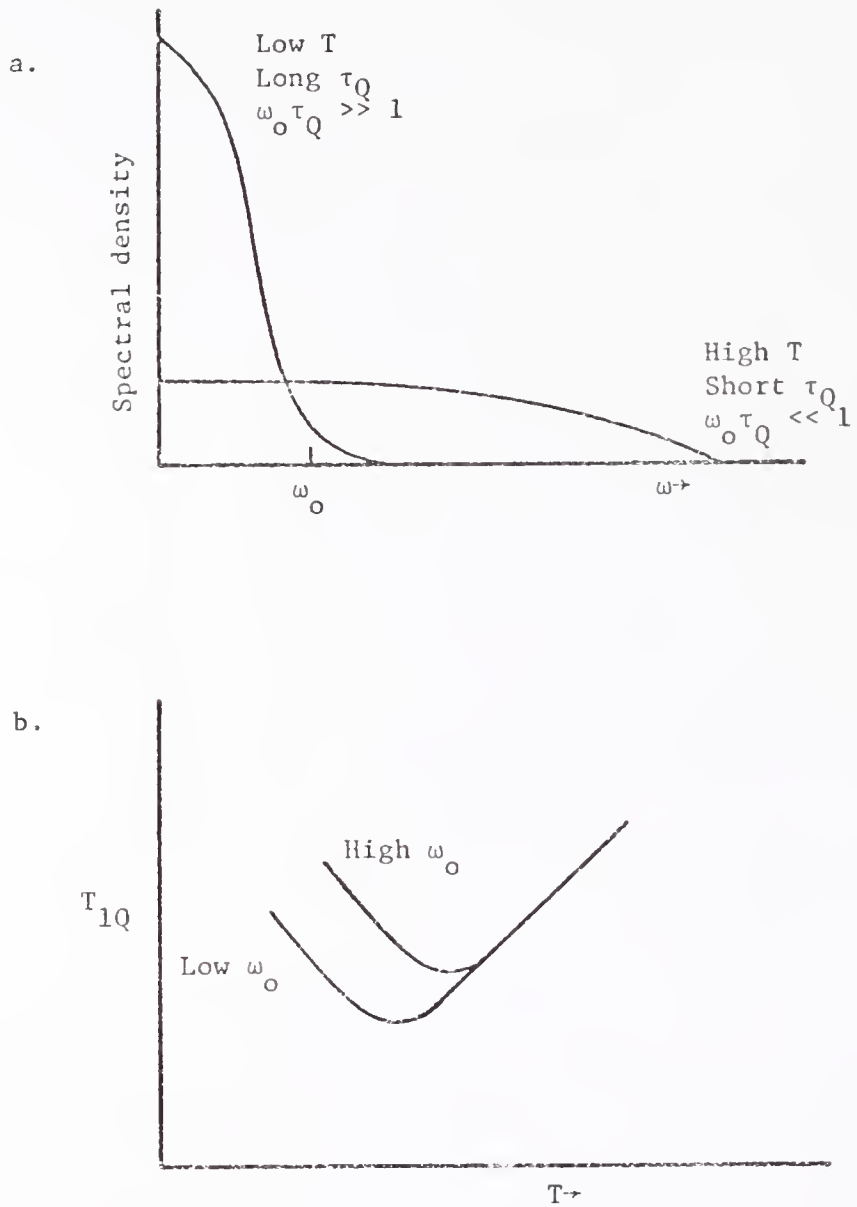


Figure 4. Temperature dependence of quadrupolar relaxation time. (a) Spectral density of correlation time versus frequency. (b) Qualitative dependence of T_{1Q} versus temperature. Frequency independence of T_{1Q} at high temperature is a result of the flatness of the high temperature curve in the upper figure

angular momentum.

As a sample cools, collisions are more frequent due to increased density. A molecule therefore requires more time to change orientation through a large angle as the random collisions cancel each other out to a greater extent. The correlation time τ_Q therefore increases with decreasing temperature. On the other hand, a single collision can even completely reverse the angular momentum of a molecule, and therefore, increasing the frequency of collisions reduces the spin-rotational correlation time τ_{sr} .

The reciprocal of the correlation time is something like the frequency of the changing electric or magnetic field. If this frequency is very high so $\omega_0 \tau \ll 1$ where ω_0 is the Larmor frequency of the nucleus, there will be frequency components over a very wide range, resulting in only a small proportion near ω_0 . The mechanism will be fairly ineffective under these conditions. On the other hand, if the correlation time is very long, it corresponds to a very low frequency, and $\omega_0 \tau \gg 1$. Most of the frequency components will be very low, and again the mechanism will be fairly ineffective. Between the two extremes, where $\omega_0 \tau \approx 1$, the frequency is on the order of the Larmor frequency and the relaxation mechanism attains maximum effectiveness and T_1 is a minimum.

Figure 4 illustrates the case of quadrupolar relaxation. Figure 4(a) shows the spectral density of the changing electric field gradient at both high and low temperatures. A maximum at ω_0 would occur at some intermediate temperature. We note that if ω_0 is changed by changing the external field, for instance, there will be little effect in the high temperature region, but in the low temperature region, reducing ω_0 will increase the effectiveness and shorten T_1 .

Converted to T_1 dependence on temperature, the plot would be something like Fig. 4(b).

2.6.2 The Hubbard Relation

We now restrict the discussion to the high temperature range where $\omega_c \tau_Q \ll 1$ and where T_{1Q} is independent of frequency ω_c . In this region the spin-rotational component of the relaxation time is given by [14]

$$T_{1sr}^{-1} = (4/3)(I_o kT/\hbar^2)(2\pi C)^2 \tau_{sr} \quad (2.6.3)$$

where I_o is the molecular moment of inertia, T is the temperature, and C is the spin-rotational constant.

The quadrupolar relaxation time is given by [4]

$$T_{1Q}^{-1} = (3/8)(e^2 qQ/\hbar)^2 \tau_Q \quad (2.6.4)$$

We now look at the relation between τ_{sr} and τ_Q . If τ_{sr} is long enough to allow the molecule to undergo large angle reorientation between collisions, we have $\tau_Q \leq \tau_{sr}$. Furthermore, changing τ_{sr} does not directly have much effect on τ_Q . On the other hand, we may increase the frequency of collisions and thereby reduce τ_{sr} to the point where many random collisions are required before the molecule reorients through a large angle. In this region $\tau_Q \gg \tau_{sr}$ and a change in τ_{sr} will be accompanied by an opposite change in τ_Q . This complementary effect has been shown to obey the condition

$$\tau_Q \tau_{sr} = I_o / 6kT \quad (2.6.5)$$

by Hubbard [14] using a rotational diffusion model. The Hubbard relation can be written

$$\tau_Q^* \tau_{sr}^* = 1/6 \quad (2.6.6)$$

where reduced correlation times are defined by $\tau^* = \tau(kT/I_0)^{1/2}$. The reduced correlation times are the correlation times expressed in units of time required for a classical freely rotating spherical molecule to rotate through one radian. The Hubbard relation was based on spherical molecules; however Kluk and Powles [15] have shown it holds for linear molecules as well.

CHAPTER III
EXPERIMENTAL EQUIPMENT AND PROCEDURE

3.1 Superconductive Magnet System

3.1.1 Magnet

The heart of the system is an RCA Superconductive Magnet Type SM-2841 capable of producing a maximum field strength of 100 kG at a current level of 91 A. The solenoid itself is about 7 in. long and 7 in. in diameter with a bore of just over two inches and is wound of Nb_3Sn superconductive ribbon. Overall dimensions, including the form (housing), but excluding mounting studs, are 10 in. long, 7.2 in. outside diameter, and a 2.03 in. bore.

The magnet is equipped with a magneto-resistive probe for field strength measurement, which also turns out to be useful as a thermometer during cool-down. With 50 mA dc through the magneto-resistive probe the voltage varied from about 700 mV at room temperature to 84 mV at liquid nitrogen temperature and 2.84 mV at liquid helium temperature at zero field. Thus it was easy to determine when the magnet had reached liquid nitrogen temperature during precooling and when liquid helium began collecting during helium transfer.

At liquid helium temperature, again with 50 mA dc, the voltage across the magneto-resistive probe varied from 2.84 mV at zero field to about 20 mV at 100 kG. Once calibrated, it was accurate to better than ± 20 G.

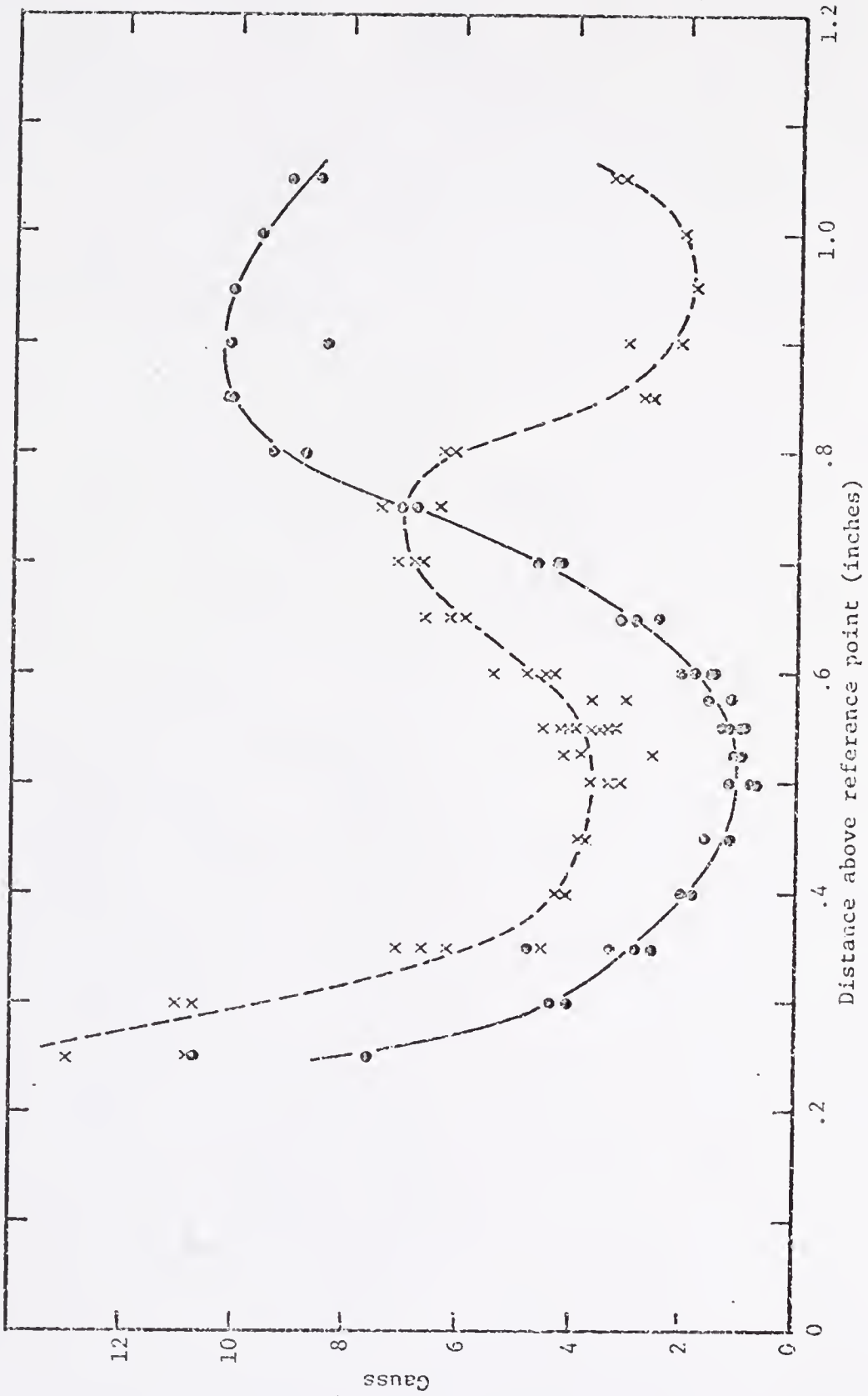


Figure 5. Homogeneity of the superconductive magnet. Solid circles are magnetic field values relative to an arbitrary reference of about 89 kG. Line width data are shown by x's.

The magnet is equipped with a superconductive switch across the terminals for semipersistent operation. A 300-mA current through a resistance wire in the switch keeps the switch in its normal state. Shutting off the heater current allows the switch to cool and become superconductive. The superconductive path is then complete except for the resistance of the copper current terminals and contact resistance where the ends of the coil and the ends of the switch are soldered to the current terminals.

On one occasion the switch heater wire was accidentally burned out, making it impossible to charge the solenoid, so the epoxy-potted switch had to be disassembled and repaired. Unfortunately, this happened before the first resonance was obtained so behavior of the magnet with the original switch as delivered was not determined.

The magnet was advertised to have a homogeneity of 5 G over a 3/4-in. diameter spherical volume (DSV). In order to test the field characteristics and to have a convenient nitrogen reference signal, a liquid ammonia vial was prepared which had inside dimensions of about 7/16 in. long and 3/16 in. diameter. The magnet was mounted with the bore (and hence \vec{H}_0) vertical and the ammonia sample was mounted horizontally.

Variation of the field and line width with position of the sample along the axis of the solenoid are shown in Fig. 5. The abscissa is in inches above an arbitrary reference point on the axis near the center of the solenoid. The ordinates of the line-width data points are in gauss, and were determined by peak-to-peak measurements of the derivative signal obtained by a cw spectrometer. The ordinates of the magnetic field strength H_0 are in gauss above an arbitrary reference of

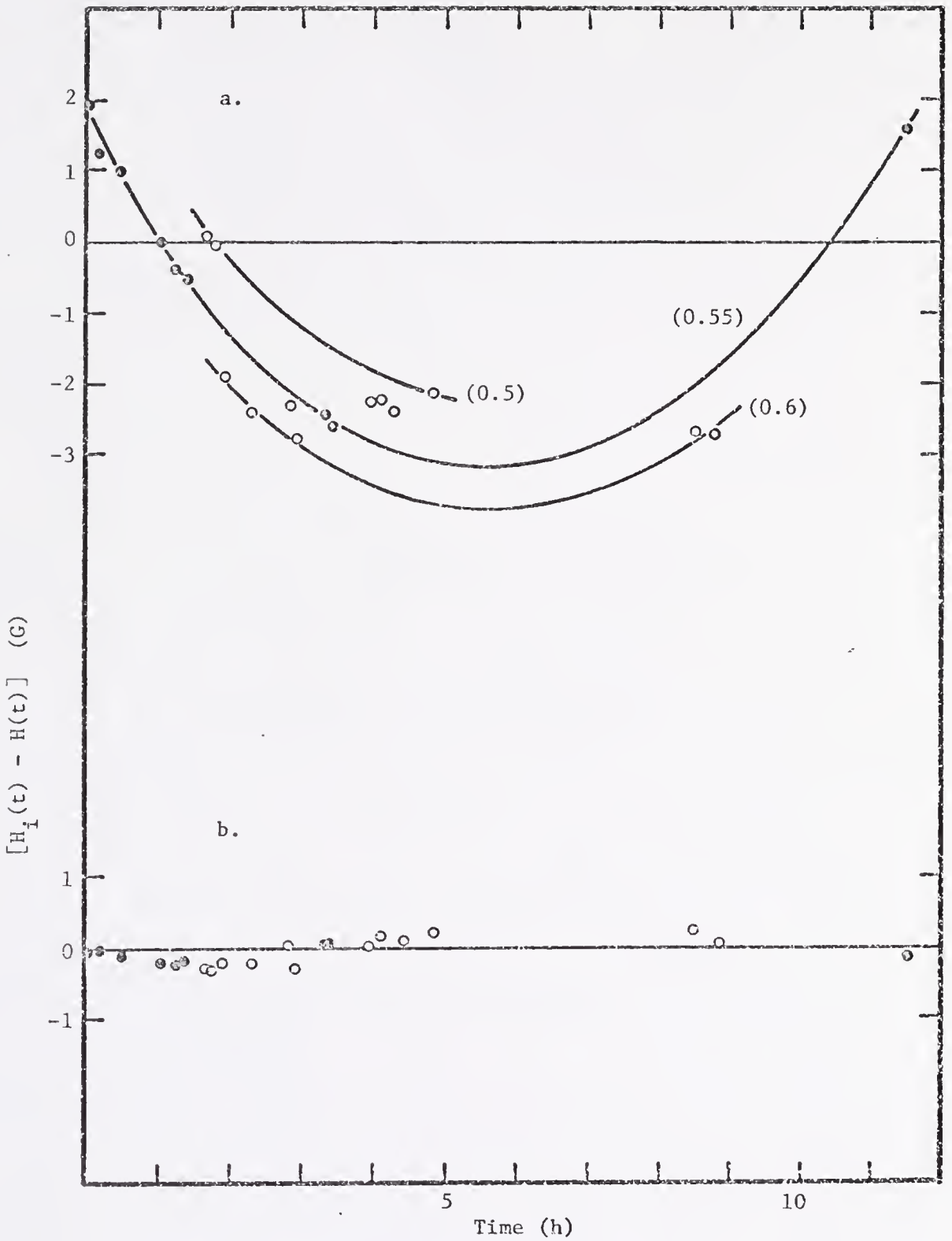


Figure 6. Differences between measured values of magnetic field and value calculated by exponential decay equation. (a) Decay to zero field assumed. Smooth curves are drawn through data points at 0.50, 0.55, and 0.60 inches from Fig. 5. (b) Decay to intermediate value.

about 89 kG, and represent the zero crossover of a sometimes quite wide derivative line.

The data points had to be corrected for a varying field drift rate, the spectrometer frequency sweep rate, direction of sweep, and the spectrometer time constant used.

As the field measurements are an average over the sample volume, they cannot be taken directly as a point-to-point variation along the axis of the bore. Considering the sample size, however, it should be possible to move it about 0.45 in. and still keep it entirely within the 3/4-in. DSV which was advertized to have a homogeneity of 5 G. No such region was found. It appears the homogeneity was closer to 7-9 G over the 3/4-in. DSV.

The peak-to-peak amplitude of the derivative signal was roughly inversely proportional to the line width over most of the region, as expected. However, the maximum amplitude occurred at 0.9 in. on the reference scale and unexpectedly decreased rapidly as the sample was raised until the signal was hardly discernible above 1.05 in.

The 0.9-in. position was chosen for the center of the field as the best combination of linewidth and signal amplitude.

The field typically decayed at a rate of 0.8 to 0.9 G/min. in the semipersistent mode. Values of the field recorded with the sample at the 0.55-in. position were first crudely fitted to the exponential decay equation

$$H(t) = H(0)\exp(-t/\tau) \quad (3.1.1)$$

by a least squares method. Differences between the data points and the values calculated according to Eq. (3.1.1), $H_1(t) - H(t)$, are plotted in Fig. 6(a) as solid circles.

As the value of the field depends on both drift rate and variation of the field with position of the sample, an error in the assumed drift rate causes an erroneous determination of field variation with position. This effect is apparent in Fig. 6(a) where data points at positions other than 0.55 in. are shown as open circles which are offset from a smooth curve through the solid circles.

Clearly Eq. (3.1.1) is not adequate over the 11.5-h duration of the experiment. Hence, the equation

$$H(t) = H(\infty) + [H(0) - H(\infty)]\exp(-t/\tau) \quad (3.1.2)$$

was used. A plot of $H_i(t) - H(t)$ versus time is shown in Fig. 6(b) where it is seen the fit is far better and entirely adequate.

Equation (3.1.1) was

$$H(t) = 89,411 \exp(-t/1755.5) \quad (3.1.3)$$

and Eq. (3.1.2) was

$$H(t) = 81,774 + 7639.1 \exp(-t/144.6) \quad (3.1.4)$$

where t is in hours and H in gauss.

Some variation in the values of $H(\infty)$ and τ occurred on succeeding runs, but generally $H(\infty)$ could be considered constant during any given run. On occasion the drift rate was nearly double the typical 0.8 or 0.9 G/min value. During one run, the drift rate increased with time as though $H(\infty)$ were decreasing.

Maintaining full current in the leads appeared to have no effect on the drift rate, but the magnet was not operated for extended periods with full current in the leads due to increased liquid helium consumption.

In some runs, the field was deliberately increased beyond the

desired value, then decreased. The drift rate was affected only the first few minutes before returning to a behavior similar to that described by Eq. (3.1.2).

It appears that Eq. (3.1.2) is normally quite accurate over operating periods of up to 23 h used thus far. At some time the value of $H(\infty)$ must decrease due to the small resistance in the solenoid circuit, but no long term study of this effect was undertaken.

Several field determinations during each run using the ammonia sample were adequate for drift determination and would probably still be necessary even if the long term behavior were known.

When the magnet was first installed, it frequently quenched for reasons which were not initially understood. As experience was gained, some causes were identified and eliminated. One cause of quenching which could not be eliminated is thought to be connected with the repaired superconductive switch. The current through the switch is the difference in the solenoid current and the current in the leads to the power supply. In the semipersistent mode the switch current therefore increases as the power supply current is reduced. The magnet quenches fairly consistently if the switch current becomes greater than about 50 A. This can be explained in terms of resistance in the switch or switch solder connections. A resistance of 10^{-4} Ω and 50 or 60 A produces about as much heat as the 300 m⁴ in the heater wire used to keep the switch normal. Thus the I^2R heat associated with a small resistance at the solder joints may be enough to drive the superconductive switch normal even though it is in contact with large copper heat sinks.

The result was that the power supply had to be left engaged carrying about 30 A to keep the current in the superconductive switch below 50 A. This of course increased the helium consumption and possibly

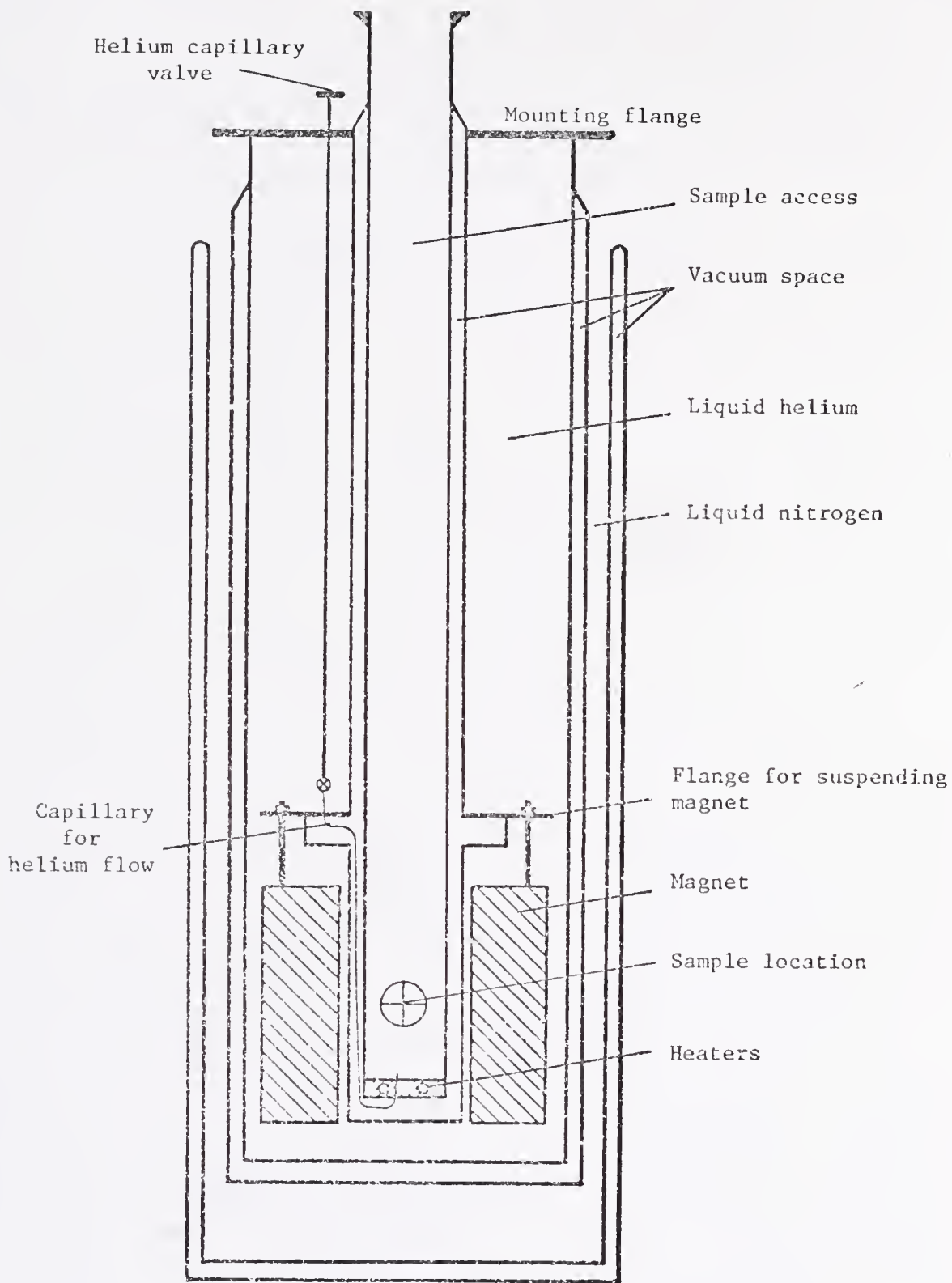


Figure 7. Top access dewar system.

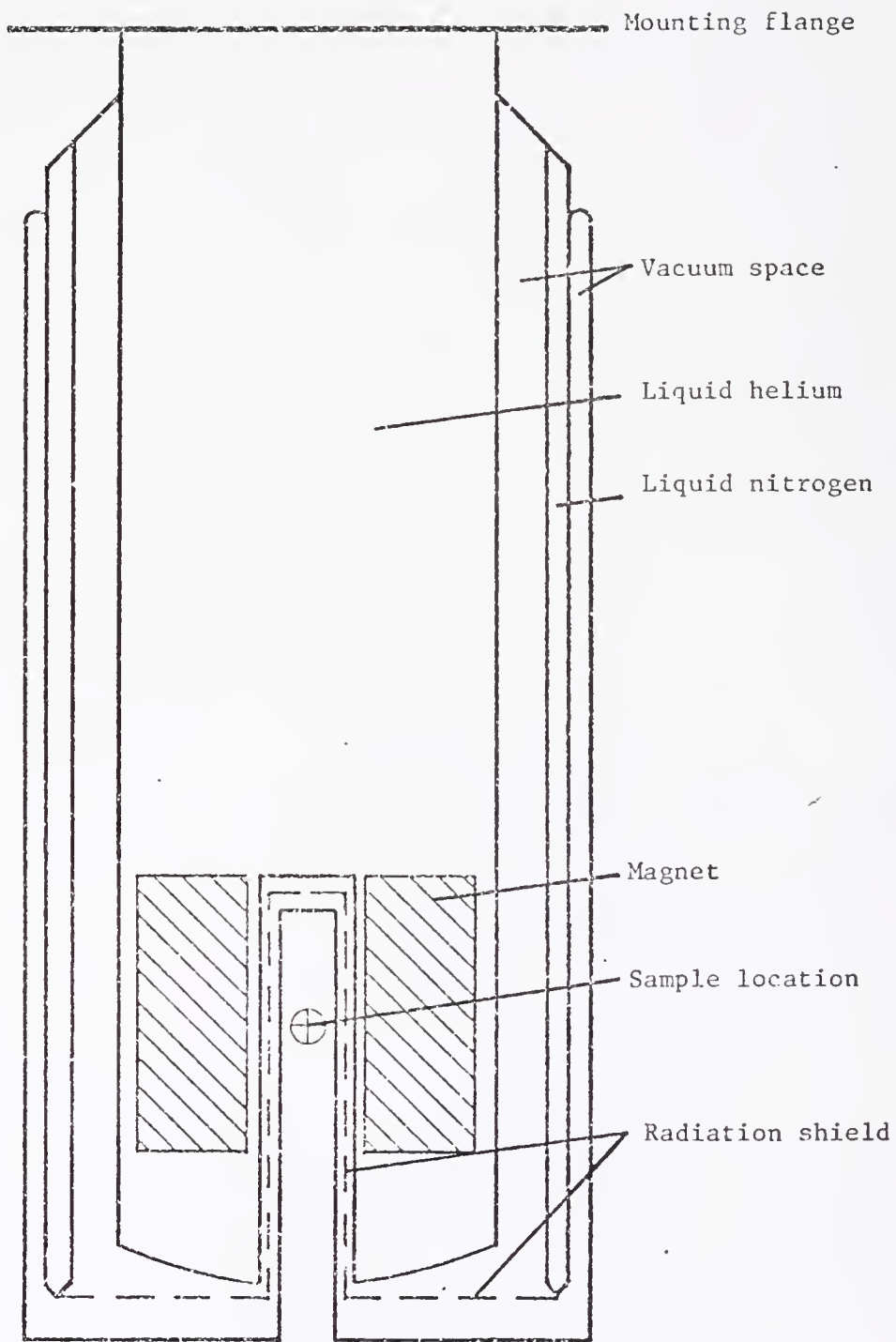


Figure 8. Re-entrant dewar system.

contributed to electronic noise. It also made the system susceptible to power failure which would not be conducive to long term operation.

3.1.2 Dewars

Two interchangeable sets of dewars were obtained for use with the superconductive magnet. The first set, manufactured by Sulfrin Cryogenics, Inc., consisted of separate nitrogen and helium dewars with top access. It was complemented by a Janis Research Company Super Vari-Temp insert assembly which supported the magnet, provided access to the working space, and provided sample temperature control. The system is shown schematically in Fig. 7.

The other system consisted of a Cryofab unit construction nitrogen and helium dewar with a common vacuum space and equipped with a re-entrant access tail. It is schematically shown in Fig. 8.

The first system has the advantage of low temperature operation and built-in temperature control. Liquid helium flow through the capillary in conjunction with either electrical heaters in the bottom of the insert or a heater added to the sample holder permits operation from 1.5 to 300 K. The obvious disadvantage is the distance from the top access flange to the working center of the magnet, about 50 in.

Lack of adequate vertical clearance in the laboratory made it necessary to either build the sample probe in sections or to shut the system down and lower it through the floor in order to insert the sample. Structural steel in the concrete floor prevented operation in the lowered position.

The re-entrant dewar had the significant advantage of easy sample access. The center of the magnetic field was only about 11 in. up from

the outside bottom of the dewar and thus the sample probe could be inserted or removed while the magnet remained at high field. Temperature control was less convenient, partly because it was not built in and partly because of the short stand-off distance from room temperature.

A gas-flow temperature control system to be described later used in conjunction with the re-entrant dewar permitted operation over a 90 to 44 K sample temperature range. The desired sample temperature could be attained and stabilized fairly rapidly but with increasing difficulty near the extremes of the range.

One problem required constant attention during operation. The helium space in the dewars was connected to the helium recovery system through the current lead feed throughs and also through a larger port. Severe thermal oscillations occurred occasionally which could be stopped by a trial-and-error adjustment of valves in the recovery lines. In general, the main valve in the recovery line from the large port in the dewar could not be opened very wide without inducing these oscillations.

The dewars were suspended on a large steel plate which could be raised and lowered on a vertical track by means of a cable and winch arrangement. The dewars alone or the whole assembly could be lowered either to gain access to the magnet or to obtain adequate overhead clearance for sample probe installation in the top access dewars.

3.1.3 Sample Probe

A sample probe, shown in Figs. 9 and 10, was constructed to position and orient the sample as well as to provide temperature control and rf connections.

The outer conductor of the rf coaxial cable doubled as structural

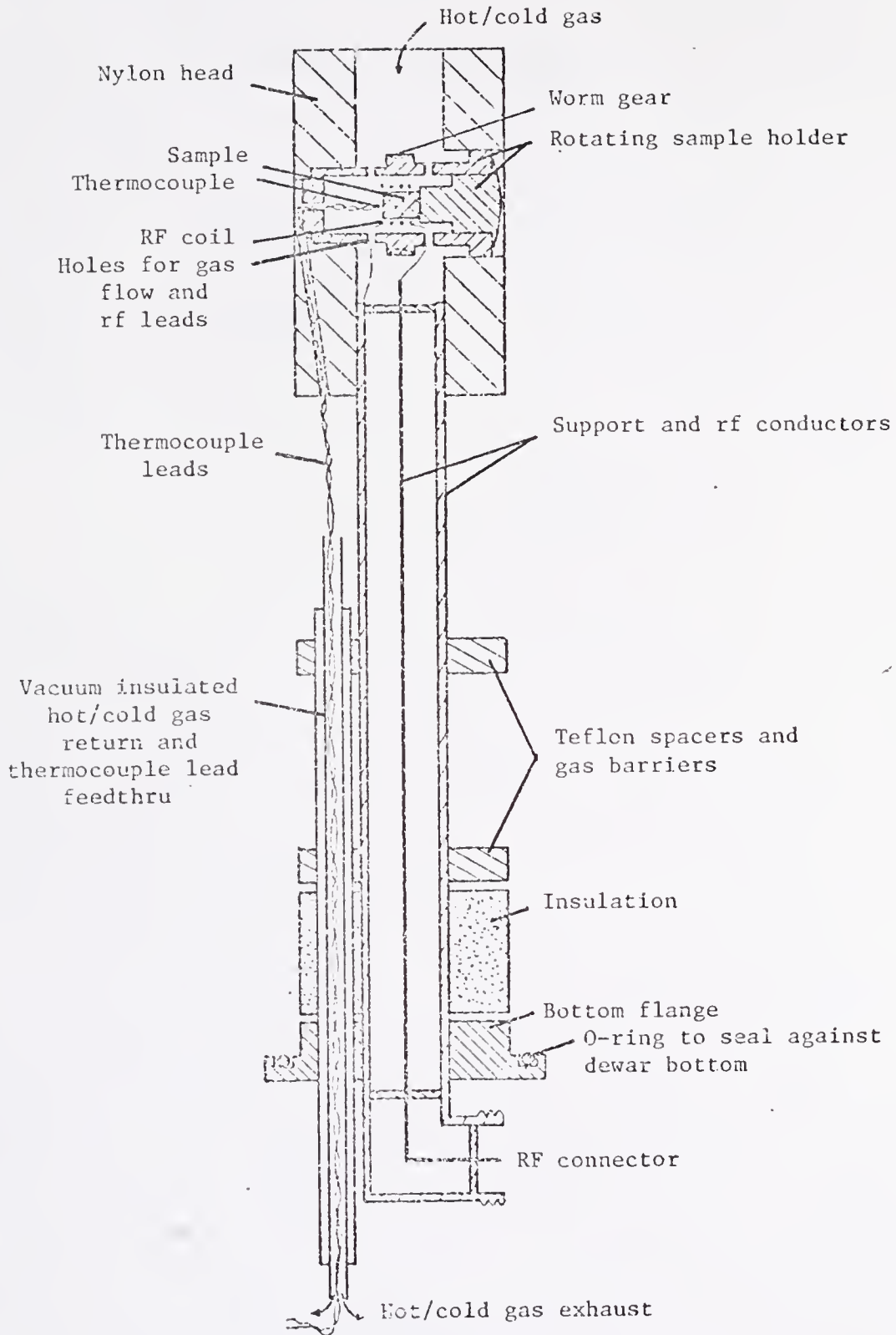


Figure 9. Sample probe, side view of sample holder.

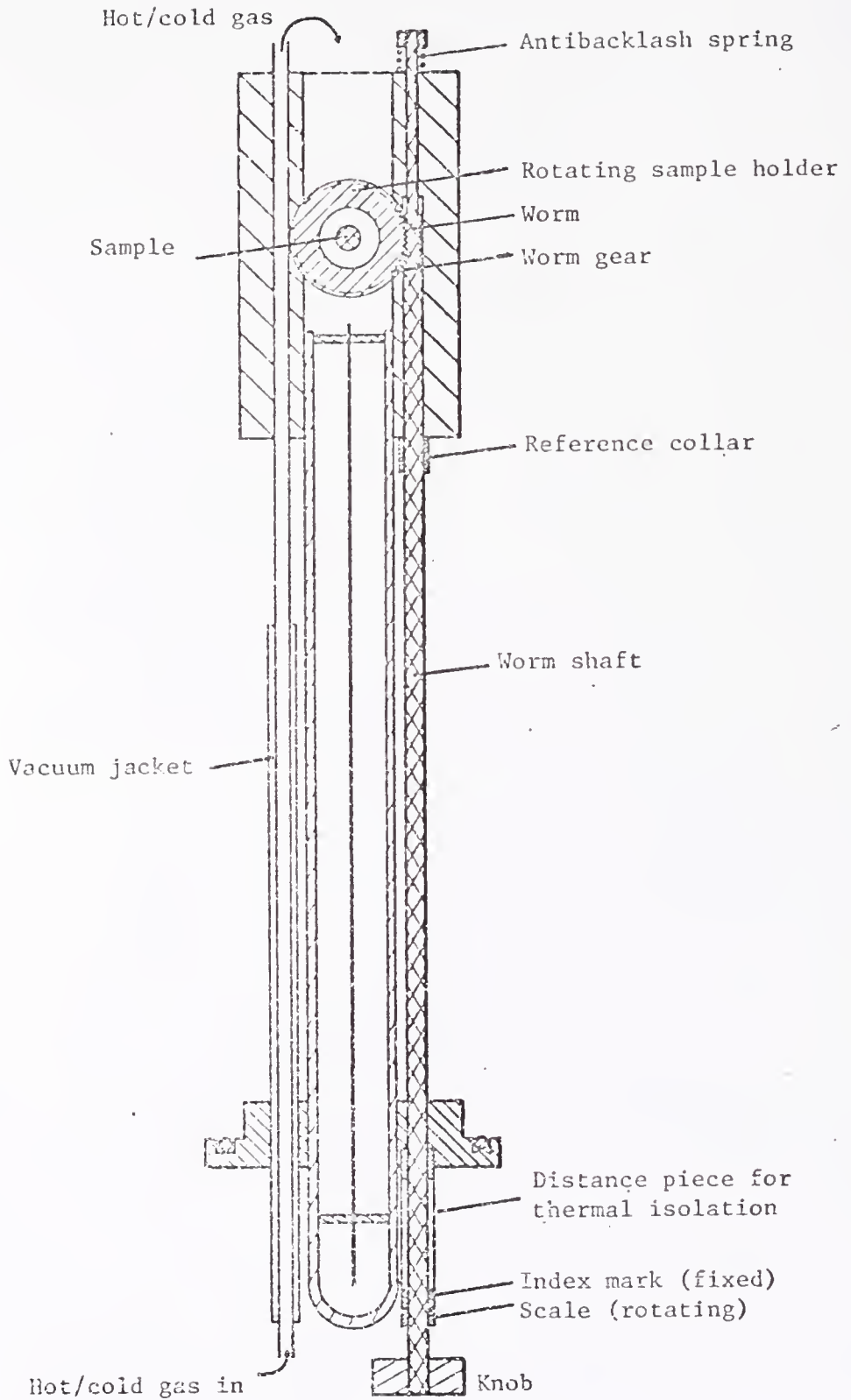
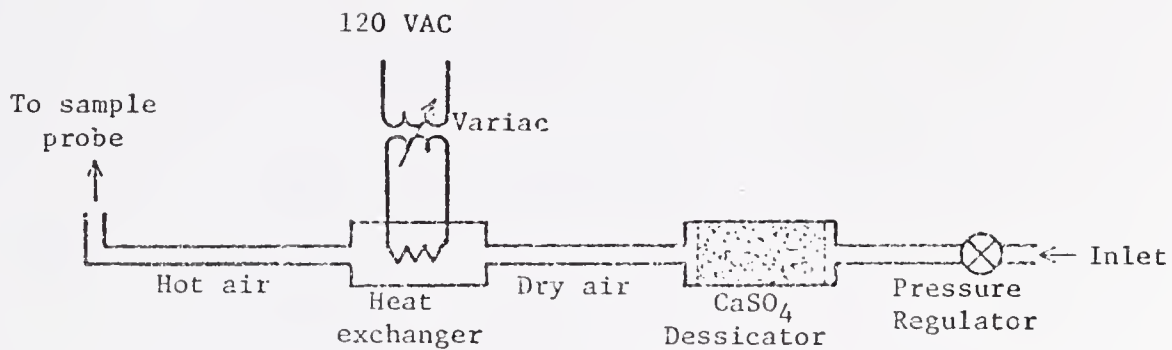
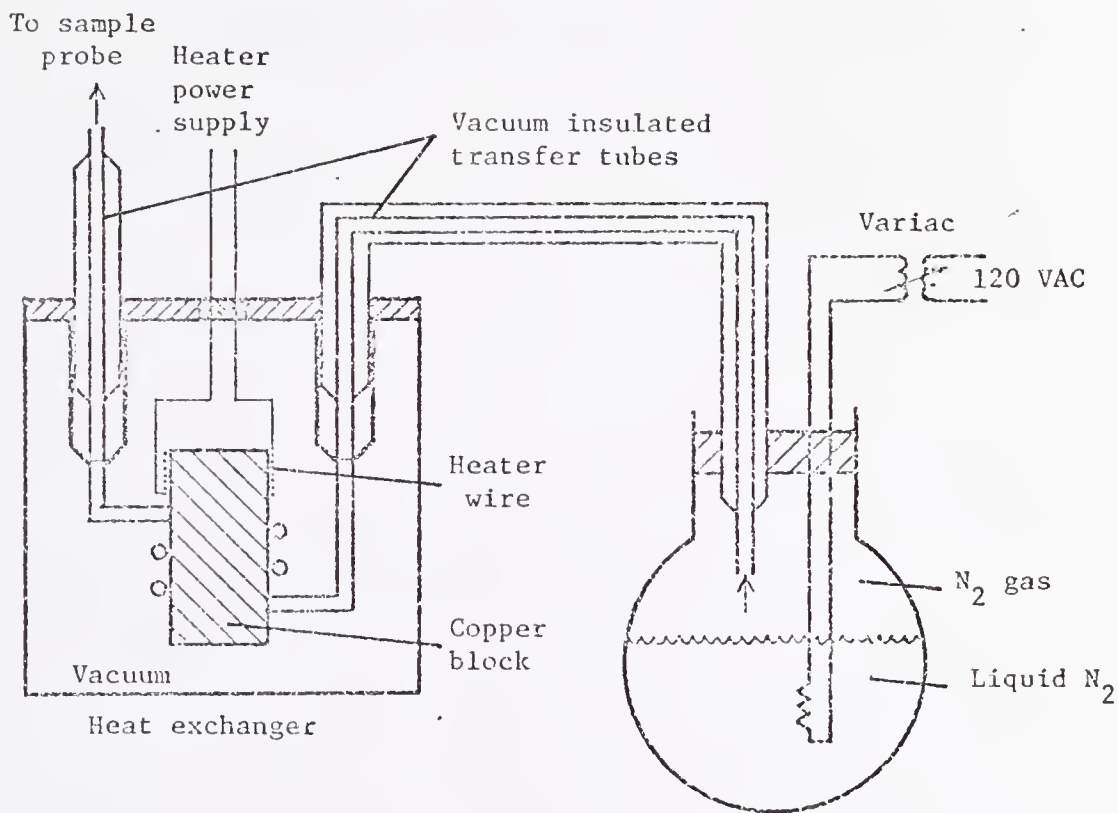


Figure 10. Sample probe, end view of sample holder.



Hot air supply



Cold N₂ gas supply

Figure 11. Gas-flow temperature control system.

support. The crystal was mounted inside a cylindrical cage-like holder which had worm gear teeth cut around its center. The angular rotation of the crystal could be controlled to within ± 2 minutes of arc relative to the initial orientation, and the initial orientation could usually be accurately determined from the data. Slack in leads from the coil to the top of the solid rf coax permitted a full 180° crystal rotation.

The entire unit fit snugly in the re-entrant tail of the dewar, leaving a small space above the nylon head. Hot (or cold) gas is passed up to this space through a 3/16-in. stainless steel tube which was vacuum jacketed up to the top spacer. The gas flows back through and around the nylon head to the space below, where it exhausts through a 1/4-in. vacuum jacketed tube.

A uniform temperature is maintained in the space above the top Teflon spacer by a combination of gas flow rate and insulation. Near room temperature there is only a small temperature gradient between the sample area and ambient temperature outside the dewar, providing little heat loss. At higher temperatures, a much higher hot gas flow rate is used which offsets the greater heat loss through the insulation without significantly cooling the gas. A similar situation applies at low temperatures.

A thermocouple close to the sample was used to measure temperature and was adequate in view of the weak temperature dependence encountered.

The gas-flow systems for operation both above and below room temperature are shown in Fig. 11. For high temperature operation, air was passed through a pressure regulator, desiccator, and electrical heat exchanger. Manual adjustment of inlet air pressure and heat exchanger voltage provided better than 1 K stability with reasonably infrequent

adjustments.

The low temperature system operated on cold nitrogen gas boiled off by passing current through a 25- Ω resistance immersed in liquid nitrogen. Stability was enhanced by passing the gas through copper tubing wound around a copper block which provided thermal inertia. Temperature variation was predominantly provided by varying the current through the 25- Ω resistance in the liquid nitrogen supply, with additional control achieved by means of a resistance-wire heater on the copper block.

The systems were operated over a range from 90 to 440 K. Higher temperatures would have been readily obtainable with no modification to the system, the limit being the ability of the sample probe to withstand the heat. Initially, an rf coaxial cable was inserted in the probe all the way up to just below the sample holder, but plastic spacers inside the cable melted at 167°C. The nylon worm gear assembly also deformed and seized at high temperatures. These problems were corrected by use of rigid rf conductors as shown in Fig. 9 and by slightly increasing clearances between moving parts.

Somewhat lower temperatures should be possible with some modification to the system. The inlet gas tube could be passed through the liquid nitrogen to insure it is as cold as possible prior to entering the vacuum transfer tubes. Also, pumping on the exhaust tube to increase gas flow rather than passing current through resistors in liquid nitrogen would have the additional effect of depressing the boiling point.

3.1.4 Operation of the Superconductive System

It was generally best to start cool-down about three days before the actual run. Simply maintaining liquid nitrogen in the liquid nitrogen dewar would cause the magnet temperature to lower to an estimated 81-83 K in that time period and an extra day would result in lowering the temperature 2 to 3 degrees.

It was also possible to precool rapidly by introduction of liquid nitrogen into the helium dewar in direct contact with the magnet, but this method required back transfer which was more trouble than keeping the outer jacket full of liquid nitrogen.

Overhead clearance limited the length of the helium transfer tube so when fully inserted it would reach roughly one third of the way down from the top. Thus, a vacuum jacketed extension was required, but it was also desirable to be able to pull the extension up out of the liquid once liquid helium was in the dewar. This was especially important to avoid passing warm gas through the liquid when starting a replenishment transfer. Therefore, a vacuum jacketed extension was made which extended through the top flange of the dewar where it was terminated with a ball valve.

This extension could be lowered for insertion of the transfer tube and for initial transfer when it was desirable to have the cold gas pass up around the magnet from below. For replenishment, it could be raised part way, and between transfers it could be raised well above the liquid helium to reduce the heat path.

During cool-down, a pressure in the supply dewar of about 5 in. H_2O above recovery line pressure would be the maximum the recovery system would take, but once liquid helium started collecting, 40 in.

H₂O pressure or more could be used. Only a few minutes would be required to collect about 25 liters after a 45-min cool-down from liquid nitrogen temperature.

Once-a-day replenishment was generally adequate. Helium consumption was about 2 liters/h during the time the field was being either increased or decreased and was as low as 0.3 liter/h with the system shut down. Vibrations fed back from the recovery compressor, thermal oscillations, changes in recovery line pressure, current in the electrical leads, and possibly other factors affected the helium consumption which usually averaged about 20 liters/day including that lost while cooling the warm transfer tubes during replenishment transfers.

Moveable level resistors in both the experimental and supply dewars made it very easy to monitor liquid helium levels. The rather simple level indicators exhibited only a small needle deflection as the resistor passed from one side of the surface to the other so needle movement while dipping the resistor in and out of liquid helium was a much more positive indication than absolute needle position.

A Magnion CFC-100 power supply was used to charge the solenoid. A 40-turn wire-wound potentiometer, motor driven at a selected rate, controlled the rate of current increase. A maximum rate of 2.0 A/min was allowed, which required 45.5 min to bring the magnet up to 100 kG. It was discovered that the core of the 40-turn potentiometer had a high coefficient of thermal expansion and would sometimes shrink so much that the wire would loosen and cause intermittent contact with the wiper which would result in the magnet quenching. The 40-turn potentiometer had to be replaced with one having only 10 turns. With this potentiometer the fastest charging rate without exceeding 2.0 A/min was

1.6 A/min which increased charging time by 25%.

Prior to placing the magnet in the semipersistent mode, the magneto-resistive voltage and power supply dial reading were recorded. The power supply current could then be reduced to about 30 A with the magnet in the semipersistent mode. At the end of the run, the magneto-resistive voltage was again noted which would be somewhat lower than the initial reading. The power supply current would be brought up to a proportionately lower reading prior to opening the superconductive switch. The power supply current and the magnet current would be closely matched in this condition, any difference between them being through the superconductive switch. When the switch is opened by driving it to the normal state, the current in it causes a voltage to develop across it, normally less than 25 mV. In case of too great a mismatch of currents, the voltage would be high enough to cause the power supply to quench which would result in the magnet discharging through a 2- Ω shunt across the terminals. Under these conditions the magnet would be de-energized in a few minutes with little loss of liquid helium.

As mentioned already, various causes would result in quenching the magnet, and it would very rapidly de-energize, generally boiling off all the liquid helium in the dewar but not warming up appreciably. The recovery system was not capable of handling such a large flow rate, so most of the helium would be lost to the atmosphere through a safety valve. A helium gas bag is needed to prevent this loss. It appears that the primary remaining cause of quenching is excessive current in the superconductive switch which can be avoided by leaving the power supply on and carrying part of the current.

3.2 Electromagnet System

3.2.1 Electromagnet

A Varian V-4012-3B 12-inch electromagnet with a 3.5-in. gap was used for the ^{15}N line shape and relaxation studies. The magnet was capable of providing magnetic fields of up to 9000 G. A Varian V-2100B magnet power supply and a Varian V-FR-2100 Fieldial field regulator were used to operate the magnet in the field-regulation mode.

Drift rates of up to about 1 G/h were encountered whereas a change of as little as 0.03 G would sometimes cause significant inaccuracies in the data. It was sometimes possible to correct for the drift rate once it was known; however the drift rate varied and even reversed direction throughout the day, especially when the laboratory temperature was fluctuating due to intermittent operation of air conditioning.

3.2.2 Cryostat and Sample System

A schematic diagram of the cryostat is shown in Fig. 12. The sample cell was made of Kel-F and had a volume of about 1.8 cm^3 . The space around it contained helium exchange gas for thermal contact with the surrounding copper can which contained the heater and thermometer. Exchange gas in the brass can was used to control thermal contact with the cryogenic fluid outside the brass can. The sample gas down pipe doubled as the center rf conductor, and the sample assembly was supported by a double walled tube which also served as the outer rf conductor. The space between the walls was evacuated to thermally isolate the sample gas down pipe from the surrounding cryogenic fluid. The sample gas down pipe was electrically insulated from the external

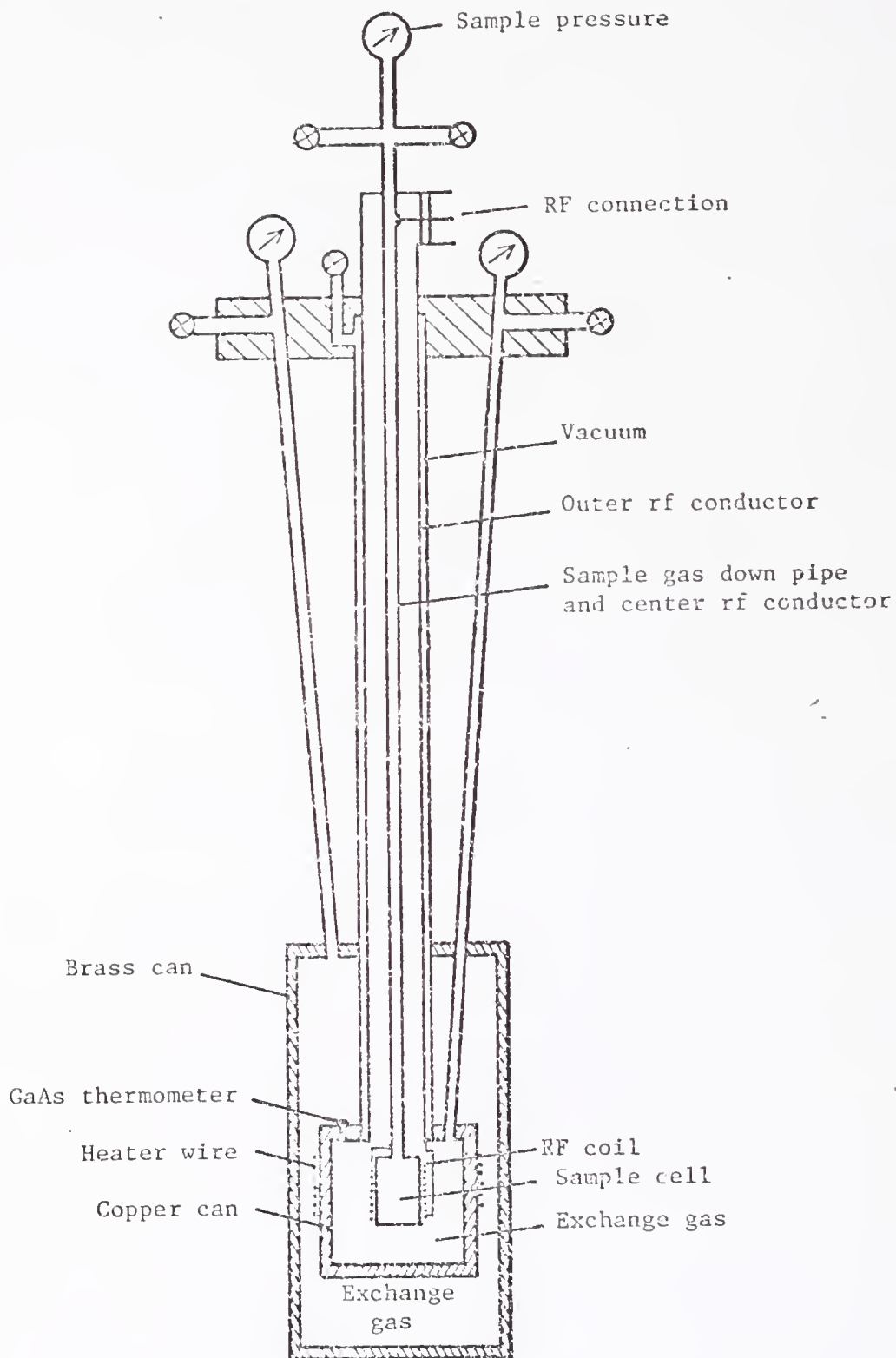


Figure 12. Cryostat used with electromagnet.

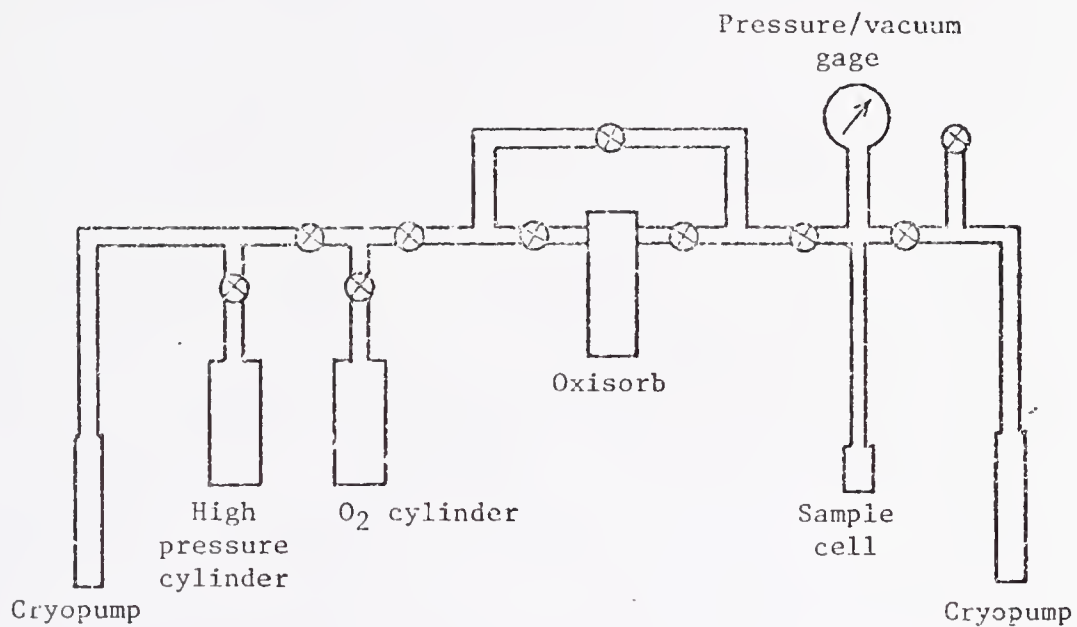


Figure 13. Sample-gas system.

plumbing by an arrangement not shown on the drawing.

Temperature control was provided for by a GaAs thermometer and resistance heater wire installed on the copper can surrounding the sample cell containing exchange gas, and by varying the exchange-gas pressure outside the copper can to vary thermal contact with the cryogenic fluid.

Figure 13 is a schematic of the sample-gas system. The sample gas was normally stored in the high pressure cylinder. Prior to releasing the sample to the rest of the system, the pressure was reduced to approximately one atmosphere by immersing the cylinder in liquid nitrogen. The gas was then moved around by controlling the temperature of the sample cell, the high pressure cylinder, and the two cryopumps. Ideally, thermal isolation of the sample cell and down pipe would have permitted operation with liquid helium as a cryogenic fluid over a wide temperature range. In practice, if helium was used during the sample condensation stage, the down pipe would freeze up and block before the sample was condensed in the sample cell. Part of the problem was due to an uninsulated tube which passed up through the cryogenic fluid connecting the copper sample cell to room temperature. This provided some thermal contact even when the exchange gas was removed from the outside of the copper can. Rather than modifying the cryostat, pumped liquid and solid nitrogen were used while condensing the sample and for operation above 50 K.

The sample-cell temperature would be maintained at about 65-67 K while the remainder of the sample system was gradually warmed, thus condensing the sample in the sample cell as it boiled off from other parts of the sample system. The pumped liquid or solid nitrogen could

then be used as the cryogenic fluid (or solid below 63 K) or it could be replaced by liquid helium for lower temperature operation.

3.3 Spectrometers

3.3.1 Pulse spectrometer

Various pulse spectrometer combinations were used depending on equipment availability and the type of measurements to be made.

It was normally not possible to observe the free induction decay (FID) of ^{14}N in a glycine directly without signal averaging. Thus it was necessary to adjust the frequency by small increments and signal average after each adjustment to first detect the signal and then to determine the frequency, a very tedious process. Under these conditions, the Fast Fourier Transform (FFT) technique was employed. The Fourier transform of the FID is the frequency spectrum or absorption line with respect to the oscillator frequency as the reference. Thus, if the oscillator frequency is displaced below the central frequency, the peak of the absorption line will be offset above the origin, and the amount of offset is added to the oscillator frequency to determine the central frequency. Hence it is only necessary to set the oscillator frequency close to the frequency of the signal.

Complex Fourier transformation capability would provide information as to whether the offset is above or below the oscillator frequency. Equipment used in the present work did not have complex capability, and only the frequency differences could be found. The ambiguity as to whether the offset is above or below the oscillator frequency had to be resolved by other means. The usual method was to change the oscillator

frequency and note whether the offset increased or decreased.

It is not only unnecessary to set the oscillator frequency to the central frequency of the line, it is undesirable without complex Fourier transform capability. If the oscillator frequency is within the frequency spectrum of the line, parts of the spectrum equal distances above and below the oscillator frequency will be added, thus distorting the frequency spectrum.

The spectrometer used in conjunction with the FFT equipment had frequency stabilization provided by a General Radio Model 1061 Frequency Synthesizer. It could be set digitally in 10 Hz increments and incorporated a search mode by which any digit position could be replaced by a continuously variable value. For example, replacing the 10 Hz digital control permitted a continuous variation over a range from -20 Hz to 100 Hz below or above the frequency set on the other controls.

An F and H Instruments Pulse Program Generator PPG 45 permitted considerable flexibility in choice of pulse sequence, width, separation, repetition rate, etc.

A locally made Quadrature Phase Sensitive Detector was especially convenient when it was desired to monitor the tuning while recording data. When the frequency and phase are properly adjusted, the FID amplitude is a maximum while the quadrature output is flat, and a drift off resonance is easier to detect relative to a flat response. This of course was not used when the oscillator was deliberately set off resonance.

Each FID was recorded by a Biomation Model 801 Transient Recorder and transferred to a Fabri-Tek Instruments, Inc., Model 1072 Instrument Computer for accumulation.

After accumulation of an adequate number of signals, a Digital Equipment Corporation PDP 8/E computer was used to perform the FFT.

While observing the NQR-perturbed ^{14}N Zeeman resonance in glycine, the frequency of the unperturbed ^{14}N Zeeman line was periodically determined by means of a liquid ammonia sample. From these data and the calculated drift rate of the superconductive magnet, the unperturbed frequency was calculated for each time at which data were recorded.

After performing the FFT, the displacement of the line center from the origin was measured in frequency units and the correction was applied to the oscillator frequency, resulting in the actual frequency of the NQR-perturbed line. Finally the difference between this frequency and the frequency of the unperturbed ^{14}N Zeeman line was determined which was the frequency shift of interest.

When using the same spectrometer to measure T_1 of ^{15}N in liquid and β -solid $^{15}\text{N}_2$, the amplitude of the FID was sampled over a short section near the origin. Successive amplitudes were recorded in successive channels of the Biomation Transient Recorder. When enough data were recorded, they were transferred to the Fabri-Tek Instrument Recorder and T_1 was then calculated by the PDP 8/E computer using a FOCAL program. A series of 90-t-90 pulse sequences were used, separated by at least $6T_1$ in order to allow the spin system to reach equilibrium before the next sequence. Thus, the first pulse would yield the amplitude at equilibrium and destroy the z component of the magnetization, and the second pulse would yield the recovery amplitude after time t. The difference between the two amplitudes decreases exponentially with increasing t, and the pair-wise differences versus t were used to calculate T_1 .

This method of measuring T_1 had the advantage of requiring only a

single sampling point on each FID. It was not necessary to determine the base line which would be required to get the correct amplitude, as only differences in amplitudes were required. It had the disadvantage of requiring a long wait between pairs of pulses as a new determination of the equilibrium magnetization was required each time. The long wait also subjected the data to more errors due to magnetic field drift and instabilities of the electronics.

Another pulse sequence, τ -90- τ -180 following complete saturation, was also used. In this method, a Princeton Applied Research TDH-9 Waveform Eductor was used to record the echo following a 180° pulse. The echo was then displayed on an oscilloscope where the echo amplitude could be determined by comparison with a scale on the screen. The base line on both sides of the echo was visible so the absolute amplitude could be determined.

This method was much faster, as it was not necessary to wait between pulse sequences. However, it depended on visual estimation of the pulse height rather than an electronically determined amplitude averaged over a short section.

3.3.2 Continuous Wave Spectrometer

A continuous wave (cw) spectrometer was used to determine the ^{15}N NMR line shape of solid $^{15}\text{N}_2$ and of a $^{15}\text{N}_2$: ^{15}N - ^{14}N : $^{14}\text{N}_2$ = 1:4:4 mixture.

A locally constructed Robinson oscillator could be operated over the entire range of frequencies (270 kHz to 4 MHz) with the appropriate rf coil and capacitance in the sample circuit. It could be frequency swept, the sweep being controlled by voltage variable capacitors. A 5-kHz sweep at 270 kHz turned out to be nonlinear, and therefore

magnetic field sweep was normally used.

A Princeton Applied Research Model HR-8 Lock-In Amplifier was used to detect the signal and a Hewlett Packard Model 201C Audio Amplifier and a Ling Electronics Model TP100 Power Amplifier provided field modulation.

The derivative line shape was recorded by the Fabri-Tek Instrument Computer which was also used to integrate the line shape to obtain the absorption line shape. Both derivative and integrated line shapes were recorded on paper by an X-Y recorder.

CHAPTER IV
RESULTS AND DISCUSSION -- GLYCINE

4.1 Glycine Structure

Glycine, $\text{NH}_2\text{CH}_2\text{COOH}$ (or $\text{NH}^{3+}\text{CH}_2\text{OO}^-$), is the simplest of the amino acids. It crystallizes in one of three forms, α , β , or γ , depending on the preparation conditions. Crystals grown from an aqueous solution form α glycine, the most common and stable. Addition of ethyl alcohol to the solution results in β glycine, and γ glycine is obtained by addition of acetic acid or ammonium hydroxide to make the solution acidic or basic.

Structures of the α , β , and γ forms were reported by Albrecht and Corey [16], Iitaka [17], and Iitaka [18], respectively, and Marsh [19] reported a refinement of the structure of α glycine.

Crystals studied in the present work were of the α glycine form, grown, cut, and mounted at the University of Nottingham. Reference [16] has some excellent drawings of α glycine, though reference [19] probably contains more accurate data.

The molecule is shown in Fig. 14. Two enantiomorphous forms of the molecule occur. The second form would be obtained by reversing the sign of all the numbers in parentheses in Fig. 14, i.e., putting atoms shown above the O_I, O_{II}, C_{II} plane below and vice versa. Only one form occurs in β and γ glycine, whereas both are found in α glycine.

The two forms described above would be mirror images of each other

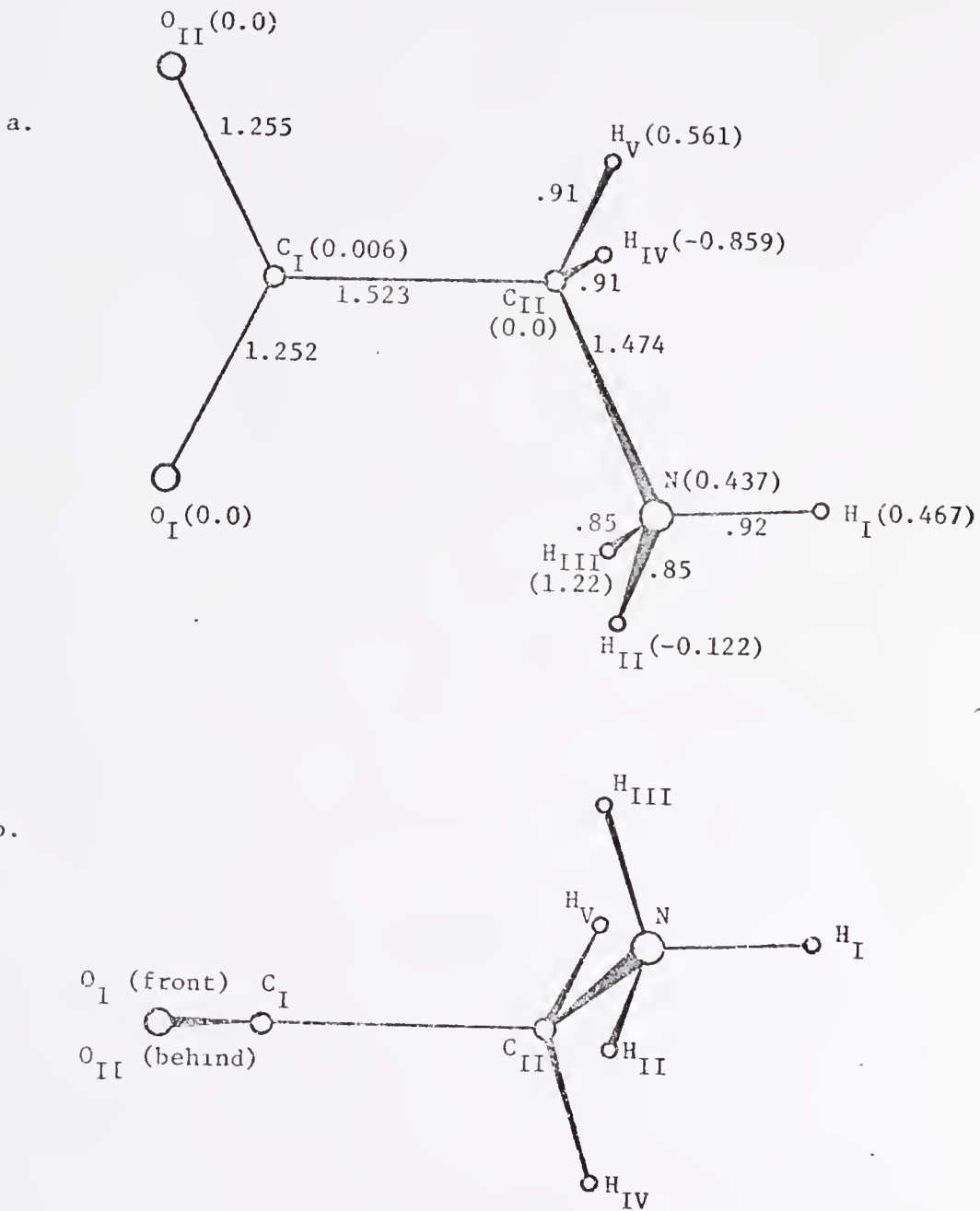


Figure 14. Glycine molecule. (a) Viewed normal to the O_I, O_{II}, C_{II} plane. Bond distances are in Å. Numbers in parentheses are distances in Å above (+) or below (-) the plane. (b) View parallel to the O_I, O_{II}, C_{II} plane showing the molecule is rather flat except for the protons.

in a reflection plane parallel to the O_I, O_{II}, C_{II} plane. A point inversion of one form would also result in the other form, in which case any line, such as the lines representing bonds in Fig. 14, would be antiparallel to the corresponding line in the other form.

The α -glycine crystal is monoclinic with four molecules per unit cell. Unit cell dimensions are [19]

$$a = 5.1020 \pm 0.0008 \text{ \AA}$$

$$b = 11.9709 \pm 0.0017 \text{ \AA}$$

$$c = 5.4575 \pm 0.0015 \text{ \AA}$$

$$\beta = 111^\circ 42.3' \pm 1.0'$$

A typical crystal is shown in Fig. 15, together with a set of crystal axes $\Sigma = X, Y, Z$, which will be used in the discussion. Figure 15 is similar to Fig. 1 in reference [1] for purposes of consistency.

Figure 16 shows the arrangement of molecules in α -glycine. The molecules are identified by A_1, A_2, B_1, B_2 corresponding to D, C, A, B, respectively, in reference [16]. The N atom in B_1 is bound to O_{II} in B_2 and to O_I in an adjacent B_2 molecule, binding B_1 and B_2 layers in a double layer. The double B layer is loosely bound to the double A layer by van der Waals forces, which is the reason for the (010) cleavage plane.

4.2 Electric Field Gradient Tensors

There are 4 inequivalent N sites; however, B_1 and B_2 are related by point symmetry. Components of the EFG tensors at the N site in B_1 and B_2 are therefore antiparallel, and being a second rank tensor, parallel and antiparallel cannot be distinguished. Thus, EFG tensors are equivalent at the two sites. Considering the A molecules, there

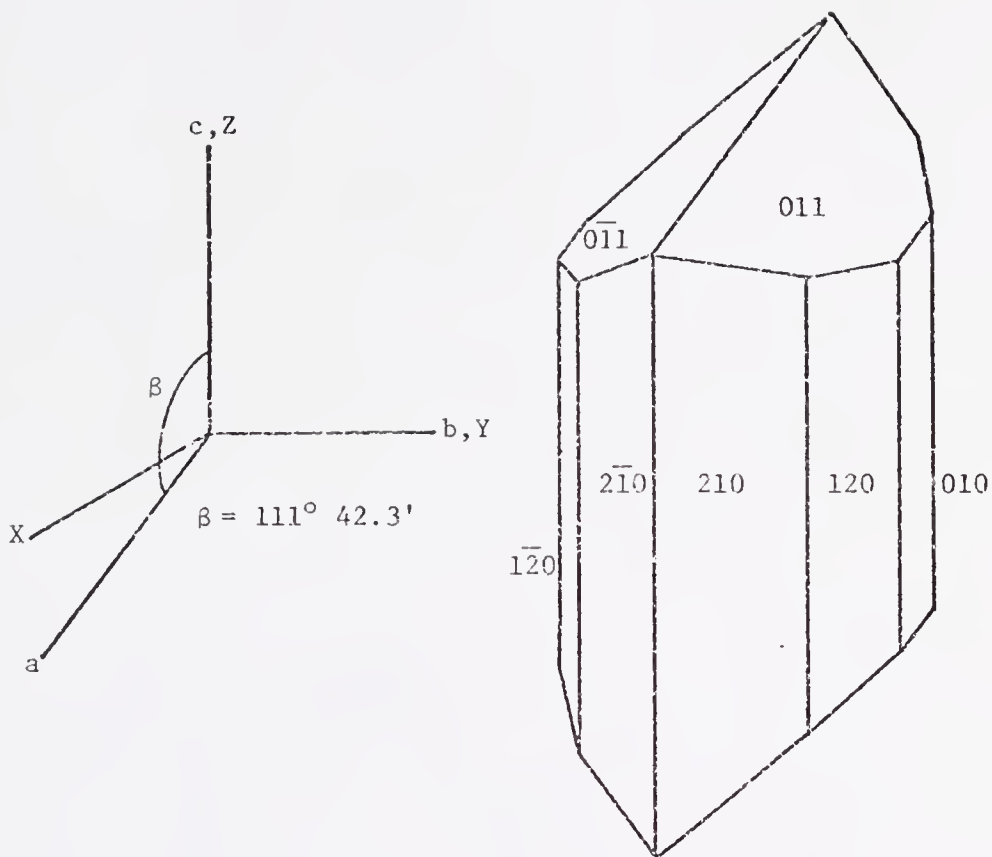


Figure 15. Typical α -glycine crystal. The $\{011\}$ and $\{120\}$ faces appear most frequently although $\{210\}$ faces also appear. The $\{010\}$ faces are readily obtained by cleavage.

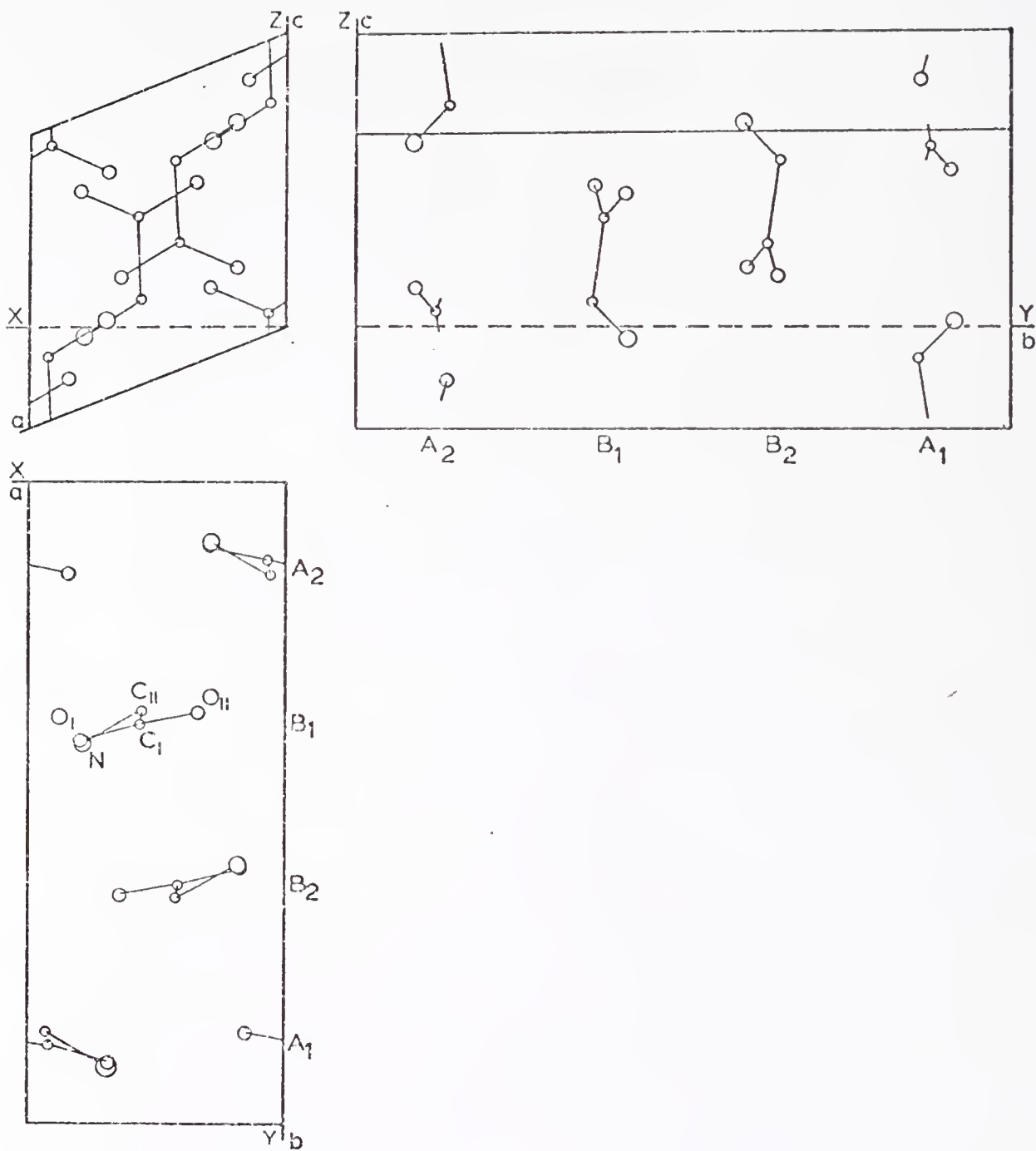


Figure 16. Unit cell of a glycine. Axes are defined in Fig. 15. Molecules A₁ and B₁ are of the enantiomorphic form shown in Fig. 14, and are related by point inversion symmetry to A₂ and B₂. Molecules B₁ and B₂ form a double layer which is loosely bound to the A₁, A₂ layer.

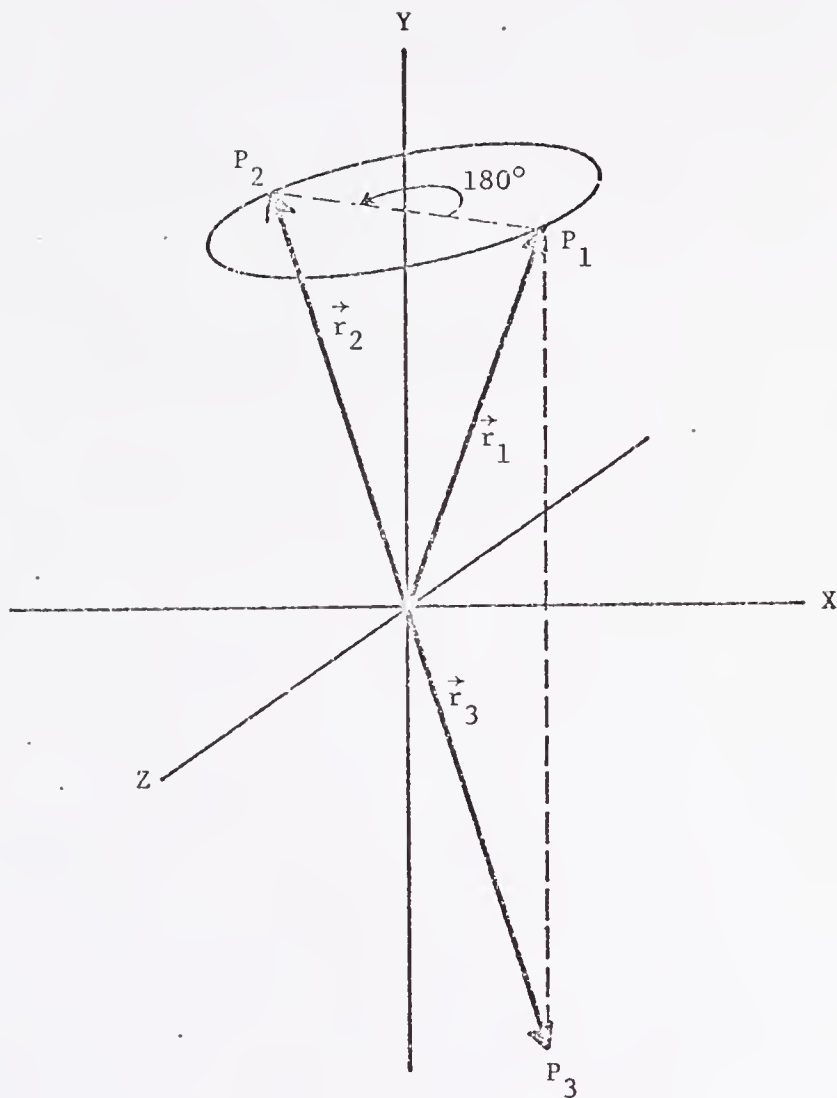


Figure 17. A vector \vec{r}_1 undergoing a 180° rotation about the Y axis would bring it to \vec{r}_2 , whereas a reflection in the X,Z plane would bring it to \vec{r}_3 , where $\vec{r}_2 = -\vec{r}_3$. A tensor component has no positive or negative sense, and therefore the 180° Y-axis rotation and the X,Z plane reflection are equivalent. Hence the EFG tensors from sites A and B are related by a 180° Y-axis rotation or, equivalently, an X,Z reflection plane.

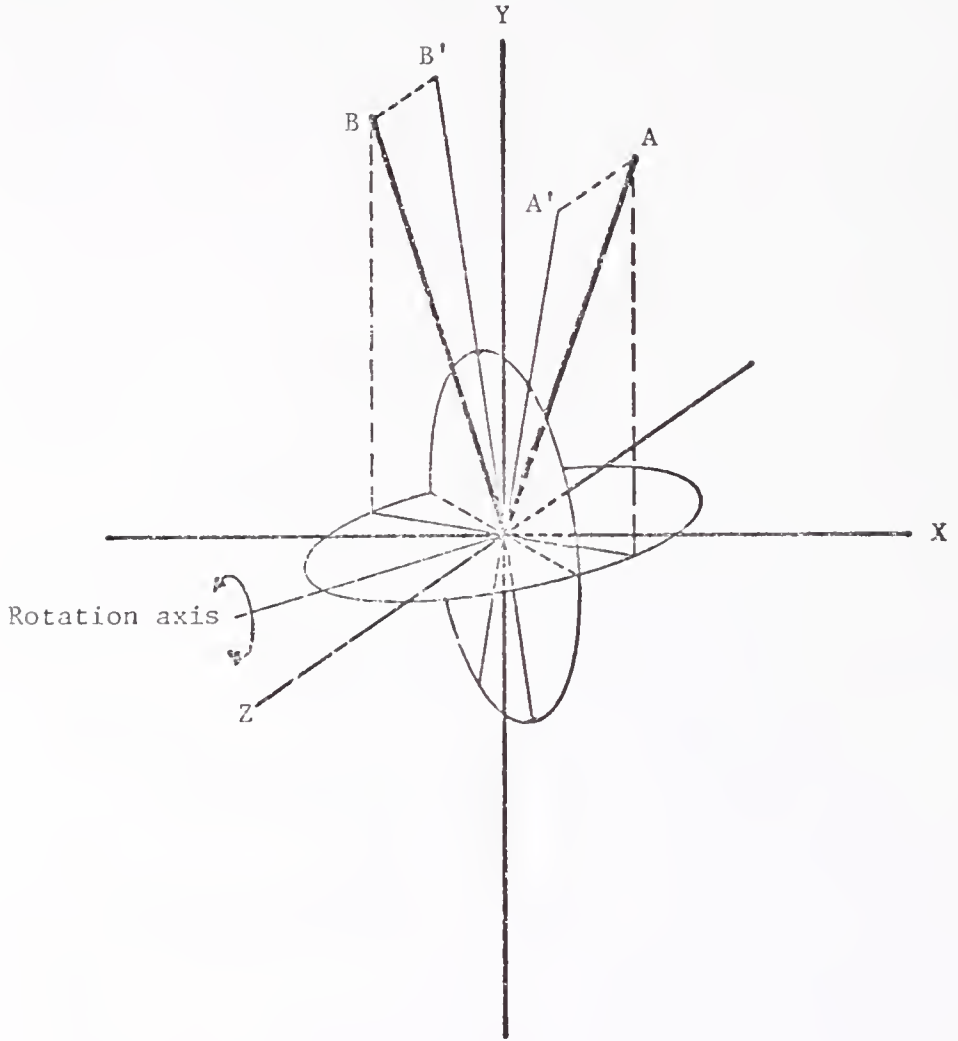


Figure 13. Symmetry of rotation patterns for rotation axes in or normal to the X,Z plane. Let A' and B' be projections of A and B, respectively, in the rotation plane for any axis in the X,Z plane. The projections are symmetric about the Y axis and about the X,Z plane (some detail omitted below the X,Z plane to reduce clutter). For a Y-axis rotation, rotation patterns from sites A and B merge as projections in the rotation plane are parallel.

are two inequivalent EFG tensors, one for site A and one for site B.

Reference to Fig. 16 shows that a 180° rotation of the A layers about an axis parallel to the Y axis would make the A layer equivalent to the B layer. The two EFG tensors are therefore related by such a 180° rotation, or equivalently by a reflection in the X, Z plane, as shown in Fig. 17.

It is seen from Fig. 18 that the rotation patterns obtained from sites A and B are symmetric for any axis in the X, Z plane when the initial orientation is chosen with \vec{H}_0 in the X, Z plane or normal to it. Site A and a clockwise rotation results in the same pattern as site B and a counterclockwise rotation. Furthermore, this requires the two patterns to coincide when \vec{H}_0 is in the plane or normal to it. A rotation about the Y axis would result in a single curve, as the projections of both EFG tensors on the rotation plane would coincide.

These considerations affect the choice of rotation axes. A Y-axis rotation would result in a single curve for $(2\Delta\nu)_Y$, taking no advantage of the fact that there are two inequivalent sites, other than alignment information. A single curve would confirm that the rotation axis was parallel to the Y axis, and two curves would mean the axis was not quite parallel to Y.

A rotation axis in the X, Z plane would result in two curves, symmetric about the $\theta = 0$ or $\theta = 90^\circ$ orientations. Thus, the $\theta = 0$ orientation could be accurately determined, and if the curves were not symmetric in amplitude or offset, it would be due to the rotation axis being somewhat out of the X, Z plane. Again, the symmetry of the two sites would provide only orientation information, and three such rotation patterns would be needed to solve the problem completely.

Using the convention that upper signs go with site A and lower with site B where the signs differ, X, Y, and Z rotations would result in the following rotation patterns:

$$\begin{aligned}
 (2\Delta v)_X &= A_X + (B_X^2 + C_X^2)^{\frac{1}{2}} \cos 2(\theta_X \mp \delta_X) \\
 &= A_X + B_X \cos 2\theta_X \pm C_X \sin 2\theta_X \\
 (2\Delta v)_Y &= A_Y + (B_Y^2 + C_Y^2)^{\frac{1}{2}} \cos 2(\theta_Y - \delta_Y) \\
 &= A_Y + B_Y \cos 2\theta_Y + C_Y \sin 2\theta_Y \\
 (2\Delta v)_Z &= A_Z + (B_Z^2 + C_Z^2)^{\frac{1}{2}} \cos 2(\theta_Z \mp \delta_Z) \\
 &= A_Z + B_Z \cos 2\theta_Z \pm C_Z \sin 2\theta_Z
 \end{aligned} \tag{4.2.1}$$

where $\tan 2\delta = C/B$.

Any of the six curves will furnish the diagonal elements of the EFG tensors, which are the same for both sites. One off-diagonal element comes from each rotation, and off-diagonal elements from the two sites have the same magnitude, differing in sign only in two cases. The complete tensors, in terms of coefficients in equation (4.2.1), are

$$\frac{1}{K} \begin{pmatrix} -2A_X & \mp C_Z & -C_Y \\ \mp C_Z & -2A_Y & \mp C_X \\ -C_Y & \mp C_X & -2A_Z \end{pmatrix}, \tag{4.2.2}$$

where other choices could have been made for the diagonal elements. Here $K = 3eQ/2I$, as in (2.4.11) and will be suppressed for simplicity in the following.

The symmetry of the EFG tensors at sites A and B is displayed in (4.2.2), where the only differences in the elements are $\phi_{XY}^A = -\phi_{XY}^B$ and

$\phi_{YZ}^A = -\phi_{YZ}^B$. For a general choice of crystal axes, the elements of the A tensor would not have the same magnitude as those of the B tensor, unless by coincidence.

Suppose a $\Sigma^U = U, V, W$ frame is chosen, and a V-axis rotation is performed. The rotation patterns for sites A and B would be

$$\begin{aligned} (2\Delta\nu)_V &= A_V + B_V \cos 2\theta_V + C_V \sin 2\theta_V \\ (2\Delta\nu)_V' &= A_V' + B_V' \cos 2\theta_V' + C_V' \sin 2\theta_V' \end{aligned} \quad , \quad (4.2.3)$$

for sites A and B respectively, the prime indicating site B. The corresponding tensors would be

$$\begin{pmatrix} \frac{A_V - B_V}{A_V' - B_V'} & \frac{\psi_{UV}}{\psi_{UV}'} & \frac{-C_V}{-C_V'} \\ \frac{\psi_{UV}}{\psi_{UV}'} & \frac{-2A_V}{-2A_V'} & \frac{\psi_{VW}}{\psi_{VW}'} \\ \frac{-C_V}{-C_V'} & \frac{\psi_{VW}}{\psi_{VW}'} & \frac{A_V + B_V}{A_V' + B_V'} \end{pmatrix} \quad , \quad (4.2.4)$$

the upper and lower values belonging to the site A and site B tensors, respectively, as indicated by the primes. Here ψ 's have been used to avoid confusion in distinguishing between the Σ and Σ^U frames. There are four unknowns, compared to only two which would result in tensor (4.2.2) if a single Y rotation were performed. If the tensor (4.2.4) is transformed to the Σ frame, it must have the symmetry of (4.2.2) which permits solving for the four unknowns.

The transformation is

$$\phi_{kl} = \sum_{i,j} a_{ki} \psi_{ij} a_{jl}^{-1} = \sum_{i,j} a_{ki} a_{lj} \phi_{ij} \quad , \quad (4.2.5)$$

where k, l stand for X, Y, Z, and $i, j = U, V, W$, and a_{ki} is the direction cosine of the k (= X, Y, or Z) axis with respect to the i (= U, V, or W) axis. Note $a_{jl}^{-1} = a_{lj}$.

Using primes to indicate elements of the B tensor in (4.2.2) we have $\phi_{kl} \pm \phi'_{kl} = 0$, where the upper sign holds for $kl = XY$ or YZ , and the lower for $kl = XX, YY, ZZ$, and XZ . This results in six equations:

$$\phi_{XX} - \phi'_{XX} = \sum_{i,j} a_{Xi} a_{Xj} (\psi_{ij} - \psi'_{ij}) = 0 \quad (4.2.6)$$

$$\phi_{YY} - \phi'_{YY} = \sum_{i,j} a_{Yi} a_{Yj} (\psi_{ij} - \psi'_{ij}) = 0 \quad (4.2.7)$$

$$\phi_{ZZ} - \phi'_{ZZ} = \sum_{i,j} a_{Zi} a_{Zj} (\psi_{ij} - \psi'_{ij}) = 0 \quad (4.2.8)$$

$$\phi_{XZ} - \phi'_{XZ} = \sum_{i,j} a_{Xi} a_{Zj} (\psi_{ij} - \psi'_{ij}) = 0 \quad (4.2.9)$$

$$\phi_{XY} + \phi'_{XY} = \sum_{i,j} a_{Xi} a_{Yj} (\psi_{ij} + \psi'_{ij}) = 0 \quad (4.2.10)$$

$$\phi_{YZ} + \phi'_{YZ} = \sum_{i,j} a_{Yi} a_{Zj} (\psi_{ij} + \psi'_{ij}) = 0 \quad (4.2.11)$$

Equations (4.2.10) and (4.2.11) can be solved for $(\psi_{UV} + \psi'_{UV})$ and $(\psi_{VW} + \psi'_{VW})$ which are the only unknowns appearing. Any two of the first four equations can be solved for $(\psi_{UV} - \psi'_{UV})$ and $(\psi_{VW} - \psi'_{VW})$, the only unknowns in these equations. Finally, $(\psi_{UV} + \psi'_{UV})$ and $(\psi_{UV} - \psi'_{UV})$ can be solved for ψ_{UV} and ψ'_{UV} , and likewise for ψ_{VW} and ψ'_{VW} using the other two equations.

Thus, a single rotation actually overspecifies the solution, as only four of the six equations are required. The only disadvantage is that less information about alignment accuracy is provided. Misalignment will cause the solution to depend on which four of the six equations are chosen.

As an example, calling Anderssen's [1] third rotation a V-axis rotation, the following tensor results:

$$\begin{pmatrix} \frac{-322.4}{1307.3} & \frac{\psi_{UV}}{\psi'_{UV}} & \frac{-199.3}{-997.0} \\ \frac{\psi_{UV}}{\psi'_{UV}} & \frac{1540.0}{-400.0} & \frac{\psi_{VW}}{\psi'_{VW}} \\ \frac{-199.3}{-997.0} & \frac{\psi_{VW}}{\psi'_{VW}} & \frac{-1217.6}{-907.3} \end{pmatrix} \quad (4.2.12)$$

Here the U, V, W axes have been chosen such that the direction cosines of X, Y, Z with respect to U, V, W are

$$(a_{ij}) = \begin{pmatrix} .7839 & -.5313 & .3212 \\ .6208 & .6709 & -.4056 \\ 0 & .5173 & .8558 \end{pmatrix} \quad (4.2.13)$$

The equations (4.2.6) through (4.2.9) can be used with values from (4.2.12) and (4.2.13) to solve for $(\psi_{UV} - \psi'_{UV})$ and $(\psi_{VW} - \psi'_{VW})$. One of the first three equations is a linear combination of the other two, and therefore any two of the first three give consistent results. The values of ψ_{UV} , ψ'_{UV} , ψ_{VW} , and ψ'_{VW} are listed in Table 1 together with the equations used in obtaining the values.

Table 1. Values of the unknown EFG tensor elements calculated using the equations listed together with Eqs. (4.2.10) and (4.2.11).

Solution number	Equations used	ψ_{UV}	ψ'_{UV}	ψ_{VW}	ψ'_{VW}
I	(4.1.6, 7, 8)	-247	-281	-615	-286
II	(4.1.6, 9)	-258	-269	-587	-314
III	(4.1.7, 9)	107	-634	-74	-827
IV	(4.1.8, 9)	-278	-249	-615	-236

The values in the table were calculated by transforming from the U, V, W frame to the X, Y, Z frame, using only the symmetry properties of the tensor in the latter frame. The actual transformations can now be performed using Table 1 values in tensors (4.2.12) and (4.2.13).

The following four tensors result, corresponding to the four sets of values in Table 1:

$$\text{I} \begin{pmatrix} 426 & \mp 837 & \frac{-814}{-840} \\ \mp 837 & 598 & \pm 548 \\ \frac{-814}{-840} & \pm 548 & -1024 \end{pmatrix} \quad (4.2.14)$$

$$\text{II} \begin{pmatrix} 426 & \mp 827 & -827 \\ \mp 827 & \frac{573}{623} & \pm 554 \\ -827 & \pm 554 & \frac{-999}{-1049} \end{pmatrix} \quad (4.2.15)$$

$$\text{III} \begin{pmatrix} \frac{-53}{906} & \mp 534 & -827 \\ \mp 534 & 598 & \pm 859 \\ -827 & \pm 859 & \frac{-545}{-1504} \end{pmatrix} \quad (4.2.16)$$

$$\text{IV} \begin{pmatrix} \frac{452}{400} & \mp 843 & -827 \\ \mp 843 & \frac{572}{624} & \pm 538 \\ -827 & \pm 538 & -1024 \end{pmatrix} \quad (4.2.17)$$

It is noted that if averages are taken where the A and B site elements differ, all the diagonal elements and the X, Z off-diagonal elements are consistent among all four tensors. Furthermore, it seems clear that (4.2.16) should be disregarded. The spread in values in (4.2.16) arises from division by the difference of two nearly equal numbers. Tensor (4.2.14) is the most consistent and the X, Y and Y, Z

elements fall between corresponding values in (4.2.15) and (4.2.17).

Therefore, the complete tensor would be

$$\begin{pmatrix} 426 & \mp 837 & -827 \\ \mp 837 & 598 & \pm 548 \\ -827 & \pm 548 & -1024 \end{pmatrix} \quad (4.2.18)$$

using only the third rotation reported by Andersson [1].

According to (4.2.18) a Z-axis rotation should give

$$(2\Delta\nu)_Z = 512 + 841\cos 2(\theta_Z \mp 47.9^\circ) \quad , \quad (4.2.19)$$

whereas Andersson [1] reported

$$(2\Delta\nu)_Z = 395 + 870\cos 2(\theta_Z \mp 39^\circ) \quad . \quad (4.2.20)$$

The differences are probably due to uncertainty in orientation of the axes which Andersson et al. [1] suggested may have accounted for the discrepancies they observed.

Using two or three rotation patterns to solve the problem would result in even greater overspecification, and make the problem of deciding which equations to use even more difficult.

4.3 Data

In the present experiment, two rotation patterns were obtained at about 5° C and one pattern each at 74° C, 148° C, and 167° C.

The c axis was chosen for the first series for several reasons. First, cleavage along the (010) and (0 $\bar{1}$ 0) planes results in a roughly hexagonal crystal, facilitating shaping and aligning the crystal. Next, Andersson et al. [1] had performed a c-axis rotation, so there was a reference to use in initially obtaining a nitrogen resonance in glycine, and a direct comparison could be made with that work. Finally, it was

not realized at the time that a single rotation would suffice if the axis were not in the a, c plane or normal to it.

The first rotation pattern, Fig. 19, produced results deceptively close to those reported by Andersson et al. [1]. It was thought that the alignment was quite good and that only a part of the rotation pattern would be required, making use of symmetry to obtain all four complete curves.

The signal was extremely weak, and results shown in Fig. 19 were the first obtained after many fruitless efforts. With all equipment finally working, emphasis was on taking data, leaving the detailed analysis until later. Therefore, it was not recognized at the time that the curves were not quite symmetric.

A second rotation pattern, Fig. 20, was obtained at 74° C, which appeared to have a reduced offset and amplitude.

The third pattern, Fig. 21, was extremely difficult, both electronically and mechanically, as the goniometer would not turn at this temperature. Some resonances could not be found where expected and sometimes doubtful signals were recorded if they appeared near the expected frequency. An effort was made to define one of the four curves quite accurately and rely on a few points and symmetry for the others.

The data showed none of the behavior reported by Blinc et al. [2] with regard to the shift in the principal axis direction. A reduction in the quadrupole coupling constant appeared to be the major change. Therefore, one more run was attempted at 167° C with understandably greater difficulty. This run continued until hot gas from the gas-flow temperature system melted the insulation in the rf coaxial cable, causing it to short. Enough data were obtained to plot some of the curves,

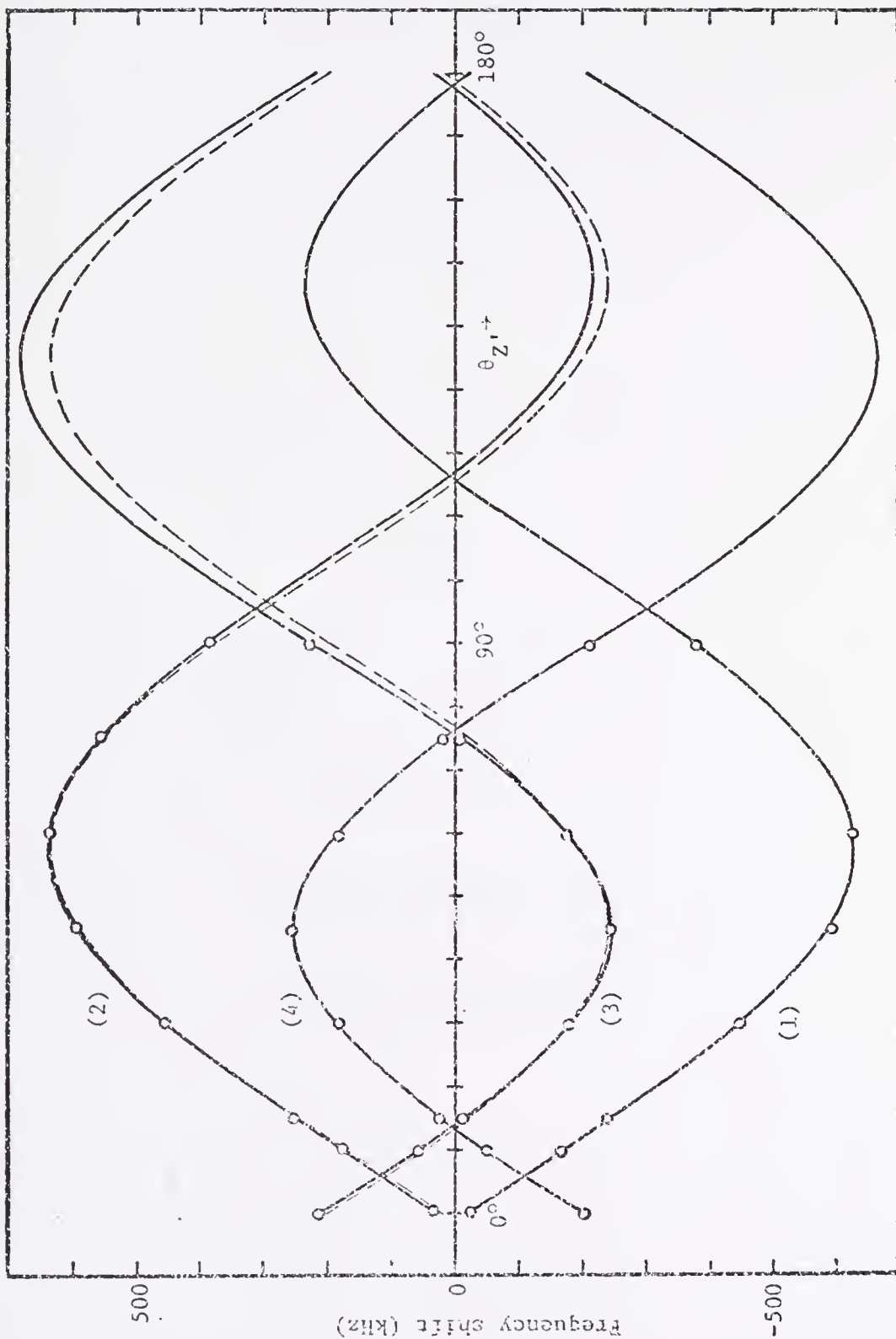


Figure 19. C-axis rotation patterns from ^{14}N in α glycine at 5°C . Pairs (1),(2) and (3),(4) are from sites B and A, respectively. $\theta_Z = 0^\circ$ at $\theta_Z \approx 96^\circ$. Dashed curves are from Andersson et al. [1].

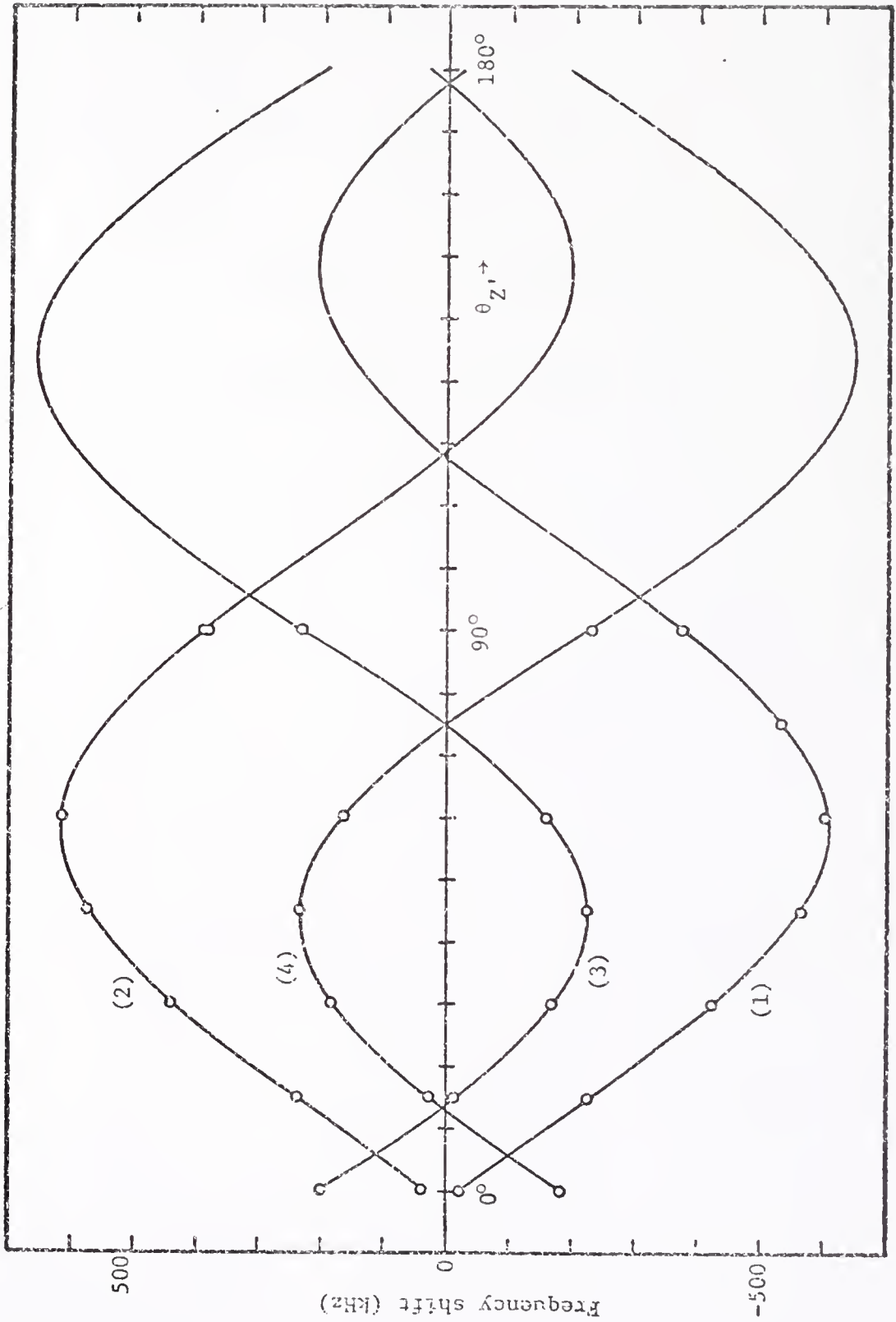


Figure 20. C-axis rotation patterns from ^{14}N in α glycine at 74°C . Pairs (1), (2) and (3), (4) are from sites B and A, respectively. $\theta_z = 0^\circ$ at $\theta_z, \approx 96^\circ$.

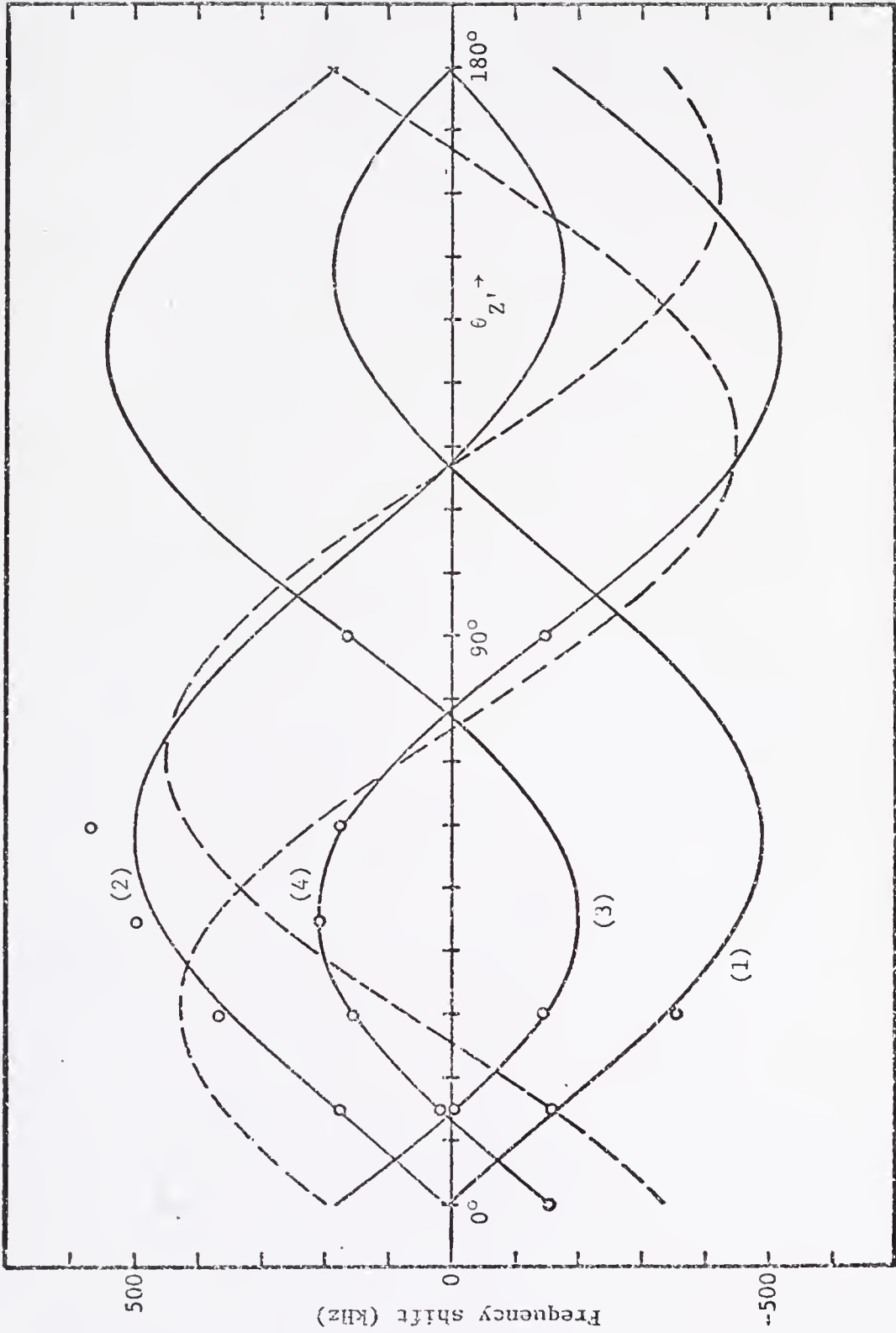
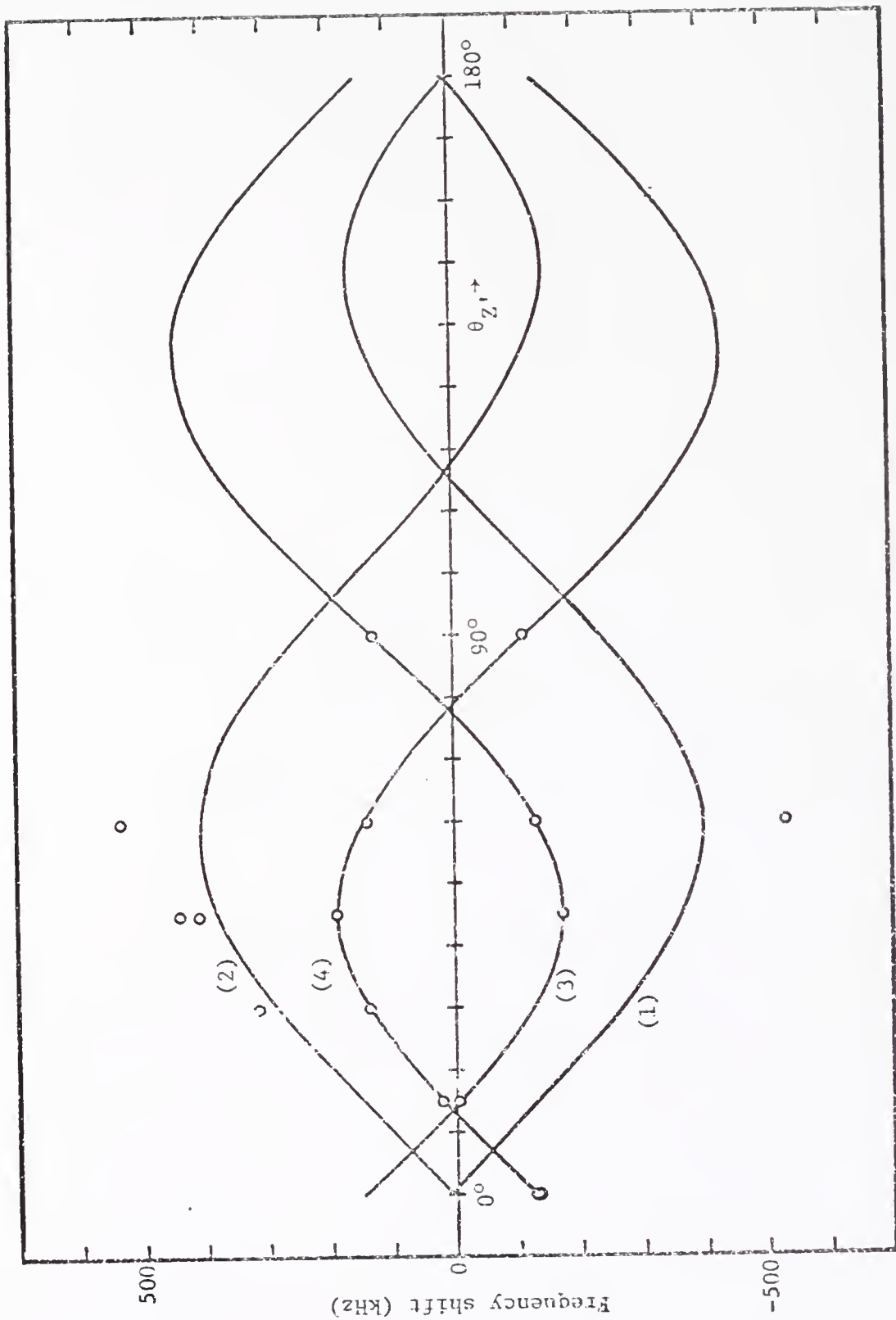
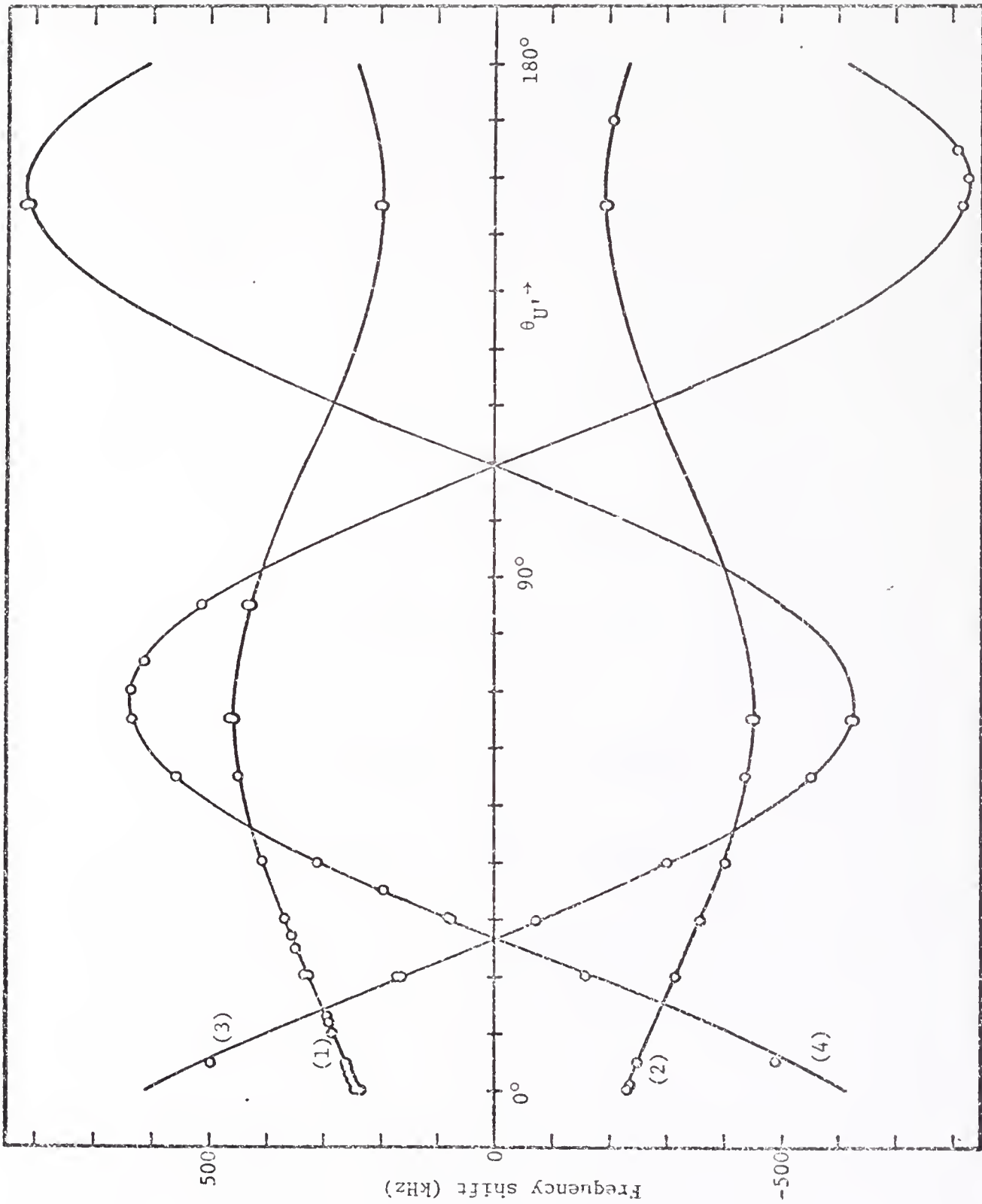


Figure 21. C-axis rotation patterns from ^{14}N in α glycine at 148°C . Pairs (1), (2) and (3), (4) are from sites B and A, respectively. $\theta_z = 0^\circ$ at $\theta_{z'}$ & 96° . Dashed curves are from Blinc et al. [2] and show no relation to the present data.



Figure, 22. C-axis rotation patterns from ^{14}N in α glycine at 167°C . Pairs (1), (2) and (3), (4) are from sites B and A, respectively. $\theta_{z,0} = 0^\circ$ at $\theta_z \approx 96^\circ$.

Figure 23. Rotation patterns from ^{14}N in α glycine at 5° C using axis normal to (120) plane. Pairs (1), (2) and (3), (4) are from sites B and A, respectively. $\theta_U = 0^\circ$ at $\theta_U \approx 1.25^\circ$. U, V, W axes are defined in Fig. 24.



so no more c-axis rotation measurements were attempted. Data are shown in Fig. 22.

After a design change to withstand the higher temperature, a second crystal was inserted, mounted with the rotation axis normal to the (120) crystal plane. The signal was weaker than during the previous runs, possibly due to the change in design of the equipment or to the quality of the crystal. Use of Fast Fourier Transform (FFT) techniques aided, but the only rotation pattern obtained was at 5° C, shown in Fig. 23. Each suspected data point had to be repeated several times for verification, and small angular rotations were used initially until the trend of the curves was established.

The signal could not be distinguished at even moderately higher temperatures, and the experiment was terminated. The c-axis rotation patterns demonstrated normal temperature dependence and did not confirm the change in the orientation of the PA frame reported by Blinc et al. [2].

Figures 19 through 23 show all the data together with smooth curves calculated by a least squares fit, except for some of the curves in Figs. 21 and 22. Curves (3) and (4) in those two figures were determined quite accurately, but the few data points thought to lie on curves (1) and (2) turned out to be unreliable. No consistent set of curves could be found utilizing all data points, and use of all data caused a very poor fit to curves (3) and (4). Therefore only the latter two curves were considered. Curves (1) and (2) were estimated from curves (3) and (4) and the known symmetry.

4.4 Data Analysis

The data were first put in the form used by Volkoff et al. [9], which required a 96° phase change in the rotational orientation as well as combining pairs of curves to give the total splitting rather than the shift from the central unperturbed Zeeman frequency. The c-axis rotations became

$$T = 5^\circ \text{ C: } (2\Delta\nu)_Z^A = 428 + 917\cos 2(\theta_Z - 38.8^\circ)$$

$$(2\Delta\nu)_Z^B = 407 + 855\cos 2(\theta_Z + 38.8^\circ)$$

$$T = 74^\circ \text{ C: } (2\Delta\nu)_Z^A = 424 + 882\cos 2(\theta_Z - 38.8^\circ)$$

$$(2\Delta\nu)_Z^B = 408 + 812\cos 2(\theta_Z + 38.8^\circ)$$

$$T = 148^\circ \text{ C: } (2\Delta\nu)_Z^A = 325 + 734\cos 2(\theta_Z - 38.8^\circ)$$

$$(2\Delta\nu)_Z^B = 312 + 676\cos 2(\theta_Z + 38.8^\circ)$$

$$T = 167^\circ \text{ C: } (2\Delta\nu)_Z^A = 261 + 614\cos 2(\theta_Z - 38.8^\circ)$$

$$(2\Delta\nu)_Z^B = 244 + 558\cos 2(\theta_Z + 38.8^\circ) \quad . \quad (4.4.1)$$

Equations (4.4.1) should have the same constants for the A and B sites if the axis were exactly in the a, c plane, so an average is taken for each temperature. The equations become

$$T = 5^\circ \text{ C: } (2\Delta\nu)_Z = 417.5 + 886.0\cos 2(\theta_Z \mp 38.8^\circ)$$

$$T = 74^\circ \text{ C: } (2\Delta\nu)_Z = 416.0 + 847.0\cos 2(\theta_Z \mp 38.8^\circ)$$

$$T = 148^\circ \text{ C: } (2\Delta\nu)_Z = 318.5 + 705.0\cos 2(\theta_Z \mp 38.8^\circ)$$

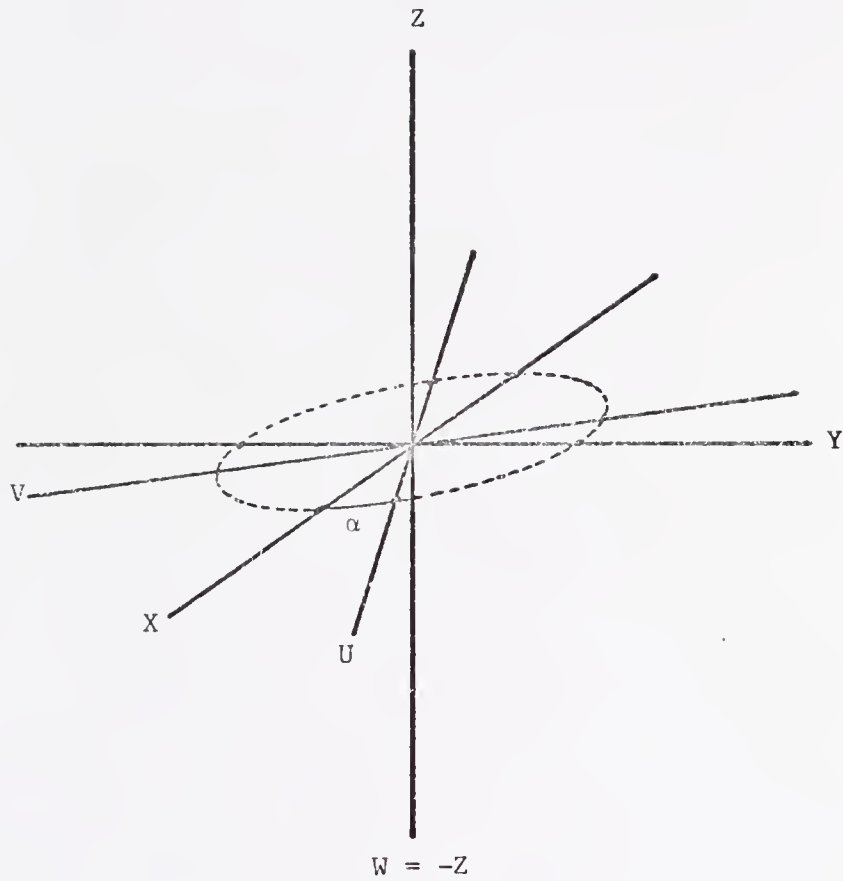


Figure 24. Relationship of U, V, W axes to X, Y, Z axes. The U axis is normal to the (120) plane and $\alpha = 38.378^\circ$.

$$T = 167^\circ \text{ C: } (2\Delta\nu)_Z = 252.5 + 586.0\cos 2(\theta_Z \mp 38.8^\circ) \quad (4.4.2)$$

where the upper (lower) sign pertains to site A (B).

A Σ^U frame is used for the rotation in the (120) plane, defined by U being normal to the plane and W being antiparallel to the Z axis as shown in Fig. 24. The curves obtained are

$$\begin{aligned} T = 5^\circ \text{ C: } (2\Delta\nu)_U^A &= 185.2 + 1444.5\cos 2(\theta_U + 21.89^\circ) \\ (2\Delta\nu)_U^B &= -646.7 + 258.1\cos 2(\theta_U + 23.66^\circ) . \end{aligned} \quad (4.4.3)$$

The two curves should cross at $\theta_U = 90^\circ$ as \vec{H}_O would be in the a, c crystal plane and the two EFG tensors are mirror images of each other in that plane. The curves cross at $\theta_U = 91.25^\circ$, indicating a 1.25° error in rotational orientation. The equations (4.4.3) then become

$$\begin{aligned} T = 5^\circ \text{ C: } (2\Delta\nu)_U^A &= 185.2 + 1444.5\cos 2(\theta_U + 23.14^\circ) \\ (2\Delta\nu)_U^B &= -646.7 + 258.1\cos 2(\theta_U + 24.91^\circ) . \end{aligned} \quad (4.4.4)$$

Equations (4.4.2) and (4.4.4) are expanded to give

$$T = 5^\circ \text{ C: } (2\Delta\nu)_U^A = 185.2 + 998.3\cos 2\theta_U - 1044.0\sin 2\theta_U \quad (4.4.5)$$

$$(2\Delta\nu)_U^B = -646.7 + 165.5\cos 2\theta_U - 197.2\sin 2\theta_U \quad (4.4.6)$$

$$(2\Delta\nu)_Z = 417.5 + 190.3\cos 2\theta_Z \pm 865.3\sin 2\theta_Z \quad (4.4.7)$$

$$T = 74^\circ \text{ C: } (2\Delta\nu)_Z = 416.0 + 181.9\cos 2\theta_Z \pm 827.2\sin 2\theta_Z \quad (4.4.8)$$

$$T = 148^\circ \text{ C: } (2\Delta\nu)_Z = 318.5 + 151.4\cos 2\theta_Z \pm 688.6\sin 2\theta_Z \quad (4.4.9)$$

$$T = 167^\circ \text{ C: } (2\Delta\nu)_Z = 252.5 + 133.8\cos 2\theta_Z \pm 572.3\sin 2\theta_Z . \quad (4.4.10)$$

Equations (4.4.5) and (4.4.6) can be used alone or in conjunction

with (4.4.7) to solve the complete EFG tensor at $T = 5^\circ \text{ C}$. These equations lead to the following tensors in the Σ and Σ^U frames, where again the upper value or sign goes with site A and the lower value or sign with site B if they differ:

$$(\phi_{kl})_{\Sigma} = \begin{pmatrix} 607.8 & \mp 865.3 & -C_Y \\ \mp 865.3 & 227.2 & \mp C_X \\ -C_Y & \mp C_X & -835.0 \end{pmatrix}_{\Sigma} \quad (4.4.11)$$

$$(\psi_{ij})_{\Sigma^U} = \begin{pmatrix} \frac{-370.4}{1293.4} & \frac{-C_W}{-C'_W} & \frac{-C_V}{-C'_V} \\ \frac{-C_W}{-C'_W} & \frac{1183.5}{-480.2} & \frac{1044.0}{197.2} \\ \frac{-C_V}{-C'_V} & \frac{1044.0}{197.2} & \frac{-813.1}{-813.2} \end{pmatrix}_{\Sigma^U} \quad (4.4.12)$$

In (4.4.11) use has been made of the relations $C_Y = C'_Y$ and $C_X = -C'_X$, the primes again indicating the B site.

The direction cosines of $\Sigma = X, Y, Z$ with respect to $\Sigma = U, V, W$ are

$$(a_{ki}) = \begin{pmatrix} \cos\alpha & \sin\alpha & 0 \\ \sin\alpha & -\cos\alpha & 0 \\ 0 & 0 & -1 \end{pmatrix} = (a_{ik}^{-1}) \quad (4.4.13)$$

where $\alpha = 38.378^\circ$ as in Fig. 24. The tensors (4.4.11) and (4.4.12) are related by

$$\phi_{kl} = \sum_{i,j} a_{ki} \psi_{ij} a_{jl}^{-1} = \sum_{i,j} a_{ki} a_{lk} \psi_{ij} \quad (4.4.14)$$

Again recalling the EFG tensors are symmetric, equations (4.4.14) lead to twelve equations, six for each site. The set of six representing site A is

$$\phi_{XX} = \psi_{UU} \cos^2 \alpha + 2\psi_{UV} \sin \alpha \cos \alpha + \psi_{VV} \sin^2 \alpha \quad (4.4.15)$$

$$\phi_{YY} = \psi_{UU} \sin^2 \alpha - 2\psi_{UV} \sin \alpha \cos \alpha + \psi_{VV} \cos^2 \alpha \quad (4.4.16)$$

$$\phi_{ZZ} = \psi_{WW} \quad (4.4.17)$$

$$\phi_{XZ} = \psi_{ZX} = -\psi_{UW} \cos \alpha - \psi_{VW} \sin \alpha \quad (4.4.18)$$

$$\phi_{XY} = \psi_{YX} = (\psi_{UU} - \psi_{VV}) \sin \alpha \cos \alpha + \psi_{UV} (\sin^2 \alpha - \cos^2 \alpha) \quad (4.4.19)$$

$$\phi_{YZ} = \psi_{ZY} = -\psi_{UW} \sin \alpha + \psi_{VW} \cos \alpha \quad (4.4.20)$$

Adding primes to the ϕ 's and ψ 's would result in the equations for the B site.

The solution may be obtained from the single U rotation by making use of the symmetry of (4.4.11). Six equations result:

$$\phi_{XX} - \phi'_{XX} = (\psi_{UU} - \psi'_{UU}) \cos^2 \alpha + 2(\psi_{UV} - \psi'_{UV}) \sin \alpha \cos \alpha + (\psi_{VV} - \psi'_{VV}) \sin^2 \alpha = 0 \quad (4.4.21)$$

$$\phi_{YY} - \phi'_{YY} = (\psi_{UU} - \psi'_{UU}) \sin^2 \alpha - 2(\psi_{UV} - \psi'_{UV}) \sin \alpha \cos \alpha + (\psi_{VV} - \psi'_{VV}) \cos^2 \alpha = 0 \quad (4.4.22)$$

$$\phi_{ZZ} - \phi'_{ZZ} = \psi_{WW} - \psi'_{WW} = 0 \quad (4.4.23)$$

$$\phi_{XZ} - \phi'_{XZ} = -(\psi_{UW} - \psi'_{UW}) \cos \alpha - (\psi_{VW} - \psi'_{VW}) \sin \alpha = 0 \quad (4.4.24)$$

$$\phi_{XY} + \phi'_{XY} = (\psi_{UU} + \psi'_{UU} - \psi_{VV} - \psi'_{VV}) \sin \alpha \cos \alpha + (\psi_{UV} + \psi'_{UV}) (\sin^2 \alpha - \cos^2 \alpha) = 0 \quad (4.4.25)$$

$$\phi_{YZ} + \phi'_{YZ} = -(\psi_{UW} + \psi'_{UW}) \sin \alpha + (\psi_{VW} + \psi'_{VW}) \cos \alpha = 0 \quad (4.4.26)$$

The small correction for rotational orientation made in equation (4.4.4) assured equation (4.4.23) would be very nearly true, which in turn caused (4.4.21) and (4.4.22) to be consistent. Because of the choice of axes, $(\psi_{UV} - \psi'_{UV})$ appears only in (4.4.21) and (4.4.22) and

either equation can be used to evaluate it without ambiguity. Also due to the choice of axes, $(\psi_{UW} - \psi'_{UW})$ appears only in (4.4.24), resulting in a single value. The quantities $(\psi_{UV} + \psi'_{UV})$ and $(\psi_{UW} + \psi'_{UW})$ appear in (4.4.25) and (4.4.26) respectively, making their evaluation simple. Even with a different choice of axes, the latter two quantities would be unambiguous.

Inserting values from (4.4.12) and recalling $\alpha = 38.378^\circ$, the unknowns in (4.4.12) are

$$\begin{aligned} C_W &= -\psi_{UV} = -429.1 \\ C'_W &= -\psi'_{UV} = -37.5 \\ C_V &= -\psi_{UW} = -448.3 \\ C'_V &= -\psi'_{UW} = -1118.9 \quad , \end{aligned} \tag{4.4.27}$$

and (4.4.12) becomes

$$(\psi_{ij})_{\Sigma^U} = \begin{pmatrix} \frac{-370.4}{1293.4} & \frac{429.1}{37.5} & \frac{448.3}{1118.9} \\ \frac{429.1}{37.5} & \frac{1183.5}{-480.2} & \frac{1044.0}{197.2} \\ \frac{448.3}{1118.9} & \frac{1044.0}{197.2} & \frac{-813.1}{-813.2} \end{pmatrix}_{\Sigma^U} \text{ (From U rotation)} \tag{4.4.28}$$

The transformation to the Σ frame (4.4.14) can now be performed, resulting in

$$(\phi_{kl})_{\Sigma} = \begin{pmatrix} 646.3 & \mp 854.6 & -999.6 \\ \mp 854.6 & 166.9 & \pm 540.1 \\ -999.6 & \pm 540 & -813.2 \end{pmatrix}_{\Sigma} \text{ (From U rotation)} \tag{4.4.29}$$

which should be compared with

$$(\phi_{kl})_{\Sigma} = \begin{pmatrix} 607.8 & \mp 365.3 & -C_Y \\ \mp 365.3 & 227.2 & \mp C_X \\ -C_Y & \mp C_X & -835.0 \end{pmatrix}_{\Sigma} \begin{matrix} \\ \\ \text{(From Z} \\ \text{rotation)} \end{matrix} \quad (4.4.11)$$

The differences are probably due to small errors in crystal orientation.

In order to solve the problem using both rotations rather than known symmetry, values of ϕ_{XX} , ϕ_{YY} , ϕ_{ZZ} and ϕ_{XY} from (4.4.11) are put in equations (4.4.15) through (4.4.20), together with known values of ψ 's from (4.4.12). Equations (4.4.15), (4.4.16), and (4.4.19) each contain only one unknown, ψ_{UV} or ψ'_{UV} for site A or B, respectively, which are found to be

$$\begin{aligned} \psi_{UV} &= 389.6, 475.6, 367.2 \\ \psi'_{UV} &= -2.0, -9.1, -24.4 \end{aligned} \quad (4.4.30)$$

depending on which of the three equations is used. There is now considerable variation, due again to orientation errors, but the averages,

$$\psi_{UV} = 410.8, \quad \psi'_{UV} = -11.8 \quad (4.4.31)$$

agree within reason with the values 429.1 and 37.5, respectively, found from the single rotation.

The four equations (4.4.18), (4.4.20) and the corresponding equations for site B have six unknowns, and cannot be solved. Therefore, two more relations, $\phi_{XZ} = \phi'_{XZ}$ and $\phi_{YZ} = -\phi'_{YZ}$ must be used. This has already been done in solving the problem from the single U rotation, and the values can be taken from (4.4.28) and (4.4.29).

The resulting two tensors are

$$(\psi_{ij})_{\Sigma^U} = \begin{pmatrix} \frac{-370.4}{1293.4} & \frac{410.8}{-11.8} & \frac{448.3}{1118.9} \\ \frac{410.8}{-11.8} & \frac{1183.5}{-480.2} & \frac{1044.0}{197.2} \\ \frac{448.3}{1118.9} & \frac{1044.0}{197.2} & \frac{-813.1}{-813.2} \end{pmatrix}_{\Sigma^U} \quad \text{(From both rotations)} \quad (4.4.32)$$

and

$$(\phi_{kl})_{\Sigma} = \begin{pmatrix} 607.8 & \mp 865.3 & -999.6 \\ \mp 865.3 & 227.2 & \pm 540.1 \\ -999.6 & \pm 540.1 & -835.0 \end{pmatrix}_{\Sigma} \quad \text{(From both rotations)} \quad (4.4.33)$$

In order to illustrate the effect of small alignment errors, the tensors (4.4.29) may be transformed to a set of axes $\Sigma'' = X'', Y'', Z''$ such that X'' and Z'' are out of the a, c plane 0.5° and therefore Y'' is 0.707° from the b axis. The resulting tensors are

$$\begin{pmatrix} \frac{631}{661} & \frac{-867}{841} & \frac{-987}{-1012} \\ \frac{-867}{841} & \frac{191}{143} & \frac{540}{-540} \\ \frac{-987}{-1012} & \frac{540}{-540} & \frac{-823}{-804} \end{pmatrix} \quad (4.4.34)$$

The order of magnitudes of the shifts caused by such a small orientation error in comparison with the differences between (4.4.29) and (4.4.33) indicates a cumulative alignment error on the order of 1° in obtaining the desired rotation axes.

Following the method of Volkoff et al. [9], the tensors (4.4.29) and (4.4.33) may be diagonalized to obtain $e^2 qQ/h, \eta$, and the direction cosines of the principal axes. These results are displayed followed by those of Andersson et al. [1] and Blinc et al. [2] for comparison. Andersson's group worked at a few degrees higher temperature than the present work but the temperature dependence is very small over this

interval, and may be ignored.

Blinic's group worked at a significantly higher temperature, but their results are included for comparison.

The tensors (4.4.29) from the single U rotation result in

$$\eta = .492, \quad e^2_{qQ}/h = 1188 \text{ kHz} \quad (4.4.35)$$

$$(a_{ij}) = \begin{pmatrix} .513 & \pm .844 & -.158 \\ .420 & \mp .086 & .904 \\ \pm .749 & -.529 & \mp .399 \end{pmatrix} \quad (4.4.36)$$

at T = 5° C.

The tensors (4.4.33) from the Z rotation with two elements obtained from the U rotation results in

$$\eta = .517, \quad e^2_{qQ}/h = 1189 \text{ kHz} \quad (4.4.37)$$

$$(a_{ij}) = \begin{pmatrix} .523 & \pm .834 & -.179 \\ .427 & \mp .074 & .901 \\ \pm .738 & -.547 & \mp .395 \end{pmatrix} \quad (4.4.38)$$

at T = 5° C.

Andersson et al. [1] reported

$$\eta = .5 \pm .1, \quad e^2_{qQ}/h = 1200 \pm 100 \text{ kHz} \quad (4.4.39)$$

$$(a_{ij}) = \begin{pmatrix} .53 & \pm .85 & -.17 \\ .43 & \mp .08 & .90 \\ \pm .74 & -.54 & \mp .40 \end{pmatrix} \quad (4.4.40)$$

at room temperature.

Blinic's published EFG tensor can be used to find the direction cosines of the principal axes in the X, Y, Z frame, and his results are [2]

$$\eta = 0.61 \pm 0.03, \quad e^2_{qQ}/h = 745 \pm 20 \text{ kHz} \quad (4.4.41)$$

$$(a_{ij}) = \begin{pmatrix} .216 & \pm.391 & -.895 \\ .902 & \mp.430 & .030 \\ \mp.373 & -.814 & \mp.446 \end{pmatrix} \quad (4.4.42)$$

at $T = 140^\circ \text{ C}$.

Edmonds and Speight [3] reported

$$\eta = 0.51, \quad e^2_{qQ}/h = 1250 \text{ kHz} \quad (4.4.43)$$

at $T = 77 \text{ K}$.

At higher temperatures, only incomplete EFG tensors could be obtained, calculated from equations (4.4.8), (4.4.9), and (4.4.10). They are

$$T = 74^\circ \text{ C}: \quad (\phi_{kl})_\Sigma = \begin{pmatrix} 598 & \mp 827 & -C_Y \\ \mp 827 & 234 & \mp C_X \\ -C_Y & \mp C_X & -832 \end{pmatrix} \quad (4.4.44)$$

$$T = 148^\circ \text{ C}: \quad (\phi_{kl})_\Sigma = \begin{pmatrix} 470 & \mp 689 & -C_Y \\ \mp 689 & 167 & \mp C_X \\ -C_Y & \mp C_X & -637 \end{pmatrix} \quad (4.4.45)$$

$$T = 167^\circ \text{ C}: \quad (\phi_{kl})_\Sigma = \begin{pmatrix} 378 & \mp 572 & -C_Y \\ \mp 572 & 127 & \mp C_X \\ -C_Y & \mp C_X & -505 \end{pmatrix} \quad (4.4.46)$$

If a constant asymmetry parameter and constant direction cosines are assumed, but e^2_{qQ}/h decreases with temperature to 1170, 925, and 750 kHz at $T = 74^\circ \text{ C}$, 148° C , and 167° C , respectively, the tensor (4.4.33) would become

$$T = 74^{\circ} \text{ C:} \quad (\phi_{kl})_{\Sigma} = \begin{pmatrix} 598 & \mp 851 & -984 \\ \mp 851 & 224 & \pm 532 \\ -984 & \pm 532 & -822 \end{pmatrix} \quad (4.4.47)$$

$$T = 148^{\circ} \text{ C:} \quad (\phi_{kl})_{\Sigma} = \begin{pmatrix} 473 & \mp 673 & -778 \\ \mp 673 & 177 & \pm 420 \\ -778 & \pm 420 & -650 \end{pmatrix} \quad (4.4.48)$$

$$T = 167^{\circ} \text{ C:} \quad (\phi_{kl})_{\Sigma} = \begin{pmatrix} 384 & \mp 546 & -631 \\ \mp 546 & 143 & \pm 341 \\ -631 & \pm 341 & -527 \end{pmatrix} \quad (4.4.49)$$

Finally, Blinc's EFG tensor in the X, Y, Z, frame is [2]

$$T = 140^{\circ} \text{ C:} \quad (\phi_{kl})_{\Sigma} = \begin{pmatrix} -587 & \pm 670 & 203 \\ \pm 670 & 540 & \pm 492 \\ 203 & \pm 492 & 47 \end{pmatrix} \quad (4.4.50)$$

There is quite good agreement between the present results, (4.4.35) through (4.4.38), and those reported by Andersson et al. [1], (4.4.39) and (4.4.40), and by Edmonds and Speight [3], (4.4.43), even though the temperatures are different. This indicates a very weak temperature dependence over the interval from 77 K to room temperature, and confirms the orientation of the EFG principal axes to within about 1° , which is the order of the variation between (4.4.36), (4.4.38) and (4.4.40). The direction of the largest principal axis is about 7° from the direction of the C-N bond.

A comparison of the observed data at $T = 74^{\circ}$, 148° , and 167° C, (4.4.44), (4.4.45), and (4.4.46), and the results predicted by a reduced e^2qQ/h , (4.4.47), (4.4.48), and (4.4.49), indicates the major effect of

increasing the temperature is a reduction of the quadrupole coupling constant.

The orientation of the principal axes observed by Blinc (4.4.42), is completely different than the orientation reported by Andersson (4.4.20) and that found in the present work, (4.4.36), (4.4.38). The latter orientation supports a hindered rotation of the NH_3 group, and there should be no reason for it to cease or become less symmetric at higher temperatures.

While a simple reduction in e^2qQ/h at higher temperatures does not completely explain the EFG tensors found at $T = 148^\circ \text{C}$ and $T = 167^\circ \text{C}$, there is no relation between these tensors and that reported by Blinc (4.4.20).

4.5 Conclusions

We conclude that the principal axis of the EFG tensor lies about 7° from the direction of the C-N bond at room temperature and below, and that the major effect of increasing temperature is a decrease in the quadrupole coupling constant of about 37%.

The reason for the disagreement with Blinc et al. [2] is not understood. One possibility is that a different form of the crystal was inadvertently used by Blinc et al. [2]. Another is that the high field approximation is not adequate in the 4,180 G or 4,280 G fields used by Blinc. The unperturbed Zeeman frequencies, 1.286 and 1.316 MHz, are of the same order as the maximum quadrupolar splitting observed of over 1.0 MHz. Also a simple error in orienting the crystal could take place.

CHAPTER V
RESULTS AND DISCUSSION — NMR LINE SHAPE OF ^{15}N IN
 α NITROGEN WITH O_2 IMPURITY

5.1 Structure of α Nitrogen

The structure of α nitrogen, stable below 35.6 K, is cubic and contains a basis of four molecules per unit cell. A unit cell is shown in Fig. 25. The molecules are oriented parallel to the body diagonals and may or may not be displaced slightly from the centrosymmetric positions along the body diagonals, a question which has not been completely resolved to date.

The intramolecular nuclear separation is about 1.1 \AA whereas the intermolecular nearest neighbor distance is 3.57 \AA assuming the molecules are at the centrosymmetric positions, or 3.42 \AA if they are displaced 0.17 \AA [20]. Other displacements would result in different distances; however the r^{-3} factor in Eq. (2.2.3) results in the intramolecular local magnetic dipolar field being about 30 times stronger than the intermolecular local field.

The molecules undergo librational motion which causes a reduction in the amplitude of α in Eq. (2.2.14) by a factor of about 0.86 due to motional averaging [21].

The librational motion results in a quadrupolar dominated relaxation time of about 100 seconds at 4.2 K in $^{14}\text{N}_2$ [22], and a much longer relaxation time is expected in $^{15}\text{N}_2$ as the spin $\frac{1}{2}$ ^{15}N nuclei have no quadrupolar interaction. Therefore, in order to conveniently observe the

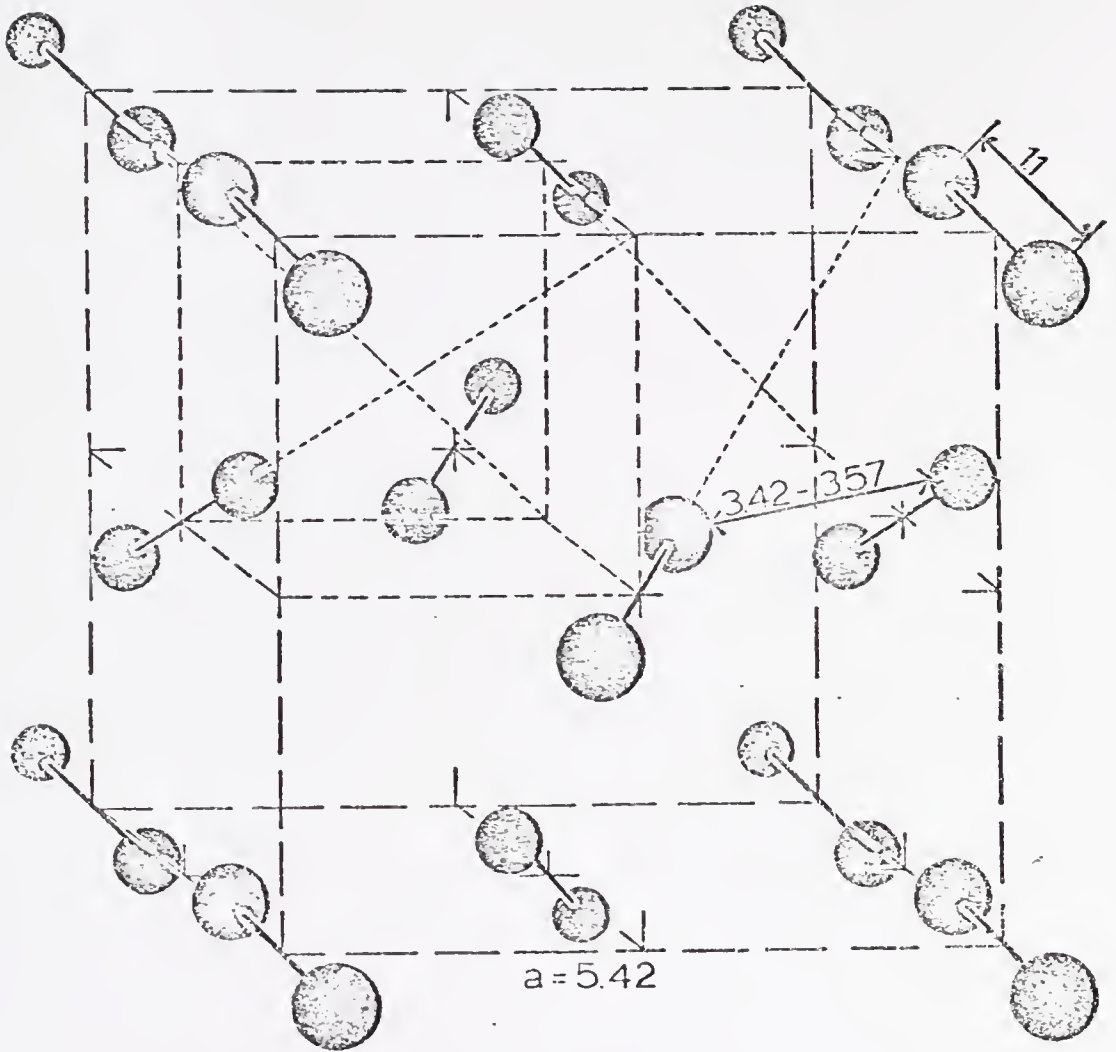


Figure 25. Unit cell of α N₂. The four basis molecules are at the corners of the small nested cube, each oriented parallel to one of the four body diagonals. Distances are in Å.

spectrum in $^{15}\text{N}_2$, paramagnetic O_2 was added to shorten the relaxation time during some runs.

5.2 Data

Using a 99.5% ^{15}N sample, with the remainder being ^{14}N , about 0.1% O_2 was added initially.

At the lowest field of 625 G, the spectrum very closely resembled a classical Pake powder pattern doublet with some asymmetry. The asymmetry increased markedly with increasing H_0 up to the limit of the magnet, 9.0 kG. The data are shown in Figs. 26 through 29.

The data at 625 G and 950 G are shown in Fig. 26. The derivative line shape as recorded by the CW spectrometer is shown as a dashed line in Fig. 26(a) with the absorption signal obtained by integration superimposed as a solid line. Figure 26(b) shows the data as a solid line superimposed on broadened and unbroadened theoretical Pake doublets from Fig. 1, which are shown by dotted and dashed lines respectively.

Examination of Fig. 26(b) can leave little doubt that the spectrum is anything but the expected Pake doublet, although the high frequency wing appears to be somewhat too close in.

Figures 27 and 28 show the effect of increasing the magnetic field H_0 . The derivative spectrum is again superimposed on the absorption spectrum at 9000 G which shows the low frequency wing, although low in amplitude, has a well-defined beginning.

The high frequency wing, which was closer in than predicted by the Pake doublet theory at 625 G, moves even closer as H_0 is increased until it cannot be distinguished above 2 kG.

Other structure is nearly masked by the basic doublet spectrum.

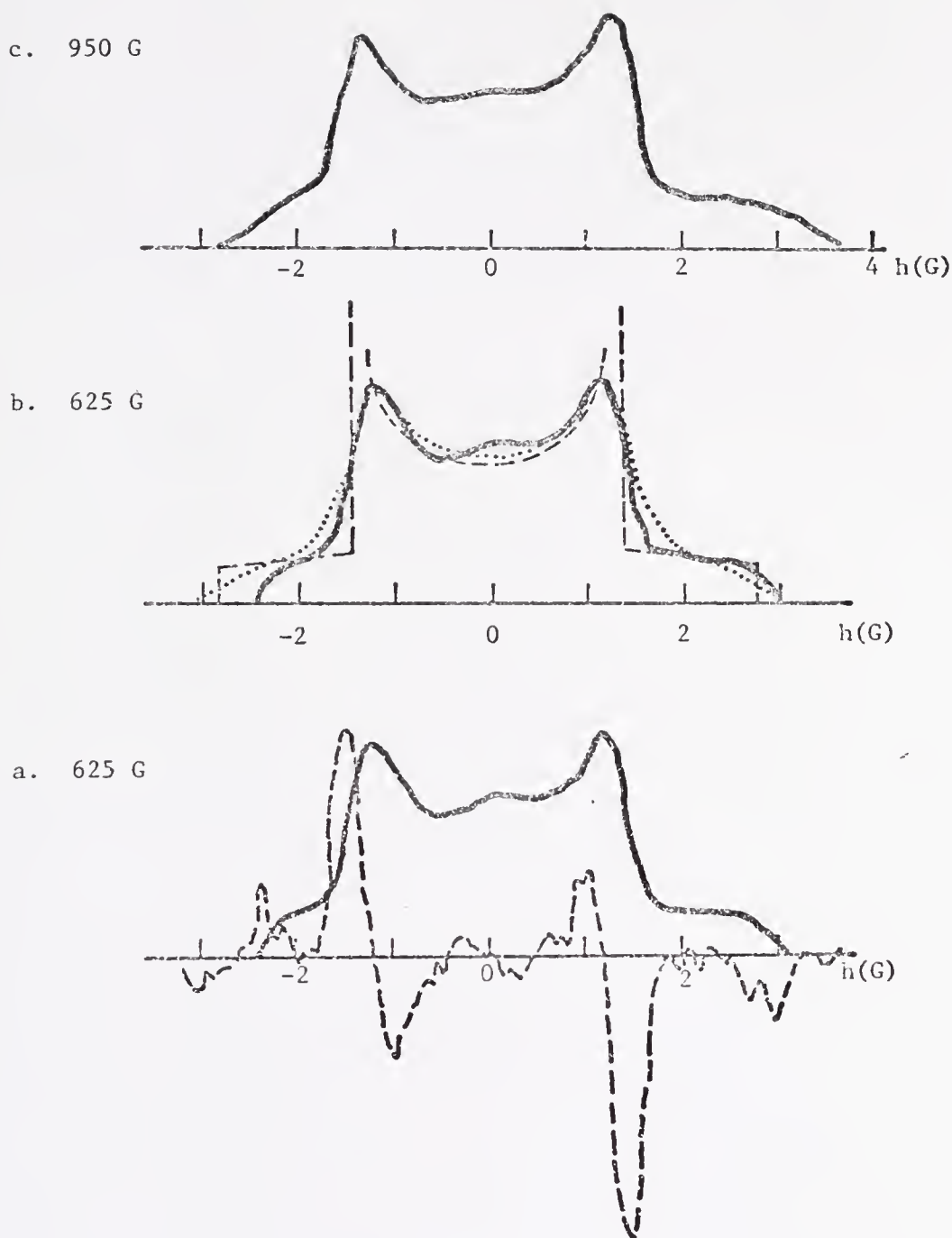


Figure 26. NMR spectrum of ^{15}N in α $^{15}\text{N}_2$ with 0.1% O_2 added at 625 and 950 G. (a) Derivative spectrum shown by dashed line at 625 G. (b) Theoretical unbroadened (---) and broadened (···) Pake doublet superimposed on data at 625 G. (c) Data at 950 G showing low frequency (high field) wing extending. Curves were obtained by sweeping H_0 , where $h = H_0 - H^* = H_0 - \omega/\gamma$ from Eq. (2.2.14).

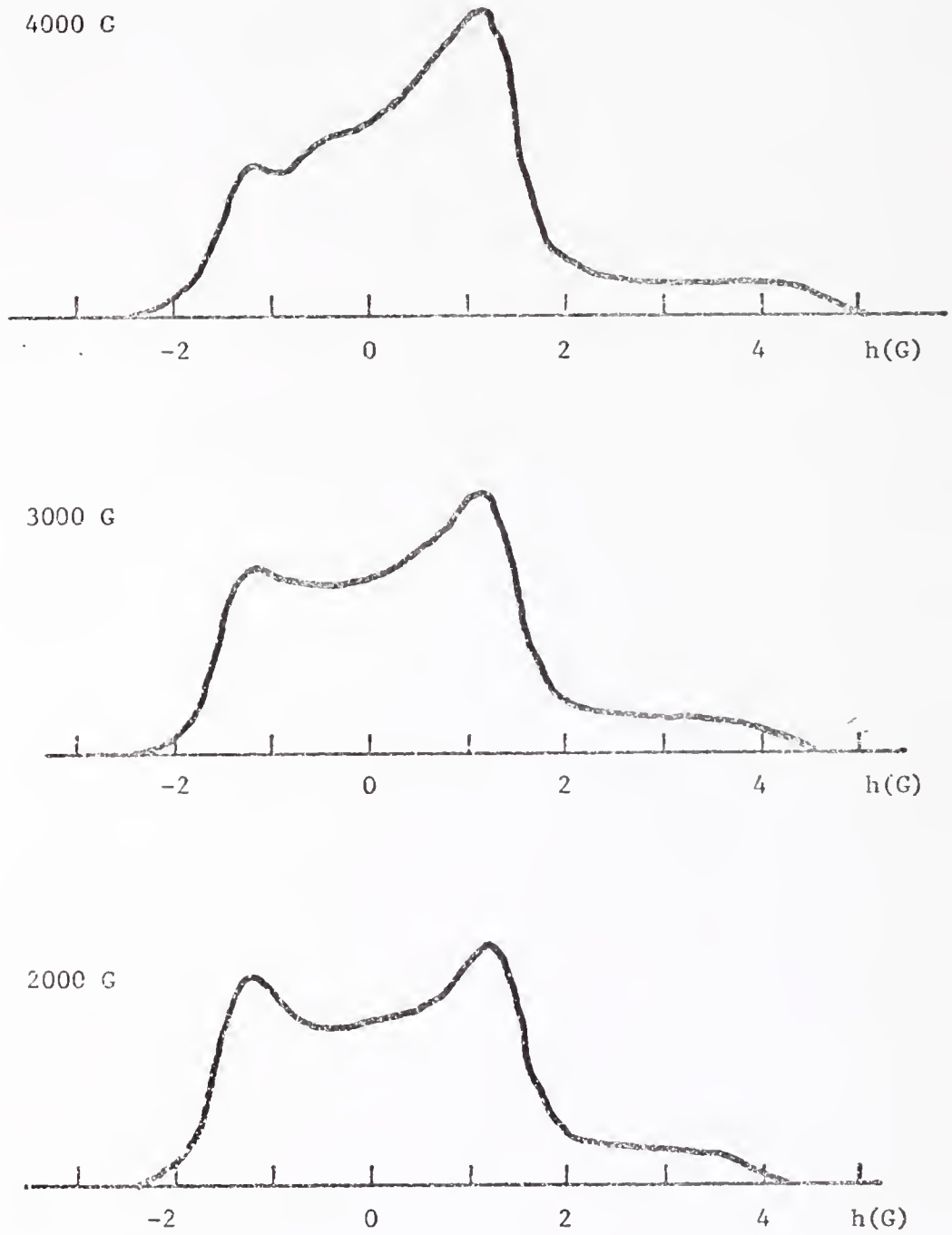


Figure 27. NMR spectrum of ^{15}N in α $^{15}\text{N}_2$ with 0.1% O_2 added at 2000, 3000, and 4000 G.

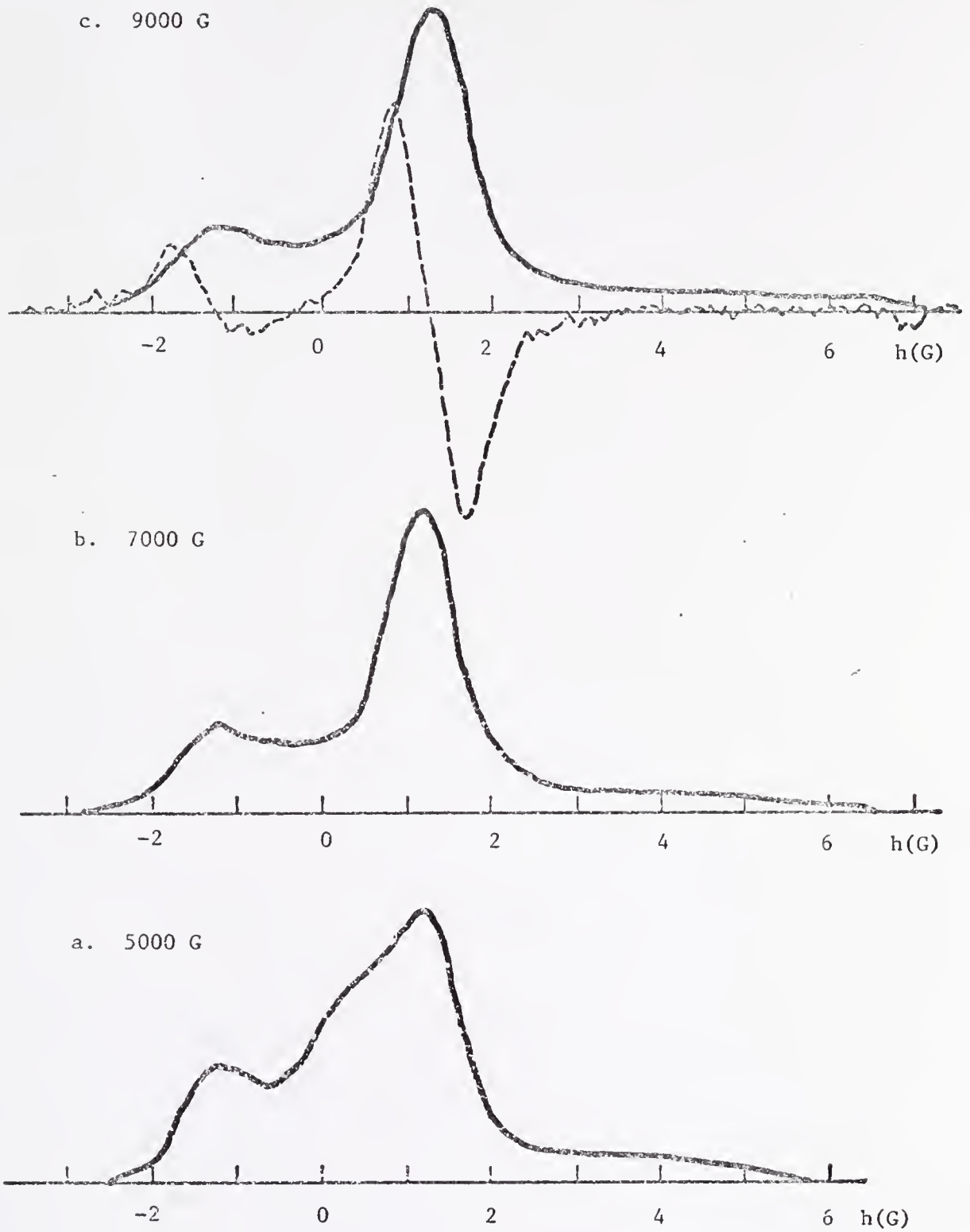


Figure 28. NMR spectrum of ^{15}N in $\alpha\text{-}^{15}\text{N}_2$ with 0.1% O_2 added at 5000, 7000, and 9000 G. (a) 5000 G. (b) 7000 G. (c) Derivative spectrum shown by dashed line at 9000 G showing low frequency wing has a well-defined beginning.

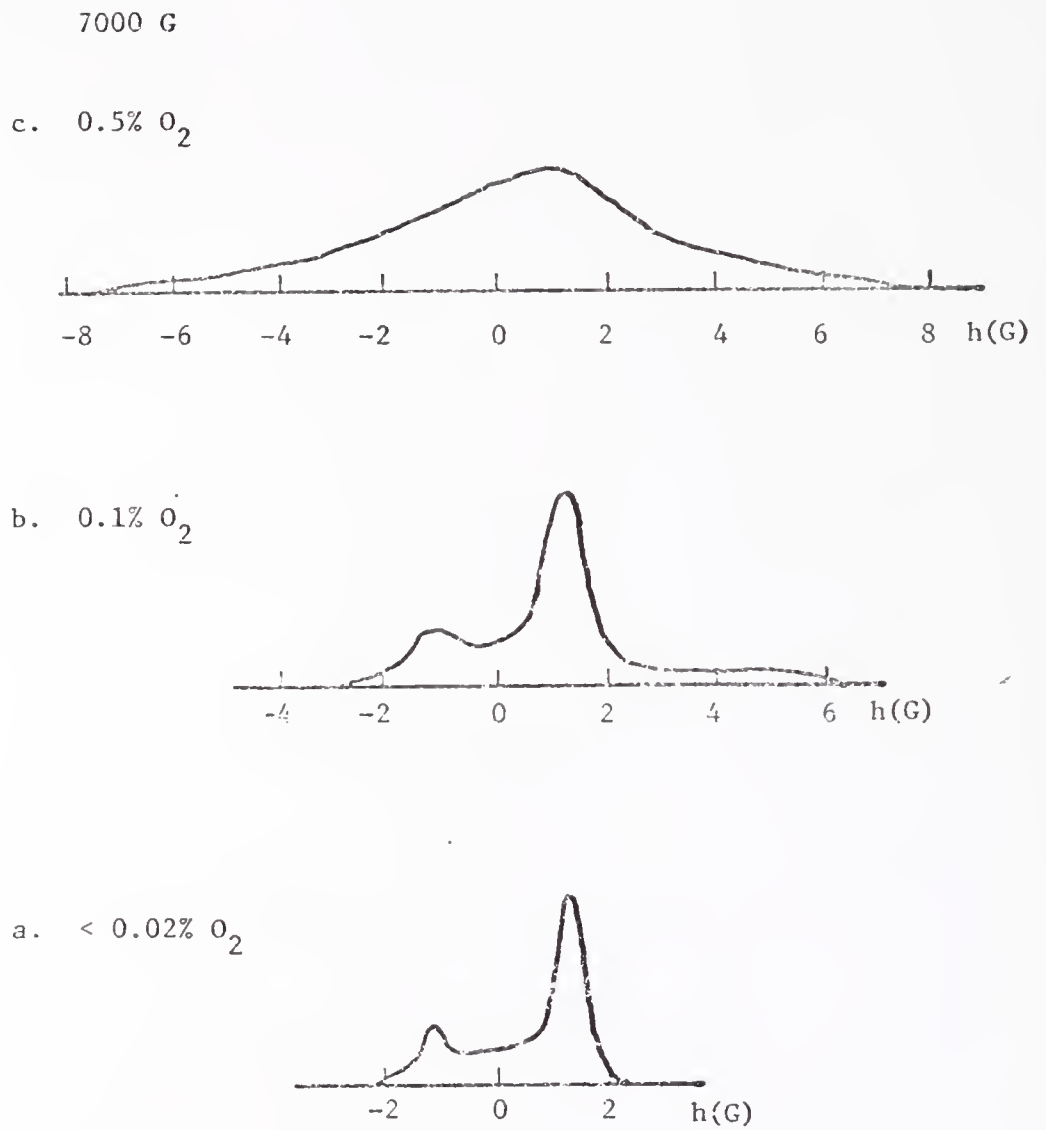


Figure 29. NMR spectrum of ¹⁵N in α ¹⁵N₂ as a function of O₂ concentration.

Thus a small hump appears between the two main peaks at low fields, but is no longer distinguishable above 5 kG. It has either lost relative intensity or is combined with the low frequency peak at high H_0 .

The peak-to-peak separation remains nearly constant, although it is a little less in medium fields than in the highest and lowest. This effect is probably due to the fact that the spectrum is a combination of a Pake doublet and a less intense spectrum. When the two peaks are added, the resultant peak lies between the two, giving the appearance of shifting the more intense peak.

The Pake doublet should be centered about the unperturbed Zeeman frequency ν_0 ; however ν_0 lies between the center and the low frequency peak, meaning the entire Pake doublet was shifted to higher frequencies by about 0.5 G or 0.25 kHz. This shift is not displayed in the data where the zero point was taken to be midway between the two peaks.

Following the experiments on the 0.1% O_2 sample the gas was passed through an Oxisorb [23] cartridge several times to remove the O_2 . As a check on the success of removal the spin-lattice relaxation time T_1 was measured at 77.4 K and compared with T_1 of high purity $^{15}N_2$ [24]. These measurements placed an upper limit of 0.02% O_2 remaining, the limit being set by the accuracy of the data. The Oxisorb specifications guarantee less than 0.1 ppm O_2 remaining for certain pressures and flow rates; however not all of the sample could be withdrawn from the outlet side of the Oxisorb unit each time. The sample was cycled repeatedly through the Oxisorb until it was calculated that less than 1 ppm O_2 remained.

Figure 29(a) is the spectrum at 7000 G and $T = 4.2$ K obtained with the O_2 removed. At 4.2 K, T_1 appeared to be on the order of seven hours,

making it very difficult to obtain a good spectrum in the presence of saturation. By leaving the magnet on continuously, one or two traces could be obtained each day, and all were reproducible to the extent that the two peaks were narrower than the corresponding data with 0.1% O₂ and the relative intensities were unchanged by the removal of the O₂. No other features could be discerned.

Figure 29(c) shows the effect of adding 0.5% O₂ where the broadening has masked any structure.

5.3 Data Analysis

In searching for an explanation of these observations, we look to the effects of the constituents of the sample other than ¹⁵N (O₂ and ¹⁴N) and to the ¹⁵N itself. The literature contains samples of spectra showing effects due to paramagnetic ions or O₂ which have a deceptive similarity to the present data [25], [26]. References [27] and [28] examine the case of ortho-para conversion in spin ½ solid H₂, and again, the resulting spectra are deceptively similar to the present data. Both of the above effects are analyzed below as is the effect of the ¹⁴N atoms which is also examined theoretically and experimentally in Chap. 6.

5.3.1. Paramagnetic O₂ Impurity

The most obvious cause of the asymmetry and other anomalous features of the line shape observed is the paramagnetic O₂. Piott and McCormick [25] have examined theoretically and experimentally the effect of O₂ impurity on the NMR line shape of protons in solid methane. They observed a central line and anomalous peaks in the wings, one of which is dominant

Broadening of the central line was attributed to protons which are second and more distant neighbors of O_2 molecules, whereas the peaks in the wings are due to first nearest neighbors.

The large central peak and the anomalous peak in the wing formed an asymmetric pair which was first compared with the asymmetric pair observed in the present data in the 4 to 7 kG range. This identification of the peaks had to be ruled out when measurements at lower fields (625 G) proved the peaks to be the expected Pake doublet peaks.

Piott and McCormick give

$$h = g\beta r^{-3} \langle S_z \rangle (1 - 3\cos^2\theta) \quad (5.3.1)$$

as the local field at a proton site due to the electron spins in a neighboring O_2 molecule. They use

$$H_e = g\beta H_o S_z + D' [S_z^2 - (1/3)S(S+1)] \quad (5.3.2)$$

as the Hamiltonian to calculate $\langle S_z \rangle$. There are 12 nearest neighbors and steric considerations limit $\langle S_z \rangle$ to three values, resulting in 36 values of h .

Using a computer, they calculated the derivative lineshape for 100 randomly oriented crystallites due to the nearest neighbors of O_2 molecules in the field produced by the C_2 molecules. A simple integration of their derivative lineshape is shown in Fig. 30 as a solid line. The dashed line qualitatively represents the location of the central peak as it cannot be accurately calculated from the data in ref. [25].

The identification of the two peaks in ref. [25] with the two in the present data has already been ruled out. There is a possibility that the present data are a superposition of a spectrum due to the nearest neighbors of O_2 molecules (hereafter referred to as the paramagnetic

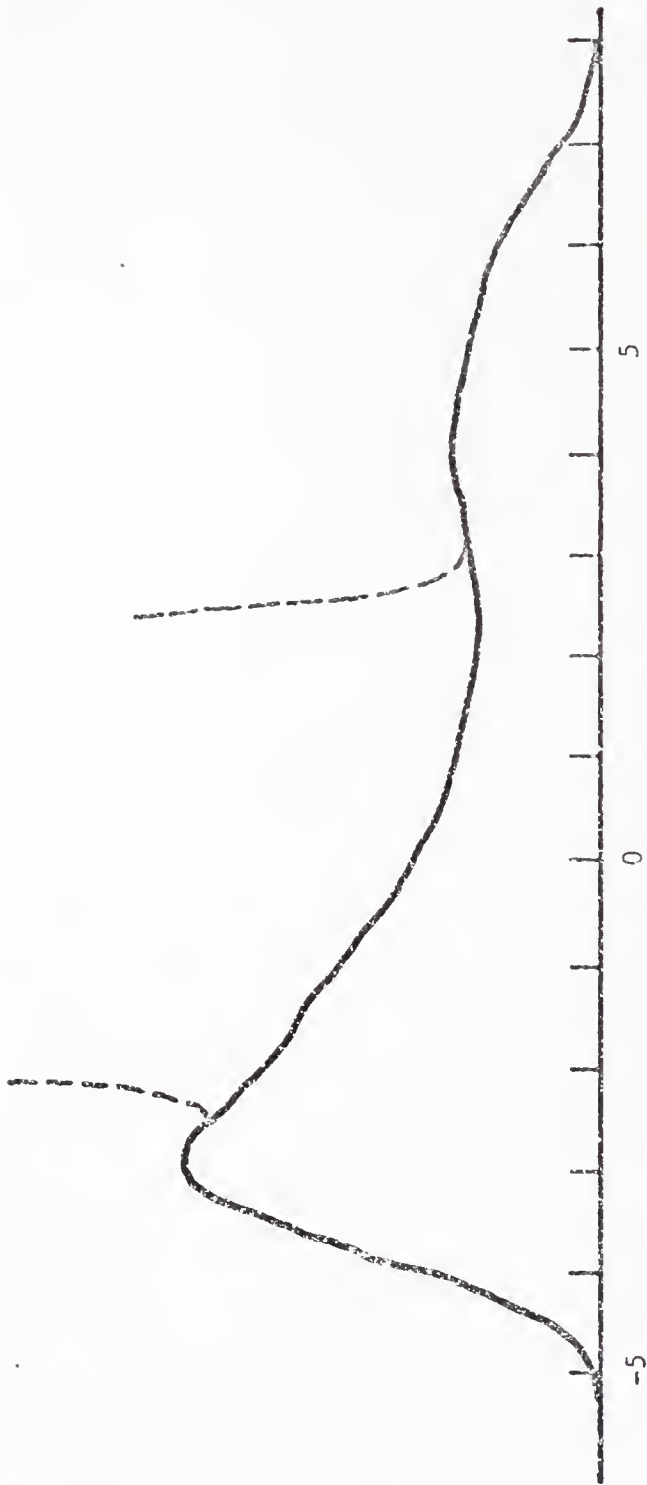


Figure 30. Calculated NMR spectrum of protons which are nearest neighbors of O₂ impurity molecules in solid methane. The solid line is an integration of the derivative spectrum in Fig. 2 of ref. [25] and the dashed line indicates the location of the central peak due to more distant neighbors of O₂ molecules. Units were not given in ref. [25].

spectrum or line shape) and the Pake doublet. Two such spectra are qualitatively indicated in Fig. 31 at $H_0 = 950$ G and $H_0 = 7000$ G.

In order to predict the behavior of the paramagnetic line shape it is easier to follow the work of Kroon [26] who examined the proton spectrum in $\text{NH}_4\text{Fe}(\text{SO}_4)_2$ experimentally and theoretically and obtained the proton spectra shown in Fig. 32. The paramagnetic Fe^{+++} ion provides the local field rather than O_2 impurity and there is no central line as all of the protons are nearest neighbors of an Fe^{+++} ion. Kroon arrived at an analytic expression for the line shape which is more convenient to use than the random crystallite calculations.

Considering that the magnetic moment of an electron is on the order of 1000 times that of a nucleus, it might be expected that the local field produced by an electron at a nearby nucleus would be as much as a kilogauss, which would spread the powder pattern spectrum over such a region as to make it unobservable. However, if the electron occupies all of its states over a time short with respect to T_1 and T_2 of the protons, an average moment must be used. The classical average is given by

$$\bar{\mu}_D = (\mu_D)^2 H_0 / 3kT \quad (5.3.3)$$

and has a fixed direction parallel to the external field. Here μ_D is the large magnetic moment of the paramagnetic dipole. The fact that the paramagnetic spectrum is observable is experimental evidence that the electron is changing states rapidly enough to make Eq. (5.3.3) valid.

The parallel component of the magnetization due to the ion is

$$H_{||} = \bar{\mu}_D r^{-3} (3\cos^3\theta - 1) \quad (5.3.4)$$

and the resulting unbroadened line shape is given by

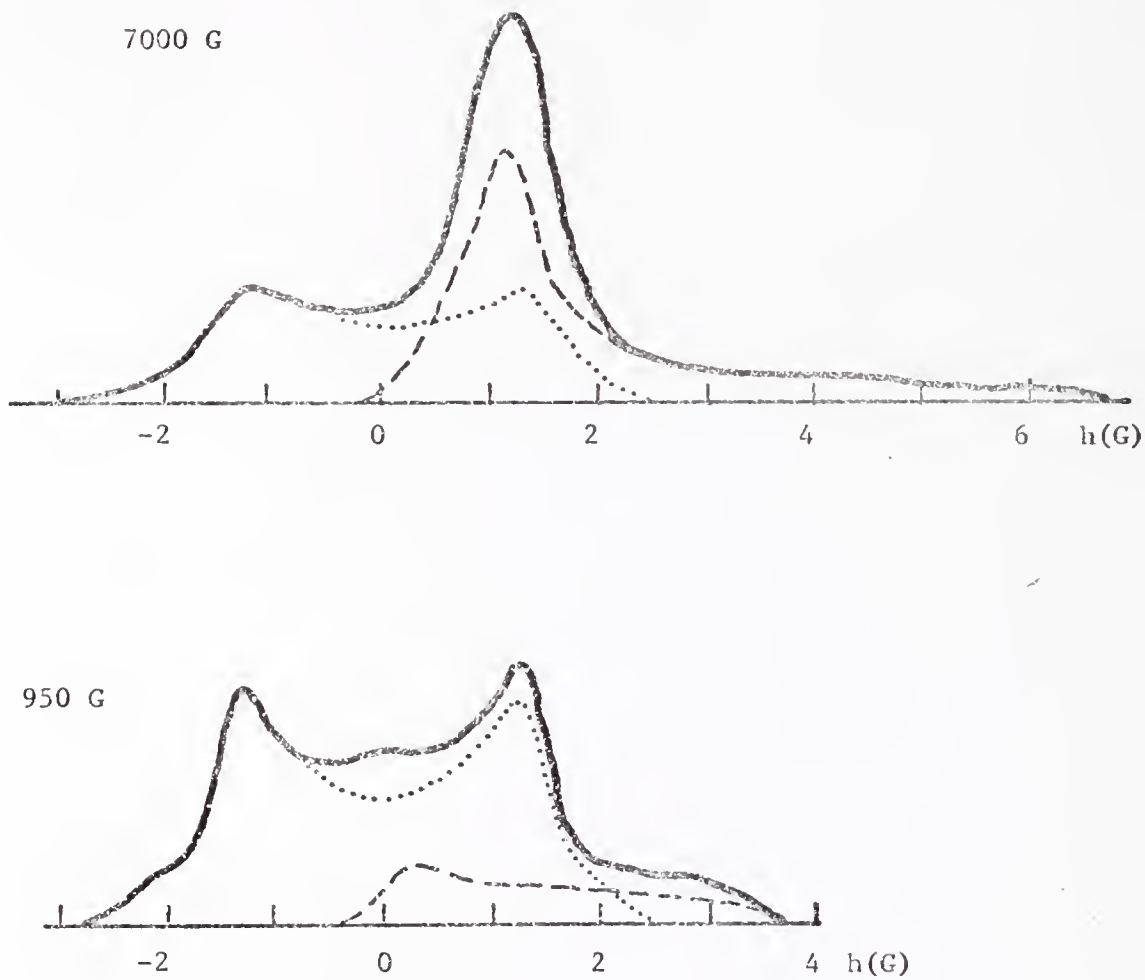


Figure 31. Possible superpositions of Pake doublet and paramagnetic spectrum which could explain data at 950 and 7000 G.

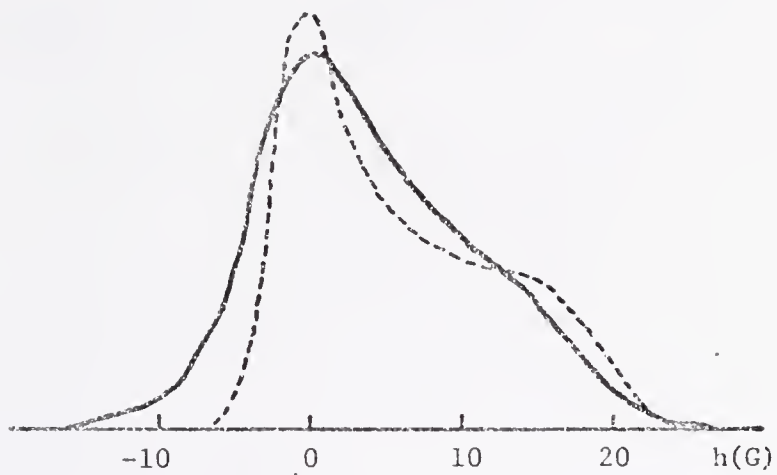


Figure 32. Calculated (---) and observed (—) NMR spectra of protons in $\text{NH}_4\text{Fe}(\text{SO}_4)_2$. Data are taken from Fig. 29 of ref. [26].

$$g(H) = \frac{1}{2\sqrt{A_1} \sqrt{H_{||} + A_1/3}}, \quad -\frac{A_1}{3} \leq H_{||} \leq \frac{2A_1}{3} \quad (5.3.5)$$

where $A_1 = 3\bar{\mu}_D r^{-3}$. This is the same form as Eq. (2.3.17) using Kroon's notation, and corresponds to the $|0\rangle \rightarrow |+\rangle$ transition in Fig. 1. Under conditions applicable to Fig. 1, some of the magnetic moments are parallel to the external magnetic field and some are antiparallel depending on their states, resulting in the two components of the spectrum. In the case of a paramagnetic ion, an average of the states is used which has a fixed direction parallel to the field, resulting in only one component of the Pake doublet.

The spectrum in Fig. 32 looks similar to some of the spectra obtained in the present work, especially those at 4000 G. However, it is deceptive as the asymmetry between the two components of the Pake doublet observed at 4000 G causes it to resemble the one asymmetric component in Fig. 32. Thus, a direct correspondence between the present data and Fig. 32 is ruled out. In addition, the spectrum observed by Kroon [26] is reversed with respect to the present data. The spectrum in Fig. 32 in fact resembles that in Fig. 30 which was calculated by a different method as might be expected.

We now compare the model of a paramagnetic line superimposed on a classical Pake powder pattern doublet to the observed data.

First, peak-to-peak separation of the Pake doublet should not be affected; however superposition of two peaks close together might cause an apparent shift of both peaks. The observed separation decreased about 5% as H_0 increased from 625 G to 4000 G, then increases about 10% as H_0 further increases to 9000 G. This is not inconsistent with the model, but cannot be even qualitatively predicted. The separation is

also affected by changes in broadening of the individual lines in the Pake doublet.

Next, it has been noted the low frequency wing extends at a rate of about 4.6×10^{-4} G per G increase in H_0 . By Eq. (5.3.5), the width of the paramagnetic line is given by A_1 , where

$$A_1 = 3\bar{\mu}_D r^{-3} = \mu_D^2 H_0 / r^3 kT \quad (5.3.6)$$

In the present case we calculate $\mu_D = 1.676 \times 10^{-21}$ erg/G taking $\nu = 8.990 \times 10^9$ Hz and $H_0 = 17,768$ G from ref. [29] since $\mu = \nu h I / H_0$. The proper value of r is somewhat in doubt as mentioned earlier, but is close to 3.5 \AA . We thus calculate

$$A_1 = 1.13 \times 10^{-4} H_0 \quad (5.3.7)$$

approximately, as the paramagnetic line width.

The data permit location of only the low frequency extent of the paramagnetic line, which extends at about four times the rate in Eq. (5.3.7) calculated for the entire line. If the paramagnetic line as a whole shifts with changing field, the linewidth may change at a rate greater or less than 4.6×10^{-4} G per G increase in H_0 . The low frequency wing observed in the data therefore may well be due to the paramagnetic spectrum.

The high frequency wing observed at low H_0 does not fit the above theory, as Eq. (5.3.7) predicts zero paramagnetic line width as H_0 approaches zero; however the data indicate about 5.5 G line width if the high and low frequency wings are counted as the limits of the paramagnetic spectrum.

If the paramagnetic spectrum is of relatively low intensity at low H_0 , it could account for the small peak between the Pake doublet peaks.

And if it increases in relative intensity as well as moving to lower frequencies, as H_0 increases, it could explain the intensity asymmetry of the Pake doublet peaks. The intensity of the Pake doublet spectrum will decrease somewhat due to broadening, but so will the intensity of the paramagnetic spectrum which widens with increasing H_0 . It is therefore rather unlikely that the paramagnetic spectrum superimposed on the Pake doublet can cause much intensity asymmetry.

Finally, the entire Pake spectrum is shifted about 0.5 G. Kroon [26] does predict a component of the local field due to the paramagnetic ion which is independent of orientation of H_0 and which would therefore shift the entire paramagnetic spectrum. It is given by

$$C = - \sum_{\ell} \mu_{\ell} r_{\ell}^{-3} P_2(\cos \beta_{\ell}) \quad (5.3.8)$$

where β is the angle between the z axis of a rectangular coordinate system in the crystal and a vector from the nucleus being observed to the dipole or paramagnetic ion. Averaging over the twelve nearest neighbor positions results in zero net shift, some parts of the spectrum being shifted one way and some parts the other way.

In order for the Pake doublet to be shifted, a relatively uniform field would have to exist throughout the sample. Possibly a very uniform distribution of O_2 could cause such a field, however the effect should increase with H_0 which was not the case.

Piott and McCormick [25] measured the shift of the anomalous peak from the center of the line as a function of temperature and compared it with the calculated shift. At 4.2 K, the shift is about 30 to 35 G, much larger than that predicted by Eq. (5.3.7) even after considering that the value of r is different. However, the peak in Fig. 30 taken from reference [25] is at about -3, units not given. Units are also omitted

on the experimental spectrum, and not much information is furnished with regard to temperature, field strength H_0 , etc., so it is difficult to draw any quantitative conclusions from ref. [25].

Line width variation as a function of O_2 concentration is shown in Fig. 29 and is consistent with expectations. A decreasing O_2 concentration results in fewer ^{15}N nuclei close enough to an O_2 molecule to be influenced by it, and broadening approaches that due to intermolecular dipole-dipole interactions between ^{15}N nuclei.

The main feature of the spectrum at low O_2 concentration is the asymmetry of the peak intensity. Because the relaxation time was on the order of several hours it was difficult to obtain good resolution of the line shape; however, the narrowing and asymmetry were reproducible.

If the spectrum is a superposition of a paramagnetic line and a Pake doublet as discussed earlier, it is still a possible mechanism here, as the enhancement due to a relatively faster relaxation rate could offset the reduction due to the lower concentration.

In summary, the paramagnetic O_2 could account for the low frequency wing and part of the asymmetry of the Pake peaks. Also, the increasing broadening with increasing H_0 and with increasing O_2 concentration are to be expected. It does not fully explain the peak asymmetry, the shift of the Pake doublet, and the behavior of the high frequency wing.

5.3.2 Ortho-Para Conversion

As $h\nu/kT$ is on the order of 10^{-6} in the present experiment, the $|+\rangle$, $|0\rangle$ and $|-\rangle$ population differences are equal to an excellent approximation according to the Boltzmann distribution. Therefore, the Pake doublet shown in Fig. 1 is symmetric.

Hydrogen molecules, consisting of two spin- $\frac{1}{2}$ protons, also have a triplet and singlet state similar to $^{15}\text{N}_2$ discussed in Sec. 2.2. Triplet and singlet state molecules are called ortho and para molecules, respectively. When hydrogen is cooled at a nominal rate to below 1.2 K, ortho-para conversion does not occur rapidly enough to maintain thermal equilibrium. Hardy and Berlinsky [27] and Berlinsky and Hardy [28] have shown that the conversion rates from the three ortho states depend on the state of the ortho molecule, the magnetic field H_0 , and the angle between the molecular axis and H_0 . Thus, the $|+\rangle$, $|0\rangle$ and $|0\rangle$, $|-\rangle$ population differences are not equal which results in an asymmetric Pake doublet.

A family of curves is shown in ref. [28] which closely resembles the data in Figs. 26-28. However, the asymmetry increases with decreasing field H_0 in ref. [28], counter to the field dependence in the present work.

It is noted that the theory in refs. [27,28] depends on a net ortho-para conversion. The spin state populations are set at high temperature, and an energy difference between the ortho and para states causes this net conversion at low temperature.

In the case of $^{15}\text{N}_2$, the ortho and para states are separated by on the order of a microdegree [30], and hence ortho-para conversion would not be significant unless the sample were cooled to about 1 μK .

The theory of ortho-para conversion presented in refs. [27,28] must therefore be discounted on both experimental and theoretical grounds as applied to the present case.

5.3.3 ^{14}N Impurity

The sample contained about 0.5% ^{14}N in the form of $^{14}\text{N}_2$ and $^{15}\text{N}-^{14}\text{N}$

molecules. In the mixed molecule, the ^{15}N Zeeman energy is perturbed by the ^{15}N - ^{14}N dipole-dipole interaction which is dependent on the state of the ^{14}N molecule. The perturbation is on the same order as the $^{15}\text{N}_2$ dipole-dipole interaction, and the resulting spectrum overlaps the Pake powder pattern spectrum due to the $^{15}\text{N}_2$ molecules. This effect has been worked out theoretically in Sec. 2.5 and experimental results are presented in Chap. VI.

Due to the low concentration of ^{15}N - ^{14}N molecules, a superposition of the mixed molecule spectrum and the $^{15}\text{N}_2$ Pake spectrum cannot differ significantly from the pure Pake spectrum.

The ^{14}N nuclei in either $^{14}\text{N}_2$ or ^{15}N - ^{14}N mixed molecules undergo nuclear quadrupole transitions, some of which are of the same frequency as the ^{15}N Zeeman transitions for certain orientations and external magnetic field strengths. The transition frequencies are shown in Fig. 33 as a function of H_0 and the angle between H_0 and the molecular axis.

It can be seen that only a small percent of the transitions are near the ^{15}N Zeeman transition frequency and therefore, considering the small concentration of ^{14}N nuclei, the ^{14}N spectrum in the vicinity of the ^{15}N Zeeman spectrum must be undetectable.

There is another interaction, however, known as level crossing which could have a much greater effect on the spectrum than indicated by the low concentration of ^{14}N in the sample. Smith and Cotts [31] have studied this effect in thiourea, $\text{SC}(\text{NH}_2)_2$, in an external magnetic field of such a magnitude as to make the proton Zeeman frequency about equal to the one of the nitrogen quadrupole transition frequencies. In this region spin exchange can occur which shifts the nitrogen resonance frequency. The effect is schematically indicated in Fig. 34 which has been

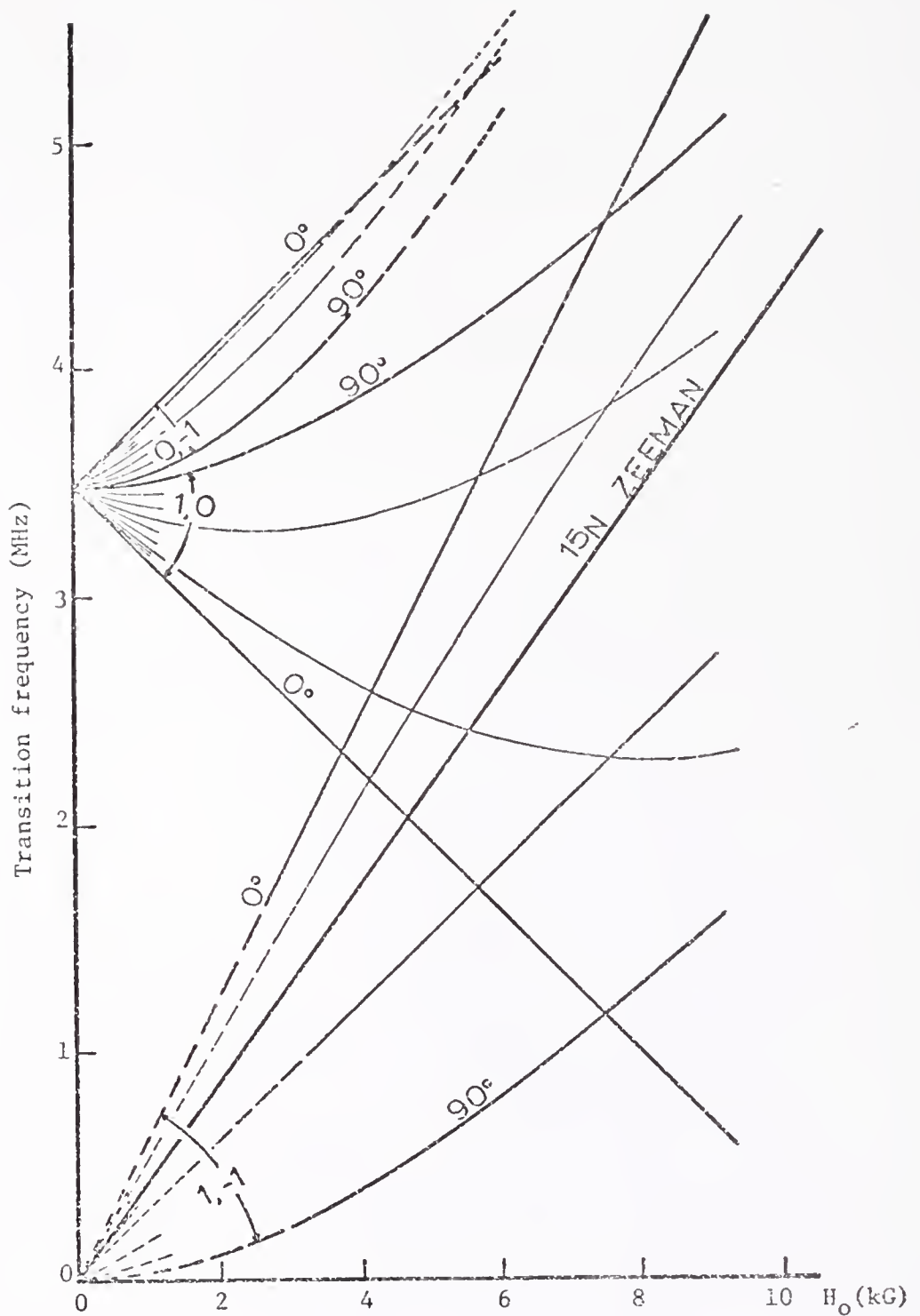


Figure 33. Quadrupole transition frequencies of ^{14}N and Zeeman frequency of ^{15}N as a function of magnetic field H_0 and angle θ between H_0 and the molecular axis. The dashed lines indicate transitions which are forbidden in the limit of low or high magnetic fields.

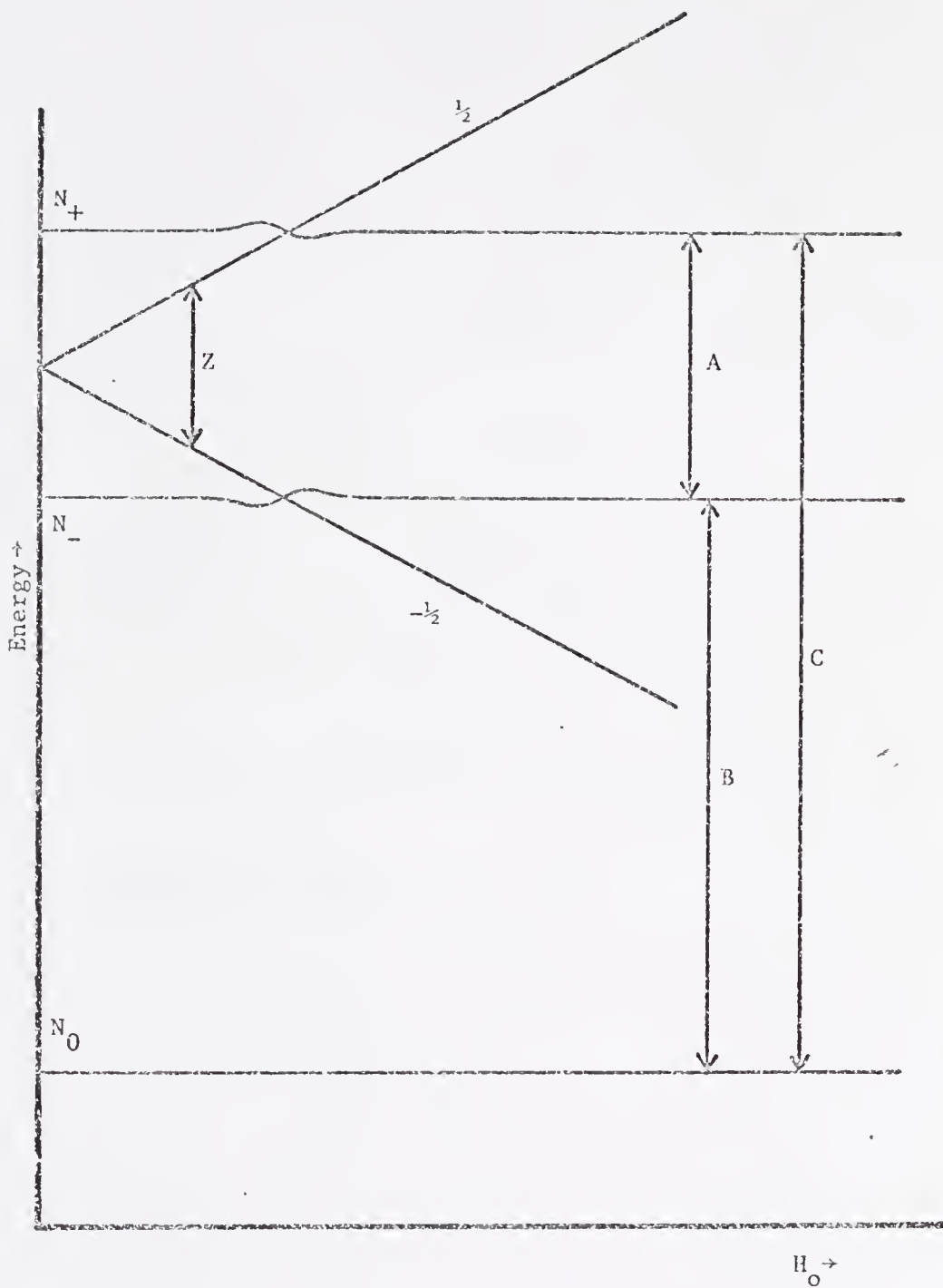


Figure 34. Qualitative effect on energy levels when the proton Zeeman transition energy matches a ^{14}N quadrupolar transition energy in $\text{SC}(\text{NH}_2)_2$. The +1, -1, and 0 levels of ^{14}N are labeled N_+ , N_- , and N_0 , respectively, and the proton levels are labeled $+\frac{1}{2}$ and $-\frac{1}{2}$. The effect is illustrated for the case $Z \approx A$, but should occur at $Z \approx B$ and $Z \approx C$, also. The diagram is a modification of Fig. 8 in ref. [31].

exaggerated for clarity. As H_0 is increased, the proton Zeeman energy Z increases until it approaches the energy difference A between the nitrogen $+1$ and -1 states, N_+ and N_- . When Z is slightly below A , the effect is to 'repel' the N_+ and N_- levels which increases A . They observed the N_-, N_0 transition B and N_+, N_0 transition C , and found B decreased while C increased. As H_0 was further increased beyond the value where A and Z were equal, the effect reversed. Similar effects should occur in the region where the proton Zeeman energy approximately equals the N_-, N_0 or N_+, N_0 transition. An expected consequence verified experimentally [31] is that level crossing permits cross relaxation which greatly enhances the relaxation rates of both the nitrogen and protons.

Relative to the present experiment, the experiment in ref. [31] is much simpler, thus facilitating theoretical analysis and experimental verification. First, a single crystal was available which permitted a knowledge and choice of orientation of H_0 . Next, only two types of molecules exist with nitrogen frequencies separated enough to permit observation of only one type. Thus, all the nitrogen nuclei had the same three energy levels and level crossing occurred at well-defined magnetic fields, permitting observation of the effect at values of H_0 changing continuously from below to above the crossing. Third, effects were intramolecular with the same relative orientation of protons and nitrogen. Finally, the proton Zeeman resonance was a single line.

In contrast, the sample used in the present experiment contained $^{15}N_2$, $^{14}N_2$ and $^{15}N-^{14}N$ molecules. There are three $^{15}N_2$ dipole-dipole perturbed Zeeman levels, three ^{14}N quadrupole levels strongly field dependent, and six $^{15}N-^{14}N$ levels with transitions in the vicinity of

the $^{15}\text{N}_2$ transitions. There are four molecules in the unit cell, each with a different orientation, and each has 12 nearest neighbors which must be considered. Finally, the sample was polycrystalline with effectively a continuum of orientations, and all of the energy levels are orientational dependent.

The twelve levels result in seven transitions at very low external fields and perhaps eight transitions at higher fields. At every magnetic field and orientation, a minimum of five transitions are within about a two-kHz spread, and at certain values of H_0 and orientations, as many as 7 transitions are in the same neighborhood. Thus the possibilities for level crossing are numerous. Even though the ^{14}N concentration is only on the order of 0.5%, cross relaxation can cause an enhancement of the level-crossing effect by increasing the relaxation rate. It therefore could have a significant effect on the line shape.

There is an intuitive objection to level crossing as the major mechanism causing the anomalous line shape, however. The observed effects such as the peak intensity asymmetry, the high and low frequency wings, and the small hump between the Pake doublet peaks all change monotonically with increasing H_0 . This would be more plausible if the various transitions were all either approaching towards or receding from each other, or some of each. However, in the actual sample, transitions approach, cross, and recede and we would expect shifts first one way then the other and a spectrum with a more complex magnetic field dependence.

5.3.4 Conclusions

The spectrum consists of a Pake powder pattern doublet with

broadening and a low frequency wing due to paramagnetic O_2 . The asymmetry in peak intensity has not been explained. Other systems such as ^{13}CO , $D_2^{13}C_2$ and O_2 impurity in a $^{15}N_2$, $^{14}N_2$, ^{15}N - ^{14}N mix might be helpful in identifying the various components of the observed spectra.

CHAPTER VI
RESULTS AND DISCUSSION - NMR SPECTRUM OF
 ^{15}N IN SOLID $^{15}\text{N}-^{14}\text{N}$

6.1 Sample

The nitrogen sample contained a statistical mix of 33% ^{15}N which resulted in proportions of $^{15}\text{N}_2$, $^{15}\text{N}-^{14}\text{N}$, $^{14}\text{N}_2$ molecules in a 1:4:4 ratio. In the vicinity of the ^{15}N Zeeman spectrum there were twice as many ^{15}N nuclei participating in the $^{15}\text{N}-^{14}\text{N}$ mixed molecule spectrum as in the $^{15}\text{N}_2$ (Pake doublet) spectrum. We therefore calculate the two spectra separately then superimpose 50% of the $^{15}\text{N}_2$ Pake doublet spectrum on the $^{15}\text{N}-^{14}\text{N}$ mixed spectrum.

6.2 Data

The data are presented in Figs. 35 and 36. A relaxation time on the order of an hour was encountered making it difficult to obtain a good spectrum and at external fields below 5000 G the signal-to-noise ratio was very poor. The relaxation time was not shortened by addition of a paramagnetic impurity because of the effect of O_2 on the line shape.

The intensity of the signal is, of course, expected to increase with increasing H_0 as was observed. Absolute intensity measurements were not made; however the intensity increase was more pronounced when the field was increased from 4000 G to 5000 G than at higher or lower fields. At lower fields, results were very poor, but at higher fields

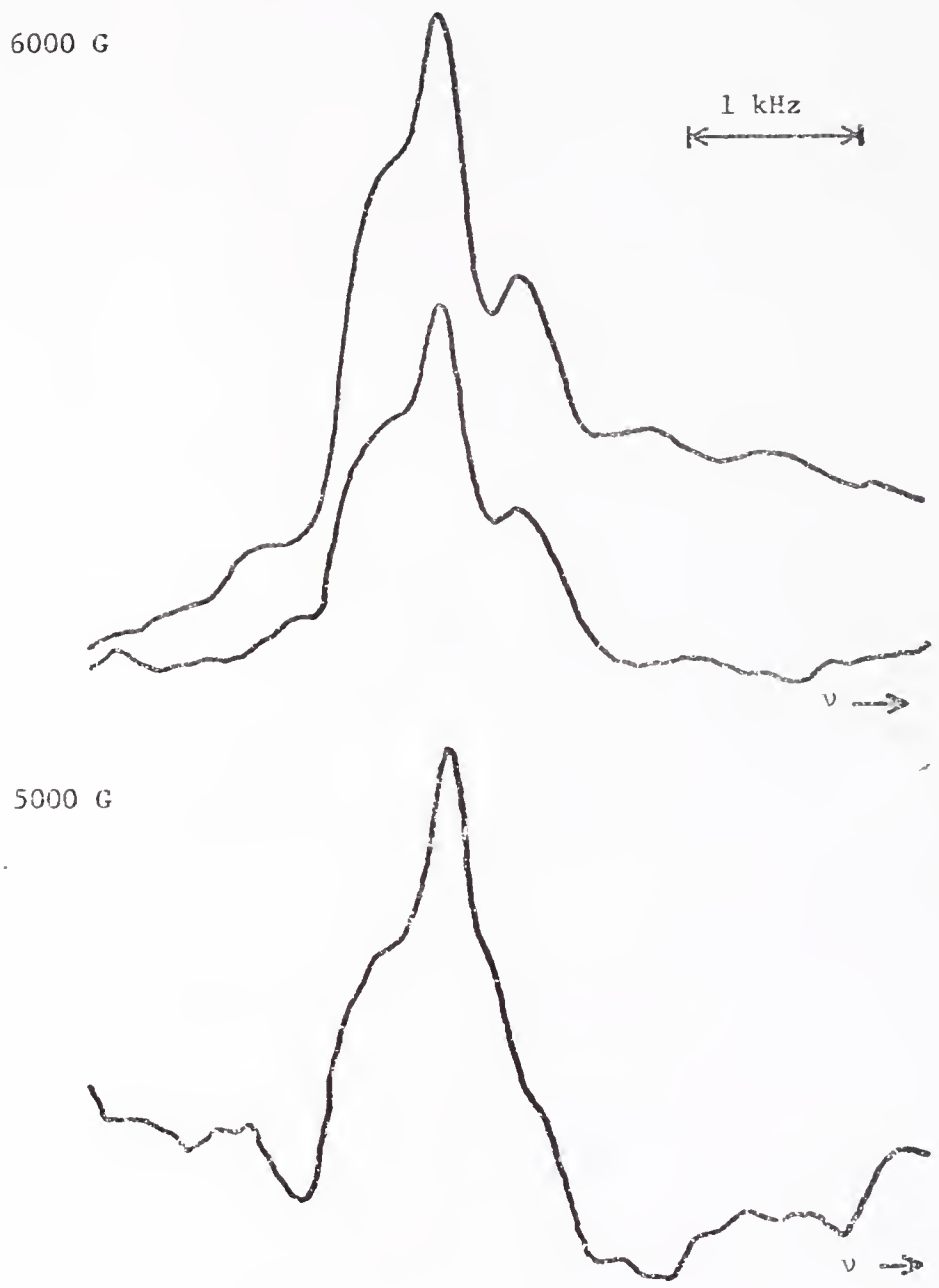


Figure 35. NMR spectra of ^{15}N in $\alpha\text{-N}_2$ enriched to 33% ^{15}N at 5000 and 6000 G.

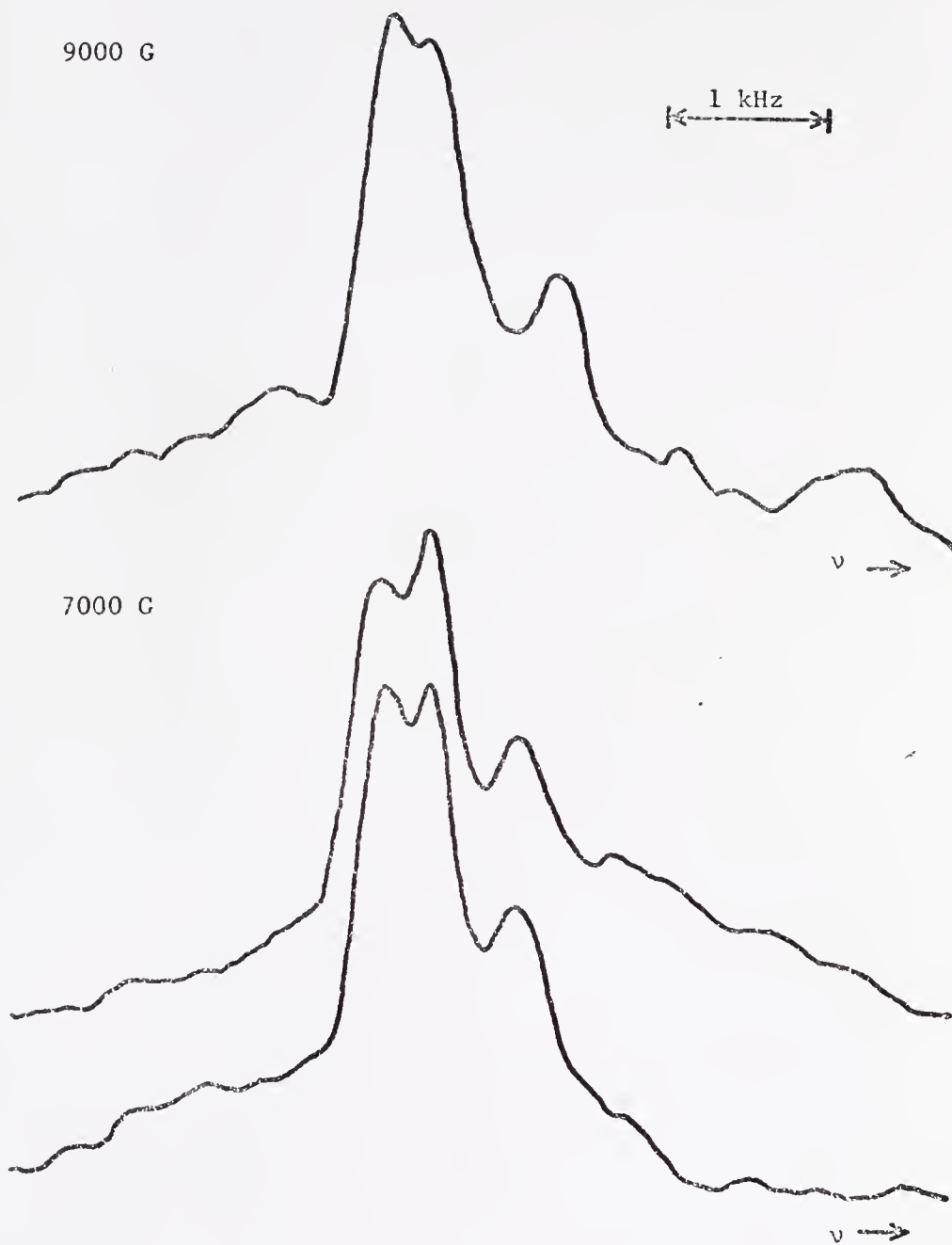


Figure 36. NMR spectra of ^{15}N in αN_2 enriched to 33% ^{15}N at 7000 and 9000 G.

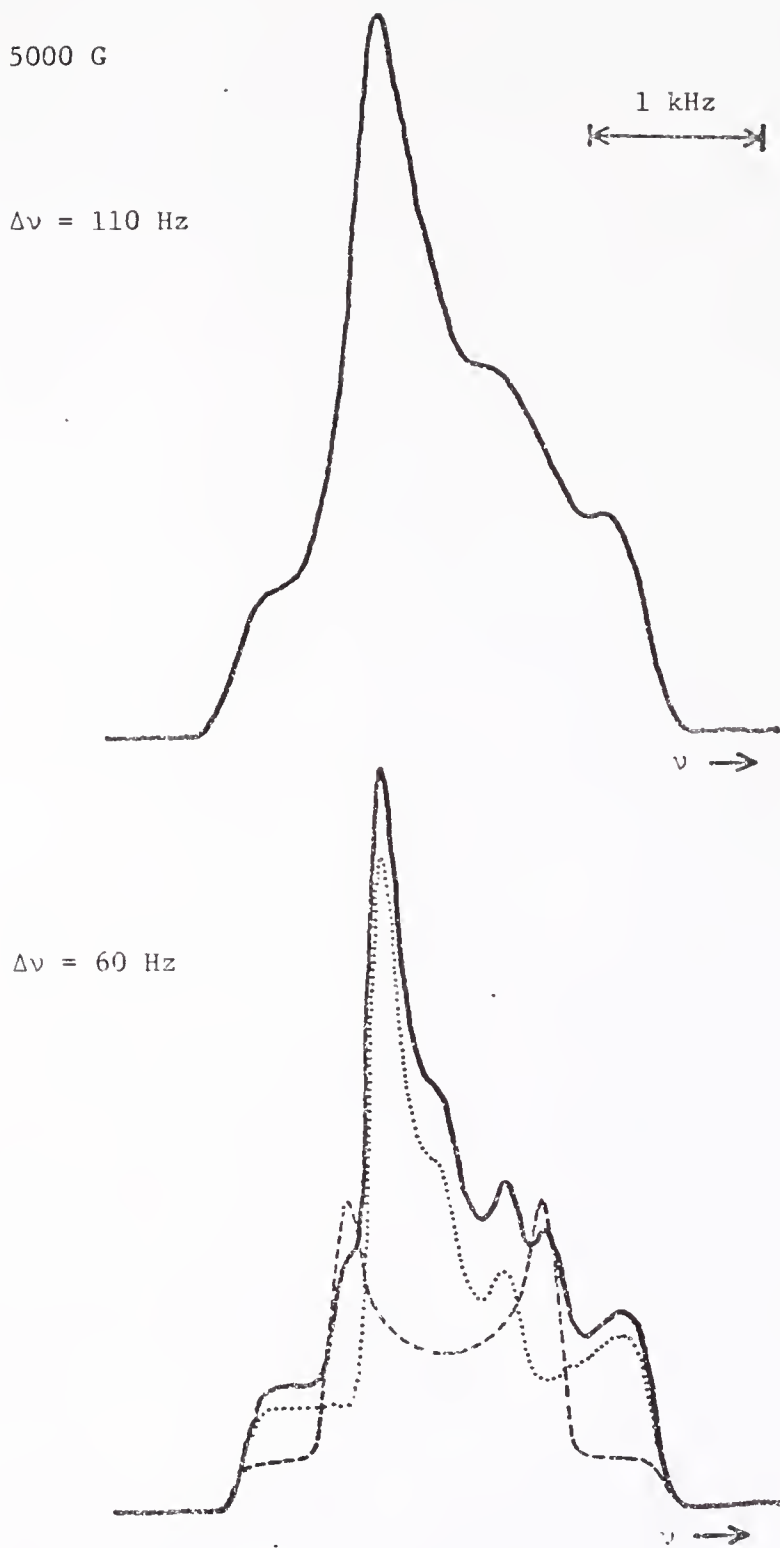


Figure 37. Calculated NMR spectra of ^{15}N in $\alpha\text{-N}_2$ enriched to 33% ^{15}N at 5000 G. The lower figure is the sum of the triplet (\dots) resulting from the ^{15}N - ^{14}N molecules and 50% of the Pake doublet ($---$) resulting from the $^{15}\text{N}_2$ molecules. Gaussian broadening of 60 and 110 Hz is shown.

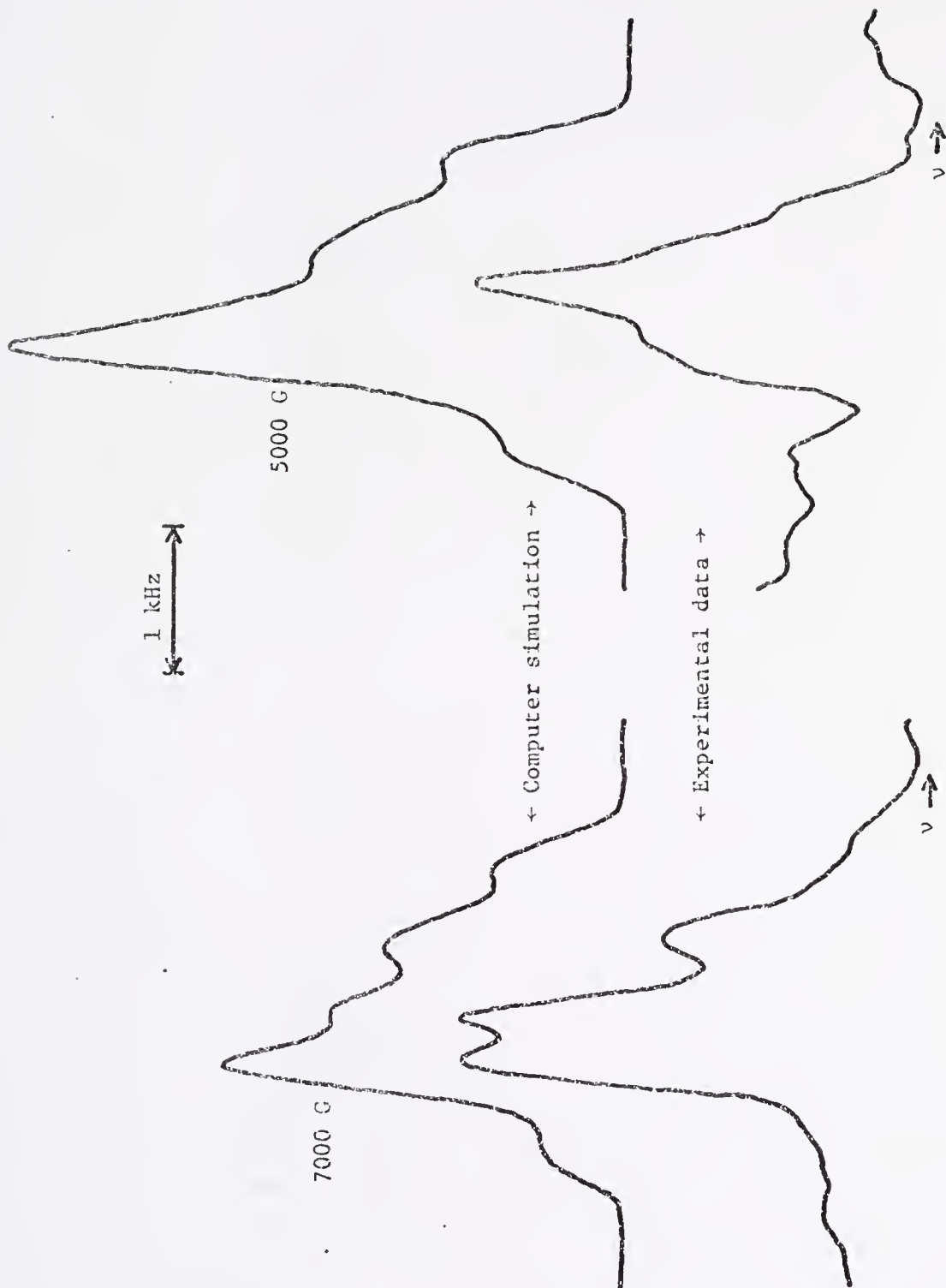


Figure 38. Comparison of NMR spectra of ^{15}N in $\alpha\text{-N}_2$ enriched to 33% ^{15}N with computer simulation at 5000 and 7000 G.

reproducibility was fairly good. Two curves at 6000 G and 7000 G are shown as an illustration. The main features change rather uniformly with increasing applied magnetic field.

6.3 Computer Simulation

A FOCAL program (Appendix A) was used to calculate the powder pattern spectrum predicted by Eq. (2.5.29) broadened by a Gaussian function. Figure 37 shows the calculated spectrum at 5000 G. The lower figure shows the individual components obtained from the ^{15}N - ^{14}N triplet (dotted curve) and the $^{15}\text{N}_2$ Pake doublet (dashed curve). The solid line is the sum of the triplet and 50% of the Pake doublet intensity.

Effects of varying the intermolecular broadening are shown by the two solid curves in Fig. 37. Comparison with Fig. 35 indicates the line width is about 100 Hz. Brookeman, McEnnan, and Scott [21] calculated the line width of dipolar broadened NQR lines in solid α nitrogen and found it to be on the order of 100 Hz. A similar broadening in the case of ^{15}N NMR is expected although the calculations are not the same.

6.4 Data Analysis

Figure 38 is a comparison of the data with the computer simulations. Intensity differences between the data and the simulations are not significant.

The theory predicts the main features of the spectrum such as the number and position of the peaks. However, the relative intensities are not correctly predicted. The asymmetry of the Pake doublet discussed in Chap. V and the level-crossing mechanism mentioned in Sec. 5.3.3 may be causes of the unexpected peak intensities.

6.4.1 Asymmetric Pake Doublet

In this chapter and in Sec. 2.5, it was assumed the Pake doublet would be symmetric. Noting the data in Chap. V do not bear this out, we would expect some similar effect here. The narrow but asymmetric peaks observed with very low O_2 concentration in pure $^{15}N_2$ (Fig. 29) could well account for the two peaks observed in the data at 7000 G and 9000 G in Figs. 36 and 38. The simulation has two peaks also but one is of such low intensity that it is not resolved. An analytical formula for the asymmetry in $^{15}N_2$ is not yet known so it cannot be included in the computer calculations at this time. Furthermore, the shift in the entire Pake spectrum observed with 0.1% O_2 added to $^{15}N_2$ is not understood quantitatively. Thus the experimental spectrum is thought to be the calculated spectrum modified by the asymmetric Pake doublet with perhaps other effects due to level crossing also present.

6.4.2 Level Crossing

Level crossing was discussed in Sec. 5.3.3. It should be a much more significant effect in the present case with 33% ^{15}N as concentrations of the various types nuclei are of the same order.

It was noted in Chap. V that the level crossings varied in a complex way with field, orientation, type of nuclei and molecule, etc., but the spectrum smoothly went from a nearly symmetric Pake doublet to a highly asymmetric doublet. In the present case the change between 5000 G and 7000 C is not as smooth. Furthermore, it was noted in Sec. 6.1 that the intensity did not increase smoothly as the magnetic field increased.

We note that level crossing increases more rapidly at approximately

the same magnetic fields. Referring to Fig. 33, there is an increase in level crossing above 3780 G due to the $1, 0$ and $1, -1$ ^{14}N quadrupole transitions overlapping for some orientations and another increase above 4700 G where the ^{15}N Zeeman line overlaps the $1, 0$ ^{14}N transition. The actual situation is a little more complex as ^{15}N - ^{14}N dipole-dipole perturbation has not been included in Fig. 33. Thus, level crossing may be more effective here than in the case of the ^{15}N Pake doublet discussed in Chap. V.

6.5 Conclusions

The ^{15}N NMR spectrum observed in the 33% ^{15}N sample is a combination of a triplet due to dipole-dipole perturbation of ^{15}N in ^{15}N - ^{14}N molecules superimposed on the Pake doublet resulting from the $^{15}\text{N}_2$ molecules. Differences between the calculated and observed line shapes are probably due to the asymmetry of the $^{15}\text{N}_2$ Pake doublet spectrum and to level-crossing effects.

It would be informative to examine the spectrum as a function of ^{15}N concentration, especially if the proportion of ^{15}N - ^{14}N mixed molecules to $^{15}\text{N}_2$ molecules were increased above that of a statistical mix. Study of a single crystal specimen would probably provide a definitive explanation of the complex behavior observed in the powder samples. However, it is exceedingly difficult to obtain a good single crystal of α nitrogen because of the disruption of the α - β phase transition.

CHAPTER VII
RESULTS AND DISCUSSION -- NUCLEAR SPIN-LATTICE RELAXATION
IN LIQUID AND SOLID $^{15}\text{N}_2$ AND $^{14}\text{N}_2$

7.1 Previous $^{15}\text{N}_2$ and $^{14}\text{N}_2$ Relaxation Time Studies

Relaxation time studies in nitrogen are of interest because they afford the opportunity to isolate two different relaxation processes in nearly the same dynamic environment. Molecules of the two stable isotopes $^{15}\text{N}_2$ and $^{14}\text{N}_2$ have only a small isotopic mass difference and therefore nearly the same molecular dynamics, but the dominant relaxation mechanism is different in each case. Relaxation via dipolar interactions and anisotropic chemical shift is negligible for both isotopes. Spin-rotational relaxation is therefore dominant in $^{15}\text{N}_2$ which has no quadrupolar interaction, whereas quadrupolar relaxation in $^{14}\text{N}_2$ dominates the spin-rotational relaxation [24]. Hence relaxation time measurements in $^{15}\text{N}_2$ and $^{14}\text{N}_2$ yield T_{1sr} and T_{1Q} , respectively.

Relaxation times had been measured in $^{14}\text{N}_2$ from 4.2 K to 145 K [22,24,32] and in $^{15}\text{N}_2$ from 77 K to 130 K [24]. Krynicki, Rankamaa, and Powles [24] found that the data tend towards the Hubbard relation [14]

$$\tau_Q^* \tau_{sr}^* = 1/6 \quad (2.6.6)$$

as the temperature is reduced to 77 K. As the sample temperature is lowered from 130 K, τ_Q at first is less than τ_{sr} but they become equal at about 77 K. Thus τ_Q and τ_{sr} are approaching the $\tau_Q \gg \tau_{sr}$ condition which is necessary to the Hubbard relation as discussed in Sec. 2.6.

Figure 39. Nitrogen spin-lattice relaxation times T_1 in $^{15}\text{N}_2$ (in seconds) and $^{14}\text{N}_2$ (in milliseconds). The solid line is a smooth curve through the present $^{15}\text{N}_2$ T_1 data (solid circles) and data (x's) taken from ref. [24]. An average value of 55 seconds observed for T_1 of $^{15}\text{N}_2$ at 38 K and represented by an open circle is probably affected by O_2 impurity. The dashed line is a smooth curve through $^{14}\text{N}_2$ T_1 data from refs. [22], [24], and [32]. The triple point and critical point are indicated by t.p. and c.p., respectively.

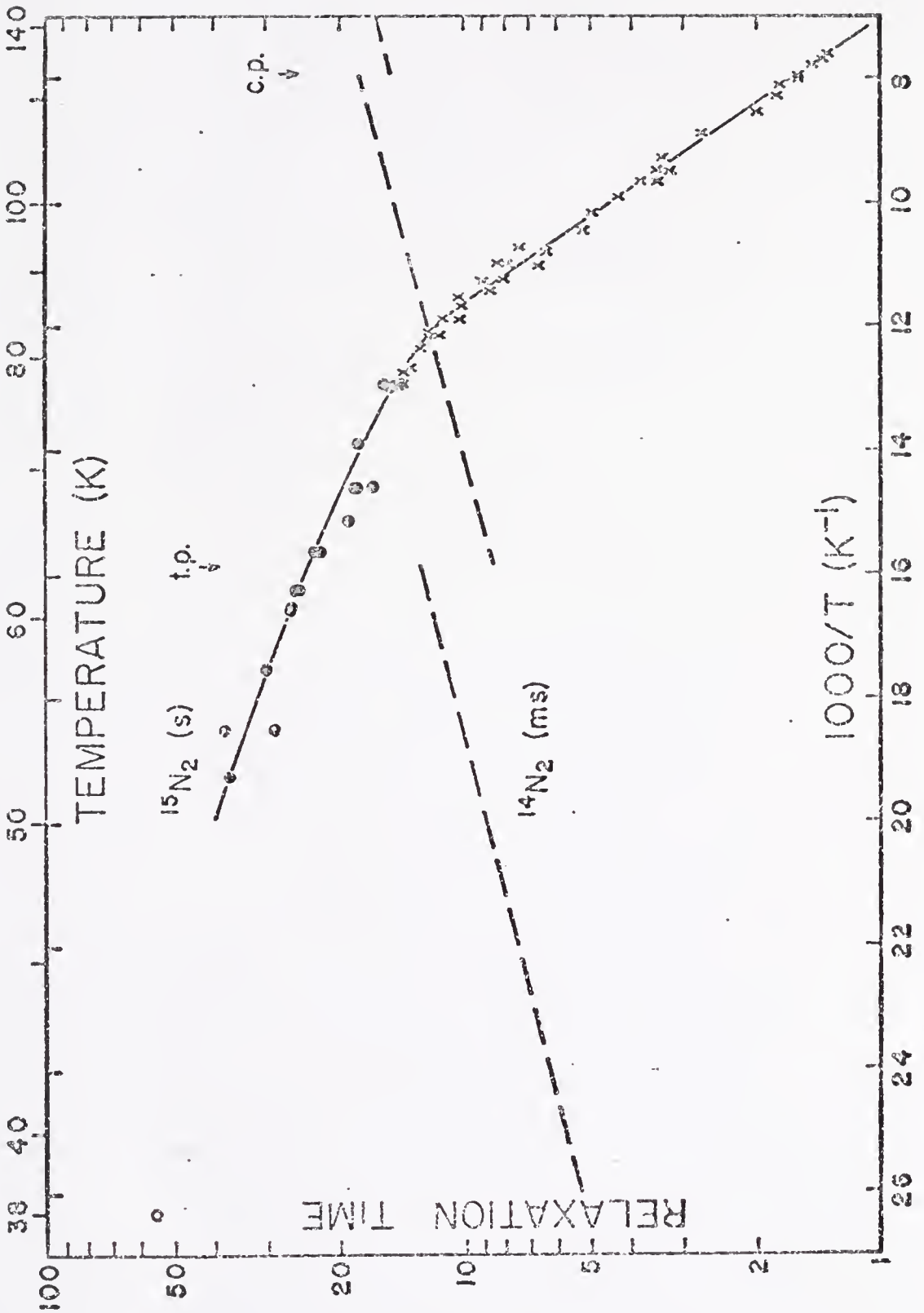
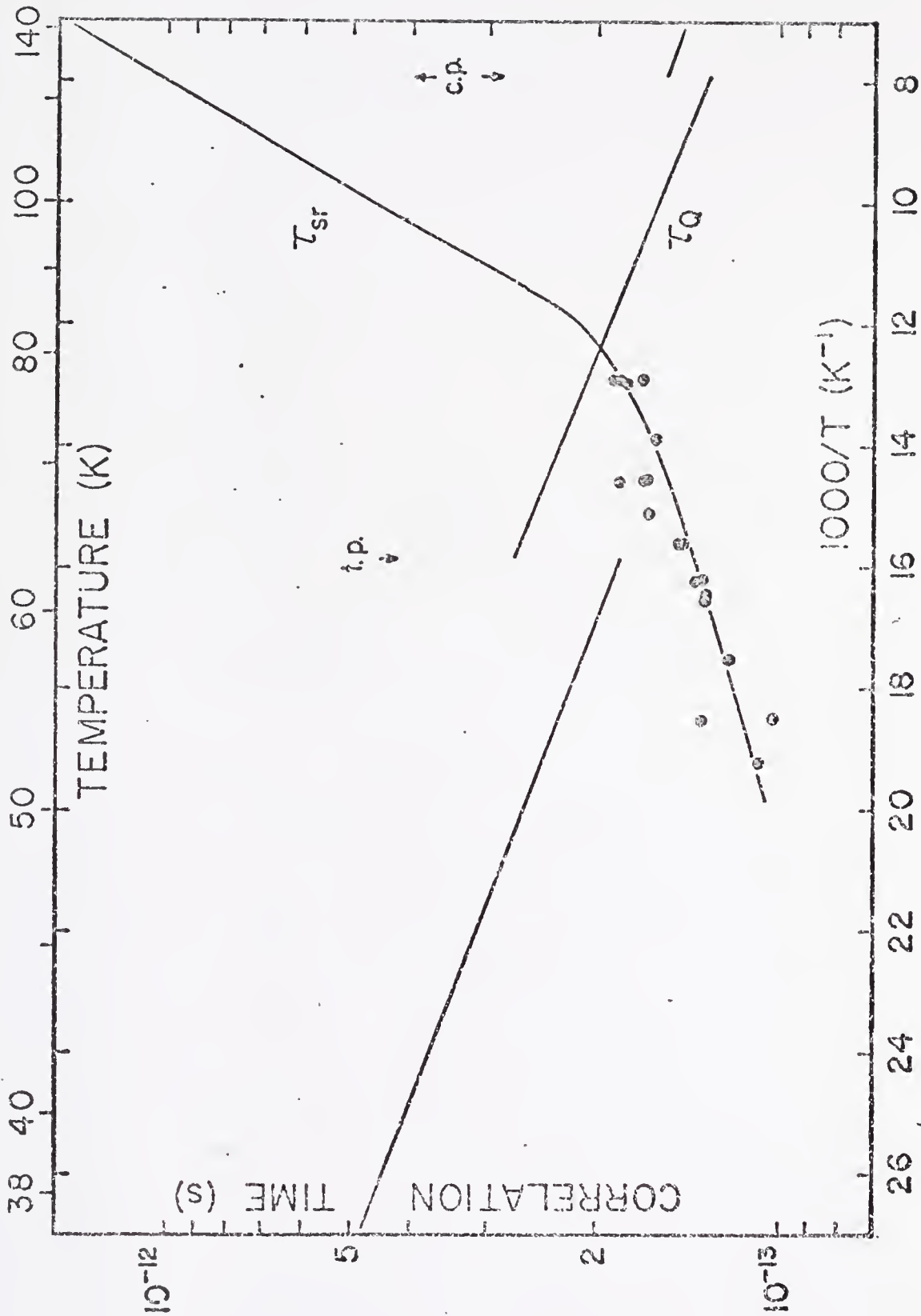


Figure 40. Correlation times τ_Q and τ_{sr} in $^{14}\text{N}_2$ and $^{15}\text{N}_2$ respectively. The solid circles and smooth curves were calculated from the corresponding circles and curves in Fig. 39.



The present work extends the relaxation-time measurements in liquid $^{15}\text{N}_2$ from 77 K down to the triple point 63 K, and in β -solid $^{15}\text{N}_2$ from 63 K down to 38 K, near the α - β phase transition.

7.2 Data

The observed spin-lattice relaxation times are shown in Fig. 39 as solid circles. The open circle at 38 K represents the average value of 55 seconds observed. It is possible this value was affected by the residual O_2 impurity and such a long T_1 is also more susceptible to magnet instabilities, therefore it is not used in the analysis. The data are in excellent agreement at 77 K with those of ref. [24] which are plotted as x's, and confirm the small departure from linearity noticeable in the data from ref. [24]. The solid line in Fig. 39 is a smooth curve through the data and the dashed line is a smooth curve through $^{14}\text{N}_2$ data from refs. [22,24,32]. It should be noted that relaxation times for $^{14}\text{N}_2$ and $^{15}\text{N}_2$ are in milliseconds and seconds, respectively, so it can be seen that the spin-rotation interaction is negligible in $^{14}\text{N}_2$ as asserted earlier.

Equations (2.6.3) and (2.6.4) were used to calculate the correlation times which are plotted in Fig. 40. The spin-rotational constant C in Eq. (2.6.3) was taken as 22 kHz [33] and the most recent value of the quadrupole coupling constant $e^2qQ/h = 5.39 \pm 0.05$ MHz [34] was used in Eq. (2.6.4). The smooth curves and solid circles were calculated from the smooth curves and solid circles, respectively, from Fig. 39. Finally, the reduced correlation times were calculated from the solid circles and smooth curves in Fig. 40 and a plot of τ_Q^* versus τ_{sr}^* on a log-log scale is shown in Fig. 41. The Hubbard relation is shown as a dashed line for comparison.

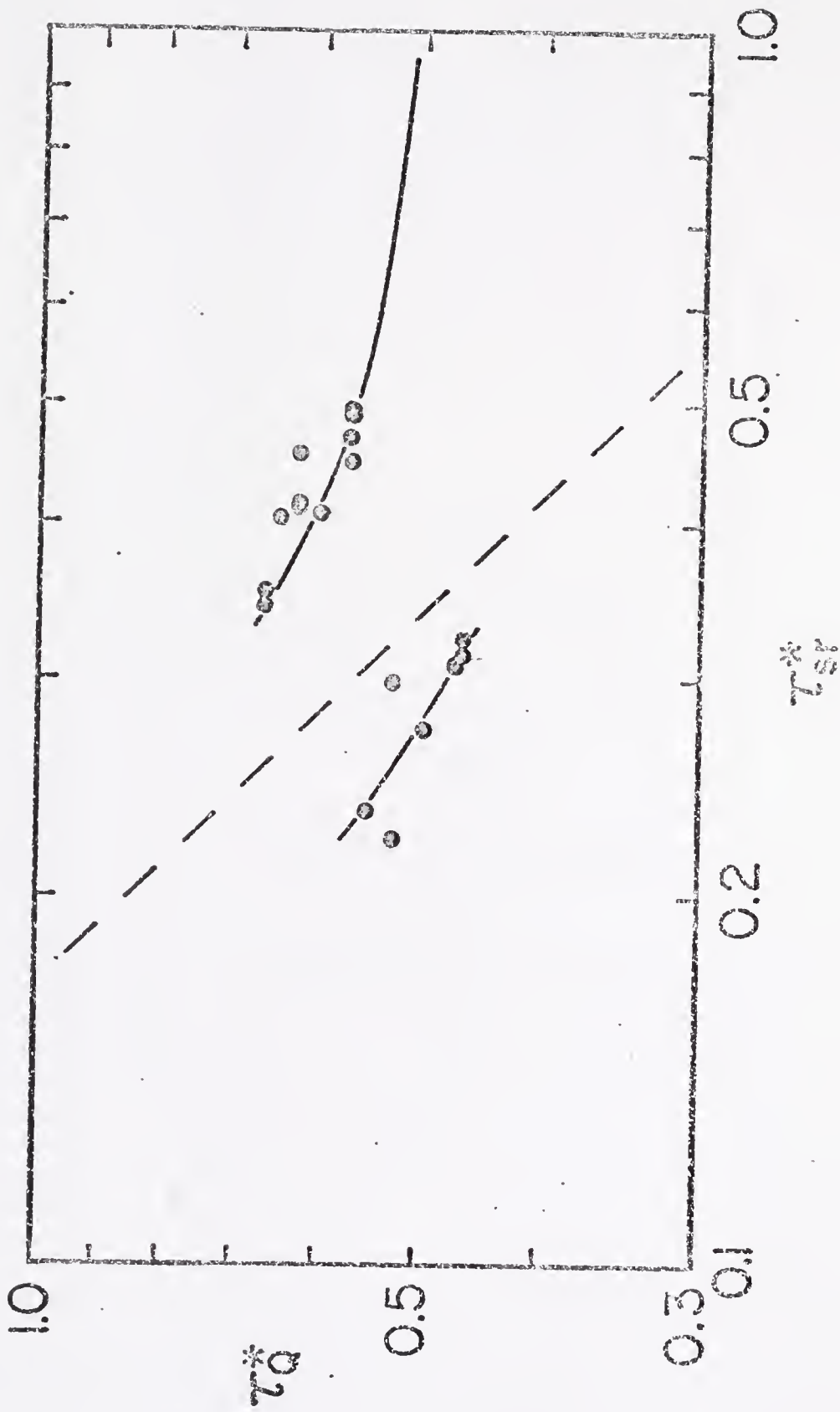


Figure 41. The reduced correlation time $(\tau^* = \tau(kf/I_0)^{1/2})$ vs. τ_{sr} . The solid circles and smooth curves were calculated from the corresponding circles and curves on Fig. 40. The dashed line is a plot of the Hubbard relation $\tau_Q^* = 1/6$.

Krynicky, Rahkamaa, and Powles [24] noted an approach towards the Hubbard relation as they lowered the temperature to 77 K and the present data confirm this tendency as the temperature is lowered to the triple point. We note that a temperature independent constant other than $1/6$ in the product $\tau_Q^* \tau_{sr}^*$ would result in a line parallel to the dashed line but offset from it. The experimental curve in the liquid appears to approach the dashed curve both in slope and in value of the constant. The discontinuity at the triple point is due to the discontinuity in T_{lQ} . Any discontinuity in T_{lsr} which may exist within the limits of experimental accuracy cannot be large enough to significantly modify the graph. The slope of τ_Q^* versus τ_{sr}^* should vary depending on how well the condition $\tau_{sr}^* \ll \tau_Q^*$ is met. As τ_Q^* decreases significantly across the gap, the condition $\tau_{sr}^* \ll \tau_Q^*$ is farther from being realized on the solid side of the gap, which would predict a change in the slope. Any such discontinuity in the slope is not discernible against scatter in the experimental results. The significant observation is that the slope is approximately the same across the triple point gap, and at lower temperatures in the solid the product of the reduced correlation times approaches even closer to a temperature independent constant than in the liquid. The value of the constant is apparently less than $1/6$, however.

7.3 Crystalline Structure of β -Solid Nitrogen

In order to understand the behavior of data above and below the triple point, we first look at the structure of β nitrogen. It is known from x-ray diffraction [20,35] to be hexagonal close packed with two molecules per unit cell in space group $P6_3/mmc(D_{6h}^k)$. The c/a ratio is very close [36] to the ideal closepacking value of 1.632. Each molecule

is surrounded by 12 nearest neighbors forming a cage structure as shown in Fig. 42. The anisotropic part of the intermolecular potential exhibits six primary minima produced by groups of four molecules at the corners of the square faces forming the cage structure. Three of these minima are above the horizontal midplane of the figure and three below. While one end of the molecular axis points towards the center of one of these square faces, the other end intersects a triangular face. For an ideal c/a ratio the polar angle θ between the c axis and a line drawn from the central molecule to the center of one of the square faces is $54^{\circ}44'$.

As the potential wells are rather shallow, the molecule executes frequent reorientational jumps among the six potential minima. Jumps between adjacent minima while maintaining the $54^{\circ}44'$ polar angle produce an angular reorientation by $48^{\circ}11'$. In addition, reorientation between minima may occur by tilting the molecular axis through a polar angle by $70^{\circ}32'$. There is thus a twelve-fold model for reorientation; however, for homonuclear molecules, the six orientations following a tilt are equivalent to the six without a tilt. The $48^{\circ}11'$ jumps are presumably more probable than the $70^{\circ}32'$ jumps. From the standpoint of an NMR experiment, rapid reorientation among these 12 configurations is indistinguishable from a continuous precession about the c axis at a fixed polar angle θ . In particular, the electric field gradient tensor is averaged by such motion according to the factor $\langle P_2(\cos\theta) \rangle$ which vanishes for the 'magic' angle of $54^{\circ}44'$.

This picture is confirmed by the fact that the ^{14}N nuclear quadrupole coupling constant in β nitrogen is reduced by three orders of magnitude, from about 5 MHz to 3 kHz [22]. The small quadrupolar

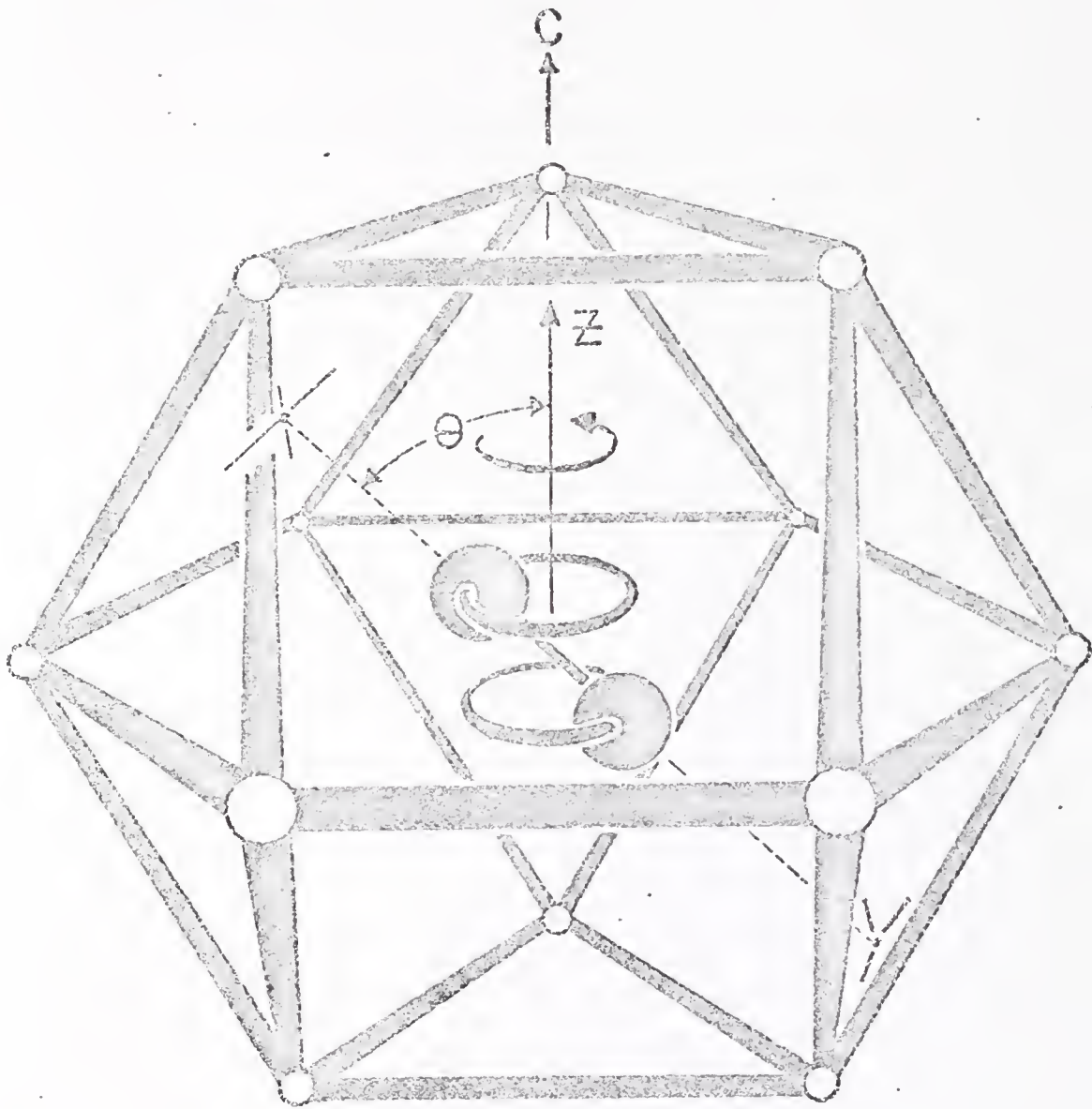


Figure 42. Crystal structure of β nitrogen. Open circles defining the cage structure denote hcp positions of molecules. Only the central molecule is illustrated. All molecules precess about the c axis at an angle $\theta = 54^\circ 44'$. At this orientation the molecular axis during the course of precession passes approximately through the center of each of the square faces of the surrounding cage.

interaction in β nitrogen is consistent with a deviation of only a few minutes of arc from the $54^{\circ}44'$ value, and has been shown [34] to be correlated with the variation of the c/a ratio during thermal expansion.

7.4 Data Analysis

We now can provide an insight into the behavior of τ_Q at the triple point. The molecules in the β solid are relatively free to reorient through large angles, but are restricted in translational freedom. Fixing the molecules on lattice sites ensures each one has its own space in which to reorient with little obstruction from the other molecules. Upon melting, the collisions due to the unleashed translational degrees of freedom destroy this cooperative behavior and the molecule is more hindered in its rotation even though the average density is less in the liquid phase, and τ_Q increases accordingly.

Several recent molecular dynamics computer simulations are consistent with this picture [37,38,39]. In particular time traces of the orientation of a molecule in the liquid near the triple point reveal [39] that molecules tend to undergo several small-angle reorientations before reorientating through an angle on the order of one radian.

That there should be at most a small discontinuity in τ_{sr} across the triple point is not surprising, considering the relative freedom enjoyed by molecules in β nitrogen which is a plastic crystal. Molecules can readily undergo changes in angular momentum whether or not restricted in translational freedom. The more unexpected result is that at lower temperatures in the solid the product of reduced correlation times approaches a temperature independent constant even more closely than in the liquid. The value of the constant though is apparently less than $1/6$.

The Hubbard relation was based on an isotropic rotational diffusion model which at first thought would not seem to be valid in the case of the large angle reorientational jumps. The theoretical problem has not yet been solved. However, Ivanov [40] has discussed the theory of rotational Brownian movement as a random-walk process including the question of how large the reorientational jumps may become before their discrete nature is distinguishable from a truly isotropic rotational diffusion. He introduces a parameter q which is related to the ratio of the Raman and infrared line widths which varies from 3 in the case of isotropic rotational diffusion to unity when the discrete nature of the jumps is dominant.

For the angles $48^{\circ}11'$ and $70^{\circ}32'$, the value of Ivanov's parameter q is 2.6 and 2.2, respectively, and hence rather close to the rotational diffusion limit, especially for the surely more predominant smaller jumps. The general conclusions of Ivanov's analysis seem to apply here and it is therefore reasonable to expect a temperature-independent slope for τ_Q^* vs. τ_{sr}^* in β nitrogen, although the constant may not be $1/6$.

7.5 Conclusions

We have observed that the Hubbard relation $\tau_Q^* \tau_{sr}^* = 1/6$ is approached even more closely in liquid nitrogen as the temperature is reduced from 77 K to the triple point. This confirms the effect noted by Krynicki et al. [24] at higher temperatures.

We next noted that the decrease in τ_Q upon solidification at the triple point and consequently the fact that the product of the reduced correlation times is less than $1/6$ were explained by the greater reorientational freedom in β solid than in liquid.

Finally, that the Hubbard relation should be obeyed at all was explained by noting the rotational diffusion model is quite good even at the relatively large angle reorientations encountered in β nitrogen.

APPENDIX A
 FOCAL PROGRAM TO CALCULATE THE POWDER PATTERN SPECTRUM
 OF ^{15}N IN α N_2 ENRICHED TO 33% ^{15}N

C-8K FOCAL 01969

```
01.05 A "RUN NUMBER"R1;A "WIDTH(HZ)"V1;S V=V1/9.27
01.10 S PI=3.14159;ASK "H" H;S L=H/7560
01.20 F X=PI/18,PI/18,PI/2;D 2.0
01.30 T " " ", "FINISHED", !;QUIT
```

```
02.05 T 74.01, "ANGLE"X+180/PI, !
02.10 S Y=FSIN(X);S Z=FCOS(X)
02.15 S A0=-1/4+L*2*(3+Z*2-1)/2;S A1=L*2+3/4
02.20 S C=(-A0/2)/FSQT(A1*3/27);S B=2*FSQT(A1/3)
02.25 S E=FATAN(FSQT(1-C*2)/C)/3
02.27 I (A0)2.3;S E=E-2*PI/3
02.30 F I=1,1,3;D 4.0
02.40 S D=1.352067*(1-3*Z*2)*61.29+256;D 4.6
02.45 S D=-D+512;GOTO 4.6
```

```
04.05 S T=-FSGV(A0)*B*FCOS(E)
04.10 S H1=(1/2+L*Z+T)/(L*Y/1.414214)
04.20 S H2=(1/2+L*Z+T)/(1/2-L*Z+T)
04.30 S K1=FSQT(1/(1+H1*2+H2*2))
04.40 S K2=-H1*K1;S K3=H2*K1
04.50 S D=-61.29+(2*(K1*2-K3*2)*Z-K2*(K1+K3)*Y/1.414214)-25
04.55 T 72.00, " " ", "I", I
04.57 T 77.06, " " ", "T" T, " " ", "W"(D+256)/122.58, !
04.60 F N=512+D-4*V, 512+D+4*V;D 5.0
04.70 S E=E+2*PI/3
```

```
05.10 S R=FEXP(-(N-512-D)/V)*2/2)*Y*2000;D 7.0
```

```
07.10 S R=R+FNEW(N)
07.20 S S=FNEW(N,R)
```

*

LIST OF REFERENCES

1. L.O. Andersson, M. Gourdji, L. Guibe, and W.G. Proctor, C.R. Acad. Sci. B 267, 803 (1968).
2. R. Blinc, M. Mali, R. Osredkar, A. Prelesnik, I. Zupancic, and L. Ehrenberg, Chem. Phys. Lett. 9, 85 (1971).
3. D.T. Edmonds and P.A. Speight, Phys. Lett. 34A, 325 (1971).
4. A. Abragam, The Principles of Nuclear Magnetism (Oxford: The Clarendon Press, 1961).
5. E.R. Andrew, Nuclear Magnetic Resonance (Cambridge: University Press, 1956).
6. M.H. Cohen and F. Reif, Solid State Physics, Vol. 5. (New York: Academic Press, 1957).
7. G.E. Pake, J. Chem. Phys. 16, 327 (1948).
8. N.F. Ramsey, Nuclear Moments (New York: John Wiley and Sons, 1953).
9. G.M. Volkoff, H.E. Petch, and D.W.L. Smellie, Can. J. Phys. 30, 270 (1952).
10. G. Hutton and B. Pedersen, J. Mag. Res. 13, 119 (1974).
11. Z.M. El Saffar, J. Mag. Res. 19, 233 (1975).
12. P.M. Parker, J. Chem. Phys. 24, 1096 (1956).
13. R.G. Gordon, Advances in Magnetic Resonance, Vol. 3 (New York: Academic Press, 1968).
14. P.S. Hubbard, Phys. Rev. 131, 1155 (1963).
15. E. Kluk and J.G. Powles, Mol. Phys. 30, 1109 (1975).
16. G. Albrecht and R.B. Corey, J. Am. Chem. Soc. 61, 1087 (1939).
17. Y. Iitaka, Acta Crystallogr. 13, 35 (1960).
18. Y. Iitaka, Acta Crystallogr. 11, 225 (1958).
19. R.E. Marsh, Acta Crystallogr. 11, 654 (1958).

20. T.H. Jordan, H.W. Smith, W.E. Streib, and W.N. Lipscomb, J. Chem. Phys. 41, 756 (1964).
21. J.R. Brookeman, M.M. McEnnan, and T.A. Scott, Phys. Rev. B 4, 3661 (1971).
22. A.S. DeReggi, P.C. Canepa, and T.A. Scott, J. Mag. Res. 1, 144 (1969).
23. M.G. Scientific Gasses, Kearny, New Jersey.
24. K. Krynicky, E.J. Rakkamaa, and J.G. Powles, Mol. Phys. 29, 539 (1975).
25. J.E. Piott and W.D. McCormick, Low Temperature Physics - LT 13, Vol. 2 (New York: Plenum Press, 1974).
26. D.J. Kroon, Philips Res. Rep. 15, 501 (1960).
27. W.N. Hardy and A.J. Berlinsky, Phys. Rev. B 8, 4996 (1973).
28. A.J. Berlinsky and W.N. Hardy, Phys. Rev. B 8, 5013 (1973).
29. I.B. Goldberg and H.R. Crowe, J. Mag. Res. 18, 497 (1975).
30. J.C. Raich, J. Chem. Phys. 56, 2395 (1972).
31. D.H. Smith and R.M. Cotts, J. Chem. Phys. 41, 2403 (1964).
32. R.L. Armstrong and P.A. Speight, J. Mag. Res. 2, 141 (1970).
33. M.R. Baker, C.H. Anderson, and N.F. Ramsey, Phys. Rev. 133, A1533 (1964).
34. T.A. Scott, Physics Reports (in press).
35. W.E. Streib, T.H. Jordan, and W.N. Lipscomb, J. Chem. Phys. 37, 2962 (1962).
36. I.N. Krupskii, A.E. Prokhvatilov, and A.I. Erenburg, Fizika Nizkikh Temperatur 1, 359 (1975).
37. J. Barojas, D. Levesque, and B. Quentrec, Phys. Rev. A 7, 1092 (1973).
38. P.S.Y. Cheung and J.G. Powles, Mol. Phys. 30, 921 (1975).
39. B. Quentrec and C. Erot, Phys. Rev. A 12, 272 (1975).
40. E.N. Ivanov, Sov. Phys.-JETP 18, 1041 (1964).

BIOGRAPHICAL SKETCH

Lyle Milton Ishol was born on July 16, 1932 in Reeder, North Dakota. He moved to South Dakota in 1937 and graduated from Philip High School, Philip, South Dakota, in 1950.

After attending Augustana College, Sioux Falls, South Dakota for two years, he entered the United States Naval Academy, Annapolis, Maryland in 1952. He received a Bachelor of Science degree and a commission in the United States Navy in 1956. He served on active duty until 1967 when he resigned to enter the University of Florida for graduate study in physics. He received the Doctor of Philosophy degree in June, 1976.

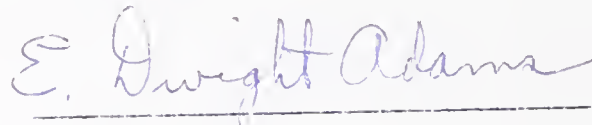
He married the former Jane Tisdale of Gainesville, Florida, in 1958 and has two daughters, Susan (12) and Karen (9).

I certify that I have read this study and that in my opinion it conforms to acceptable standards of scholarly presentation and is fully adequate, in scope and quality, as a dissertation for the degree of Doctor of Philosophy.



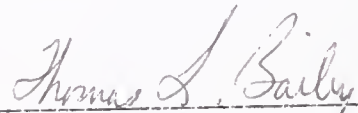
Thomas A. Scott, Chairman
Professor of Physics

I certify that I have read this study and that in my opinion it conforms to acceptable standards of scholarly presentation and is fully adequate, in scope and quality, as a dissertation for the degree of Doctor of Philosophy.



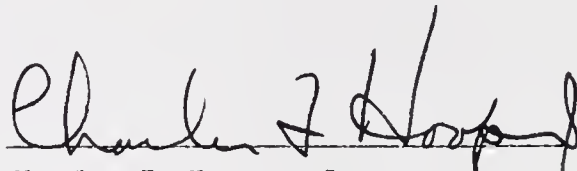
E. Dwight Adams
Professor of Physics

I certify that I have read this study and that in my opinion it conforms to acceptable standards of scholarly presentation and is fully adequate, in scope and quality, as a dissertation for the degree of Doctor of Philosophy.

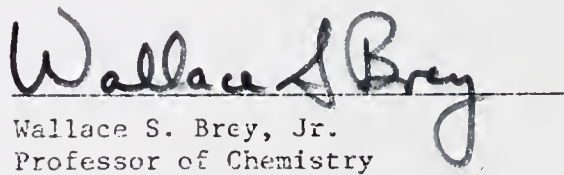


Thomas L. Bailey
Professor of Physics and Electrical
Engineering

I certify that I have read this study and that in my opinion it conforms to acceptable standards of scholarly presentation and is fully adequate, in scope and quality, as a dissertation for the degree of Doctor of Philosophy.


Charles F. Hooper, Jr.
Associate Professor of Physics

I certify that I have read this study and that in my opinion it conforms to acceptable standards of scholarly presentation and is fully adequate, in scope and quality, as a dissertation for the degree of Doctor of Philosophy.


Wallace S. Brey, Jr.
Professor of Chemistry

This dissertation was submitted to the Graduate Faculty of the Department of Physics and Astronomy in the College of Arts and Sciences, and to the Graduate Council, and was accepted as partial fulfillment of the requirements for the degree of Doctor of Philosophy.

June, 1976

Dean, Graduate School